DEVELOPMENT OF HIGH-RESOLUTION AND REAL-TIME MICROWAVE IMAGING ALGORITHMS FOR APPLICATIONS IN BREAST TISSUE IMAGING AND MICROWAVE ABLATION MONITORING

by

Luz Maria Neira Steinfort

A dissertation submitted in partial fulfillment of
the requirements for the degree of

Doctor of Philosophy

(Electrical and Computer Engineering)

at the

UNIVERSITY OF WISCONSIN–MADISON

2018

Date of final oral examination: 12/14/18

The dissertation is approved by the following members of the Final Oral Committee:
  Susan C. Hagness, Professor, Electrical and Computer Engineering
  Barry D. Van Veen, Professor, Electrical and Computer Engineering
  David T. Anderson, Professor, Electrical and Computer Engineering
  Walter F. Block, Professor, Biomedical Engineering

ACKNOWLEDGMENTS

I want to thank my advisors, Professors Susan Hagness and Barry Van Veen for their instruction, guidance, and support through my graduate studies, both in my research and personally.

I am also indebted to numerous fellow students. In particular, Dr. Timothy J. Colgan and Dr. Owen R. Mays for their warm welcoming to Madison, and their guidance and full support during my first years in the program. Also to my lab friends and fellow graduate students, Dr. James F. Sawicki, Zach Hertzberg, Prathyusha Sharma, Dr. Sathya Ganta, Dr. Hung Luyen, Dr. Yahya Mohtashami, Alex Haufler, Audrey Evans, and Yizhou Yao for making my time here productive and enjoyable.

Finally, I would like to thank my family. My parents, for their invaluable assistance and support. My son Cristian, who gives me purpose, strength, joy, and chuckles. And my husband Edgar Hernandez, for his steady encouragement and always timely wise advice.

CONTENTS

LIST OF TABLES

LIST OF FIGURES

ABSTRACT

Microwave imaging is an imaging modality that produces a 3D map of the dielectric properties of an object. It shows promise for medical imaging because it is portable, safe, and low cost, and most importantly there is a strong correlation between tissue physiology and dielectric properties. In breast tissue, there is a high dielectric contrast between fibroglandular tissue and adipose tissue and a moderate contrast between malignant and healthy fibroglandular tissue. Therefore, microwave imaging has excellent potential for breast cancer screening. Another promising application of microwave imaging is the monitoring of thermal therapies for cancer treatment. During thermal therapies, such as microwave ablation (MWA), the dielectric properties of the treated tissue change because of temperature changes and damage induced in the tissue. The contrast between thermally damaged tissue and healthy tissue can be exploited to monitor the evolution and completeness of the treatment.

Some of the challenges of conventional microwave imaging are that it lacks high-resolution and it is computationally expensive. Microwave imaging involves solving a highly ill-posed microwave inverse scattering problem, which results in images with moderate resolution exhibiting blurred boundaries and poor dielectric properties estimation, especially when imaging highly heterogeneous breast tissue. Additionally, the several computational electromagnetic simulations that are necessary to construct the microwave scattering problem are computationally time consuming. The computational cost of microwave imaging limits its applicability for monitoring MWA in real-time.

In this dissertation, I developed microwave imaging algorithms for breast cancer screening and MWA real-time monitoring. First, I explored the use of prior spatial information to enhance the resolution of microwave breast imaging and developed an algorithm that succeeds at producing high-resolution images by combining medical imaging modalities. Second, I investigated the foundations for using microwave imaging to monitor MWA. I characterized the changes in temperature and dielectric properties of breast tissue and liver tissue during MWA and created models of the evolution of tissue properties during treatment. Finally, I developed microwave imaging algorithms that can operate in real-time by exploiting these models to achieve accurate and timely monitoring of MWA.

1 INTRODUCTION

The overall objectives of my Ph.D. research have been to further advance the algorithms and techniques of microwave imaging, particularly in applications of breast cancer screening and microwave ablation (MWA) treatment monitoring. Breast cancer is the second most commonly diagnosed type of cancer worldwide, and it is by far the most common type of cancer among women [1]. In 2012 death rates for female breast cancer in the United States were down 36% from historical peak rates in 1990 as a result of improvements in early detection and treatments [2, 3]. However, it remains the leading cause of death from cancer in young women (20 to 59 years old), and holds second place, after lung cancer, in older women [2]. These facts suggest the importance of early detection and effective treatment of breast cancer. Part of my research has focused on developing microwave imaging algorithms for breast cancer screening and the other part has focused on aiding the basic understanding of the effects of MWA on tissue dielectric properties, temperature, and cell damage, and developing microwave imaging algorithms for MWA treatment monitoring.

Breast Cancer Screening

The breast imaging modalities in clinical use for breast cancer screening have limitations [4]. Conventional X-ray mammography is a 2D projection of the soft tissues in the breast, and therefore the probability of detection of breast cancer (sensitivity) is relatively low, particularly for women with dense glandular tissue. In a wide literature review, Berg [5] reported that only 36% of all cancers were identified in high-risk women screened with mammography. Additionally, mammography involves ionizing radiation that increases the risk of future cancers. Magnetic resonance imaging (MRI) has the advantage of producing high-resolution 3D images of the breast, and when used to complement mammography the sensitivity improves considerably. According to Berg [5], 93% of all cancers in the study population were identified by combining mammography and MRI. However, the high cost of MRI precludes its use as a screening method for all women. Complementing mammography with ultrasound can be more cost-effective, but the sensitivity is improved only to around 50% for high-risk women [6].

Given the need for alternative breast cancer screening techniques, there has been an interest in exploring several emerging new imaging modalities, such as electrical impedance imaging, thermography, optical imaging, and microwave imaging, which are still in an experimental stage. Microwave imaging via inverse scattering (reviewed in Chapter 2.1) is a promising technique because it provides 3D images of the dielectric properties, and is portable, safe, and low cost. Microwave imaging involves having an array of antennas surrounding the breast and transmitting low power, non-ionizing radiation, in the microwave frequency range, through the breast. The received signals are then processed with a microwave inverse scattering algorithm to produce the image [7, 8, 9]. Large-scale studies of the dielectric properties of breast tissues [10, 11] have shown that there is a correlation between these properties and tissue physiology. There is a high dielectric contrast of 10:1 between healthy fibroglandular tissue and adipose tissue and a moderate contrast of about 10% between malignant and healthy fibroglandular tissue. Contrast agents to improve tumor contrast are being investigated [12, 13].

A primary challenge of microwave imaging based on conventional inverse scattering is that it lacks high resolution. The inverse scattering problem is highly ill-posed, and therefore regularization techniques are needed to obtain bounded solutions and avoid overfitting to noise. Regularization techniques usually result in smooth edges between the different tissue types and inaccurate property estimation for each tissue type. Different types of regularization have been explored to try to overcome this issue, such as [14, 15, 16, 17, 18]. The use of prior spatial information, such as what can be obtained with a high-resolution complementary modality, shows promise for enhancing the resolution of microwave imaging.

Chapter 3 presents my work on microwave imaging for breast cancer screening. I developed a microwave imaging algorithm that incorporates *a priori* information of the spatial extent of different tissue types in the breast to achieve high spatial resolution and accurate dielectric properties estimation. Accurate dielectric properties estimation offers insights about the tissue's health state. I evaluated the performance of the method by imaging detailed, anatomically realistic numerical 3D breast phantoms, under different levels of noise, for different choices of the regularization parameters, and various types and amounts of error in the prior information.

Cancer treatment

Breast cancer is usually treated with a combination of treatments: chemotherapy, endocrine therapy, radiotherapy, and surgery. However, all of these treatments have risks of short and long-term side effects, such as pain, infections, lymphedema, dermal reactions, cardiac complications, peripheral neuropathy, secondary cancers, and psychological distress. Microwave ablation (MWA) (reviewed in Chapter 2.2) is a promising technique for low risk and minimally invasive treatment of breast cancer, mainly as an alternative to surgery, and for tumors that do not respond to pre-operatory therapies [19, 20].

Microwave ablation consists of delivering microwave energy into the malignant tumor via an interstitial antenna. The microwave energy absorbed in the tumor produces heat and induces cytotoxic effects that result in protein denaturation and coagulation necrosis. MWA offers significant advantages over other types of thermal ablation technologies, including radiofrequency ablation (RFA), high-intensity focused ultrasound (HIFU), and laser ablation [21]. Currently, MWA is being used clinically for treating unresectable malignant hepatic tumors [22], but it has also showed promise for treating a variety of other cancers such as lung, bone, renal, and breast cancer [23, 19, 24, 25, 26].

The lack of suitable imaging technologies for monitoring and verifying the completeness of MWA in real time is a limiting factor for its clinical application. Ultrasound is useful for ensuring the antenna is well positioned in the tumor prior to the start of ablation, but it is not suitable for imaging during the ablation treatment due to imaging artifacts that arise during heating. These artifacts prevent accurate assessment of the extent of tissue damage [27]. Using MRI for MWA monitoring is attractive, but the effects of heating MR contrast agents are unknown [28], and the cost remains prohibitive. Radiation exposure and lack of standard operating procedures and dose reference levels are a persisting concern for computed tomography-guided interventions [29].

Microwave imaging algorithms show promise for monitoring the extent of tissue damage during MWA. As tissue becomes ablated, there is a change in its dielectric properties [30, 31]. A microwave imaging algorithm can take advantage of the contrast between ablated and non-ablated tissue to image the ablated region. Also, it can exploit the presence and knowledge of the location of the interstitial antenna for modeling and sensing purposes. Finally, by using microwave imaging, the ablation and monitoring can be done with an integrated microwave system that would be low cost, safe, and minimally invasive. Microwave imaging for MWA monitoring is reviewed in Chapter 2.3.

Chapter 4 presents my work on advances in MWA as a tool for breast cancer treatment. I conducted MWA experiments on *ex vivo* human breast tissue to study the effects of MWA on breast tissue dielectric properties, temperature, and cell damage. This knowledge is essential for MWA antenna and equipment design and for evaluating the success of MWA as a technology for breast cancer treatment. Additionally, characterization of the changes in dielectric properties induced by ablation provides the foundation for using microwave imaging as a MWA monitoring technique.

Chapter 5 of this dissertation presents additional groundwork for supporting microwave imaging as a tool for MWA monitoring. I conducted MWA experiments in *ex vivo* porcine liver tissue to characterize the spatiotemporal evolution of temperature and dielectric properties during MWA. Unlike breast tissue, liver tissue is homogeneous; therefore it provides a more controlled testbed for studying the changes in temperature and dielectric properties induced by MWA. This study is the first wide-band wide-temperature study of dielectric properties of liver tissue during heating by MWA.

Chapter 6 and 7 present the microwave-imaging algorithms I developed for monitoring MWA in real time. The algorithms exploit the knowledge of the dynamic properties of tissues during ablation, studied in Chapters 4 and 5, to reduce computational burden and achieve real-time monitoring capabilities. Chapter 6 presents a microwave imaging via inverse scattering algorithm that estimates the size of the ablation zone in homogeneous and heterogeneous tissues by comparing the measured scattered signals during ablation to pre-computed simulated array measurements of patient-specific models containing candidate ablation zones. The method is highly accurate but susceptible to modeling errors. Chapter 7 presents a microwave imaging algorithm that exploits the time-difference-of-arrival of pulse signals sent before and during ablation to estimate the temperature profile of the tissue during the procedure. In this strategy, the knowledge obtained in Chapter 5 serves as a basis for creating a spatial model of the temperature during ablation that is combined with radar time-difference-of-arrival calculations to image the ablation accurately and robustly in real time.

2 BACKGROUND AND SIGNIFICANCE

2.1 Microwave Breast Imaging

Microwave breast imaging via inverse scattering is a low cost, portable, and safe experimental imaging modality that entails an array of antennas that operate in the ultra-high frequency range (UHF) (300 MHz - 3 GHz) surrounding the breast. Scattered fields are measured for every channel throughout the array, and the dielectric properties of the breast are estimated by solving an inverse scattering problem.

There is a correlation between dielectric properties and breast tissue physiology. Therefore, the distribution and location of the different tissues that constitute the breast can be inferred from the estimated dielectric properties.

Dielectric Properties of Breast Tissues

The breast is constituted primarily by adipose, glandular and fibrous tissues. The dielectric properties of the tissues are related to the tissue's water content [32]. The dielectric contrast between fibroglandular (high water content) and adipose tissue (low water content) is large, on the order of 10:1 [10]. Malignant cancerous tissue usually originates from the fibroglandular tissue and has higher water content due to increased blood flow and immature vascularization [32]. Therefore there is also a contrast between healthy fibroglandular tissue and malignant tissue, of around 10% [11]. Figure 2.1 shows the dispersive dielectric properties of breast tissues according to the large-scale Wisconsin-Calgary studies [10, 11] where the dielectric properties of the different tissue types were measured shortly after excision.

Dielectric properties of ex vivo breast tissue have been also reported in [33], and the reported results are similar to the ones in [10, 11]. Some studies have reported higher contrast between healthy and malignant tissue, e.g. [34], but they have been small-scale studies.

Distorted Born Iterative Method

Several approaches have been developed for solving the microwave inverse scattering problem [35, 9, 36, 37, 8, 7, 38]. Because the inverse scattering problem is non-linear and ill-posed, these approaches involve iterative techniques in which at each iteration the es-

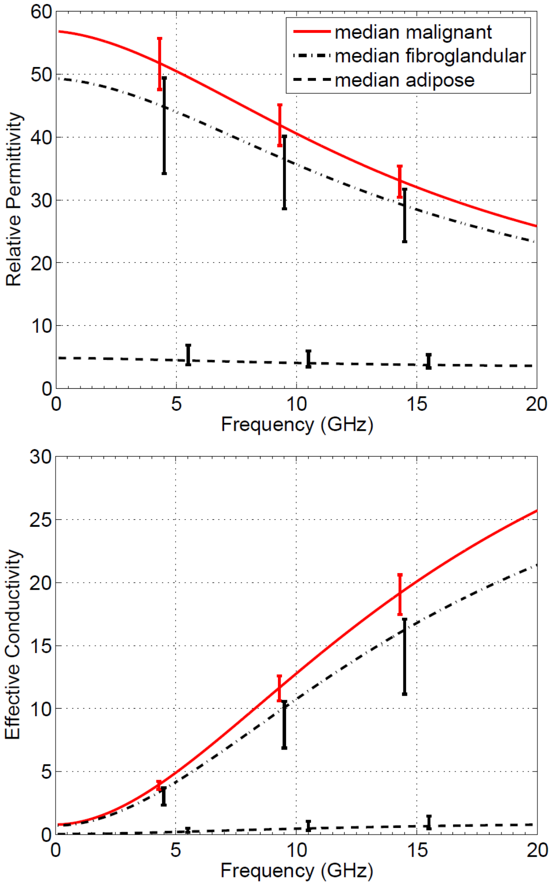

(a)

(b)

Figure 2.1: (a) Relative permittivity and (b) effective conductivity of healthy and malignant breast tissues in the 50 MHz-20 GHz frequency range, obtained from [10, 11]. The lines correspond to the 50th percentile and the variability bars show the 25th and 75th percentiles.

timate of the map of dielectric properties of the scatterer is updated to minimize the difference between simulated scattered fields and measured scattered fields. Some examples of algorithms are the Born Iterative Method (BIM) [38, 39], Distorted Born Iterative Method (DBIM) [7, 39], Gauss-Newton methods [8, 36, 35, 40], and Contrast Source Inversion (CSI) method [37, 9, 41]. All these methods exhibit similar performance [42, 43], with the exception of BIM that falls behind for high contrast imaging scenarios. This section describes the Distorted Born Iterative Method.

The electric field integral equation [39] governs the scattering of electromagnetic radiation by a non-magnetic object inside a volume V with dielectric properties ϵ, as in:

$$\mathbf{E}^s(\mathbf{r}_{obs}) = \omega^2\mu_0 \int_V \mathbf{G}^b(\mathbf{r}_{\text{obs}}|\mathbf{r}')\mathbf{E}^t(\mathbf{r}')[\epsilon(\mathbf{r}') - \epsilon^b(\mathbf{r}')]d\mathbf{r}' \tag{2.1}$$

Here $\mathbf{E}^s$ is the scattered electric field, defined as the difference between the measured field when the scattering object is present and the incident field when only the background dielectric profile, ϵ^b, is present; $\mathbf{G}^b$ is the dyadic Green's function for the background; and $\mathbf{E}^t$ is the electric field inside the volume. The observation point is denoted as $\mathbf{r}_{obs}$. The permeability of free space is denoted as μ_0 in 2.1.

To find the properties of an unknown scatterer, e.g., the dielectric properties of the breast, we take measurements for a set of source-observation channels at one or several discrete frequencies, ω, to form a set of equations for the unknown properties ϵ. Each of the measurements corresponds to one equation in the form of 2.1. These equations are non-linear since the total field inside the volume, $\mathbf{E}^t$, depends on the dielectric properties inside it, ϵ. The DBIM linearizes each equation by approximating $\mathbf{E}^t$ in the integrand of 2.1 by the incident electric field inside volume V computed for the background dielectric profile. Full-wave computational electromagnetic simulations are used to calculate the incident electric field and the background Green's function, which can be computed numerically as in [7]. This step is denoted as the forward solution.

The set of linearized equations for all source-observation-frequency channels forms a system of scattering equations,

$$\mathbf{Ax} = \mathbf{b} \tag{2.2}$$

, which is then solved to find an approximation to the contrast between the actual properties of the volume and the background properties, $\mathbf{x} = \epsilon - \epsilon^b$. This step is denoted as the inverse solution. The estimate of the dielectric properties of the scatterer is then used to update the properties of the background. The forward solution, inverse solution, and updating of the background properties are repeated iteratively until the residual scattered fields are negligible. Once convergence has been reached, the dielectric properties of the updated background correspond to the estimate of the dielectric properties inside the volume.

Since Eq. 2.2 is ill-posed, regularization techniques are required to obtain a bounded solution. Different regularization methods favor solutions with different features. However, usually the techniques for solving Eq. 2.2 result in overly smoothed images [7]. Figure 2.2 shows an example of microwave breast imaging using DBIM. The blurred boundaries between tissue types are representative of the moderate resolution observed with conventional microwave imaging techniques.

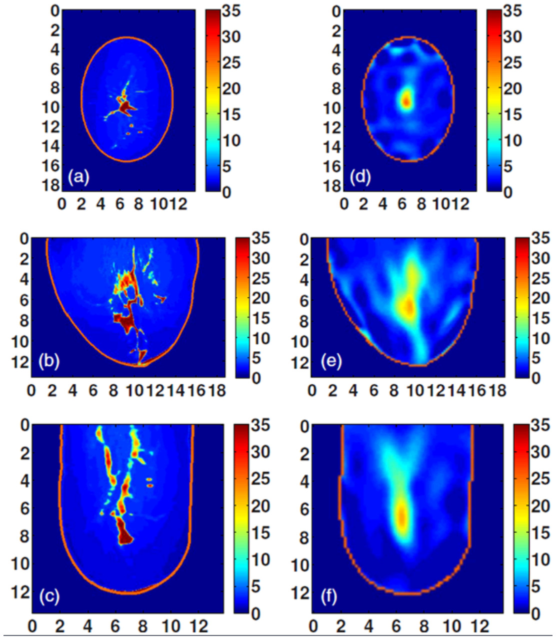

Figure 2.2: Exact [(a)-(c)] and reconstructed [(d)-(f)] profiles of $\Delta\epsilon$ for the Class 1 breast phantom shown in coronal (top row), sagittal (middle row), and axial (third row) cross-sections. Source: Shea et al. [7].

High-resolution microwave imaging

Different strategies have been explored to improve the resolution of microwave imaging. The studies [18, 14] proposed level-set methods to preserve dielectric boundaries. These methods have demonstrated improvement for breast density estimation using microwave imaging. Gao et al. [44] proposed using sparse regularization for the specific case of finding tumors with the aid of contrast enhancement agents. Tumors as small as 1 cm in diameter were accurately localized in 3D realistic numerical breast phantoms using sparse regularization.

One particularly promising strategy to improve image resolution of microwave imaging is to incorporate *a priori* structural information, also known as spatial priors, into the inverse scattering algorithm. Structural information given by a high-resolution imaging modality can be combined into the moderate resolution microwave imaging algorithm to produce high-resolution images of the distribution of dielectric properties in the breast.

The idea of complementing relatively low-resolution imaging with high-resolution imaging has been studied for years in the context of several medical imaging modalities. Examples include improving the resolution of Positron emission tomography (PET), Single-photon emission computed tomography (SPECT), and Electrical impedance tomography (EIT) by using boundary information obtained from magnetic resonance imaging (MRI) or computational tomography (CT) (see, for example, [45, 46, 47, 48, 49]). In the case of microwave imaging, high-resolution information about the spatial distribution of the different tissue types in the breast can be obtained from a high-resolution imaging modality, such as MRI or ultrasound imaging.

Information about tissue boundaries has been incorporated into microwave breast imaging algorithms in [50, 51, 52]. The method used in these studies improves the accuracy of the dielectric properties estimations greatly. However, it is computationally inefficient, which prohibits its implementation for imaging large volumes such as the breast, and the heterogeneity of the tissues cannot be captured effectively. There is an opportunity for improving microwave imaging by using spatial priors in a computationally efficient manner.

2.2 Microwave Ablation (MWA)

MWA ablation as a cancer treatment is a thermal therapy that consists of delivering microwave energy into the tumor, through a minimally invasive antenna, that heats the tissue to the point of cell death. Other thermal therapies for cancer treatment are radio-frequency ablation (RFA), high-intensity focused ultrasound (HIFU), and laser ablation. MWA has the advantages of achieving higher temperatures, larger ablation volumes, and shorter ablation times than other thermal therapies [20]. Additionally, MWA does not lose effectiveness as the tissue becomes ablated, since microwave propagation is not impeded by desiccated tissue, and it can defeat the heat-sink effect of nearby blood vessels that usually reduces the performance of thermal therapies because of its rapid heating rate [53].

MWA is being used clinically for the treatment of lung, kidney, bone, and liver cancer [22, 23, 24, 25, 26]. The dielectric properties of these tissues are relatively homogeneous. The clinical usefulness and safety of MWA as a treatment for tumors in heterogeneous breast tissue is still being investigated. Initial studies have shown promising results [19, 20].

2.3 Microwave Ablation Monitoring

The lack of suitable imaging technologies for monitoring and verifying the completeness of ablation is a major limiting factor in the clinical application of MWA [54, 55, 20].

The majority of MWA studies have relied on computed tomography or ultrasound for antenna placement. Thermocouple needles, ultrasound, or magnetic resonance imaging have been used for monitoring the MWA procedure. However, they have some drawbacks. Thermocouple needles increase the invasiveness of the treatment and only provide localized information. Ultrasound is susceptible to artifacts during thermal ablation, such as increased echogenicity and acoustic shadowing, that obscure the target lesion and impede real-time ablation assessment [27, 55, 20]. Finally, magnetic resonance imaging monitoring is expensive, and the effects of heating the required contrast agents are unknown and potentially hazardous [28]. There is a need for innovative real-time image-guidance of MWA.

Dielectric properties changes

During MWA, microwave energy heats the tissue to high temperatures, above 60°C, causing irreversible cell damage through protein denaturation and coagulation necrosis [56]. Figure 2.3 shows a sample of ablated liver tissue, where the changes in tissue appearance are evident in the vicinity of the MWA antenna. The dielectric properties of the tissue in the microwave frequency range also change as the tissue becomes ablated. Several studies have reported the temperature dependence of tissue dielectric properties [57, 58]. During MWA, the high temperatures additionally produce physiological changes in the tissue, making the change in dielectric properties even more drastic and irreversible. For example, Lopresto et al. [30] reported an irreversible decrease of approximately 38% in relative permittivity and 33% in effective conductivity at 2.45 GHz during MWA of ex vivo bovine liver tissue.

Microwave imaging for MWA monitoring

The substantial dielectric properties changes that occur during MWA ablation inspire using microwave imaging for monitoring the growth of the ablated zone. Microwave imaging has been used for monitoring hyperthermia treatment [60, 61, 62], where the temperature increase is relatively small (less than 20°C), and so is the change in dielectric properties (less than 10%). Haynes et al. [60] developed a microwave imaging algorithm to monitor the

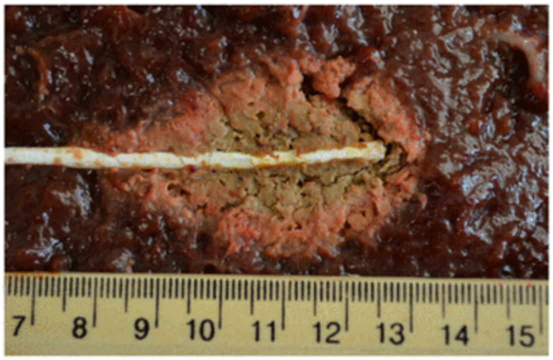

Figure 2.3: Photograph of a representative ablation zone created in ex vivo bovine liver, using a 1.9 GHz balun-free helical monopole at 42 W for 5 min. Source: Luyen et al. [59].

temperature of water between 22 and 55°C in real time. The algorithm produced estimates as fast as one frame/s by using a linear approximation of the electric field integral equation.

However, linear approximations of the inverse scattering problem are not accurate for the large dielectric contrasts produced by MWA. Iterative techniques, such as the Born and Distorted Born iterative methods [39], in which the estimates of the interior fields are updated in each iteration, are needed. The computationally expensive calculation of the interior fields precludes real-time assessment of the extent of the ablation zone. However, MWA offers some unique aspects that can be exploited to achieve both accuracy and fast computation time: *a priori* knowledge about the tissue environment pre-ablation is available, the MWA antenna location is known, and the dielectric properties changes are spatially localized near the MWA antenna. Additionally, information about the spatio-temporal changes that occur during ablation can be incorporated into the microwave imaging algorithm, to improve accuracy and computational efficiency further.

3 HIGH-RESOLUTION MICROWAVE BREAST IMAGING USING A 3-D INVERSE SCATTERING ALGORITHM WITH A VARIABLE-STRENGTH SPATIAL PRIOR CONSTRAINT

This chapter was previously published in *IEEE Transactions on Antennas and Propagation* [63].

3.1 Abstract

Microwave inverse scattering is an exploratory imaging modality with potential for several clinical breast imaging applications including density evaluation, cancer detection, and treatment monitoring. However, conventional regularization techniques used to solve the ill-posed inverse problem typically result in blurred boundaries between tissue structures exhibiting dielectric contrast, thereby limiting the effective resolution. We present a method to improve microwave breast imaging resolution that incorporates *a priori* information about the boundaries between different tissues in the breast into the inverse scattering algorithm. This spatial prior information can be derived from another imaging modality, such as MRI. Our method exploits the fact that the dielectric properties within a tissue type exhibit low to moderate variability by favoring solutions to the inverse scattering problem that have small variations in dielectric properties within each tissue region. The amount of variation tolerated in each regions is controlled by a spatial prior constraint parameter. We demonstrate the feasibility of the method by imaging detailed, anatomically inspired numerical 3D breast phantoms. The performance in the presence of different levels of noise and for different choices of the constraint parameter is evaluated. We also demonstrate the robustness of the algorithm with respect to errors in the spatial prior information.

3.2 Introduction

Microwave breast imaging via inverse scattering consists of reconstructing the dielectric properties of the breast from measurements of scattered electromagnetic fields. Microwave imaging offers several potential advantages compared to other breast imaging modalities such as X-ray mammography and MRI: it uses non-ionizing radiation, is low cost, and provides 3D images with quantitative, complementary information about tissue properties. Breast tissue dielectric properties are correlated with tissue physiology [10, 11]. The diagnostic utility of this information extends to several clinical applications, including evaluation of breast density, detection of breast cancer, and monitoring of treatment.

However, microwave imaging spatial resolution is typically limited by the regularization techniques used to solve the inverse problem's ill-posed system of equations. Conventional regularization techniques such as L_2 regularization usually result in smooth or blurred images. Several alternative regularization strategies have been investigated to improve image resolution and preserve boundaries between regions with distinctly different dielectric properties. Examples include total variation regularization, Krylov subspace regularization, and level set methods [14, 15, 9, 16, 17, 18].

One particularly promising strategy to improve image resolution is to incorporate *a priori* structural information, also known as spatial priors, into the inverse scattering algorithm. The idea of incorporating anatomical information obtained from a high-resolution imaging modality into a complementary lower-resolution imaging algorithm has been studied in the context of several imaging modalities. Examples include improving the spatial resolution of PET, SPECT, and EIT by using boundary information obtained from MRI or CT (see, for example, [45, 46, 47, 48, 49]).

In the case of microwave imaging, structural information about the breast can be obtained from a higher resolution imaging modality, such as MRI or ultrasound imaging. Microwave imaging algorithms that use this structural information can provide a high-resolution quantitative image of dielectric properties. Spatial prior methods that favor solutions with high contrast between regions of different tissue types and/or penalize solutions with large variations within a tissue type are well suited for breast imaging because the different types of tissues that constitute the breast – mainly adipose and fibroglandular tissue – have distinct dielectric properties [10, 11]. Spatial priors have been previously added to microwave breast imaging algorithms [64, 52, 51, 50] using soft constraints in the regularization matrix to penalize solutions with large variations of the properties within a region. A system for coregistration of MRI and microwave breast imaging scans was reported in [52] and used in 2D microwave imaging studies with a human subject. Studies of microwave imaging with spatial priors were also reported using simulated and experimental data for simple phantoms in 2D [51, 50] and 3D [64].

In this paper we investigate a new method that we have recently proposed [65] for incorporating spatial prior information into the microwave inverse scattering algorithm. Our method also uses soft spatial prior constraints, but offers two unique features. First, the parameter that sets the weight of the spatial prior constraints is not directly linked to the L_2 regularization of the problem; consequently, the algorithm allows a wide range of variation of the reconstructed properties within each spatial prior region without affecting convergence of the solution of the inverse scattering problem. Secondly, the prior information is stored in a sparse matrix, leading to computational efficiencies that are particularly beneficial when implementing spatial prior methods in 3D.

We incorporate spatial prior information into the Distorted Born Iterative Method (DBIM), a conventional technique to solve the inverse scattering problem [39], and use numerical 3D phantoms to evaluate the performance of our algorithm. First, we image a locally homogeneous breast phantom to assess the accuracy of property estimation under conditions that closely match the assumptions of the algorithm configured with a hard constraint. Then, we conduct performance evaluation studies on realistic heterogeneous breast phantoms described in [66]. We investigate the effect of different levels of noise in the measured data and the choice of different weights for the spatial prior constraints. Finally, we evaluate the performance of the algorithm when there are errors in the prior information, namely shifts in the location of the *a priori* known regions, and discuss expected performance with other types of errors in the prior information.

3.3 Method

In this section we present an algorithm that incorporates spatial prior information into the DBIM. Similar modifications can be applied to other inverse scattering methods. We first provide a brief description of DBIM. A more detailed description can be found in [39] and [7]. Then we describe how we modify conventional DBIM to incorporate spatial prior information.

Conventional DBIM

The DBIM reconstructs the complex permittivity[1], ϵ, of a non-magnetic object inside a volume V from the scattered electric fields at the observation point $\mathbf{r}_{obs}$ outside the volume, by solving the following electric field integral equation:

---

[1] In this paper, we use the terms “dielectric properties” (i.e. relative permittivity and effective conductivity) and “complex permittivity” interchangeably.

$$\mathbf{E}^s(\mathbf{r}_{obs}) = \omega^2\mu_0 \int_V \mathbf{G}^b(\mathbf{r}_{obs}|\mathbf{r}')\mathbf{E}^t(\mathbf{r}')[\epsilon(\mathbf{r}') - \epsilon^b(\mathbf{r}')]d\mathbf{r}' \tag{3.1}$$

Here $\mathbf{E}^s$ is the scattered electric field, defined as the difference between the measured field when the scattering object is present and the incident field computed for the background dielectric profile, ϵ^b; $\mathbf{G}^b$ is the dyadic Green's function for the background; and $\mathbf{E}^t$ is the electric field inside the volume. The permeability of free space is denoted as μ_0 in (1). Measurements are taken for a set of source-observation channels at one or several discrete frequencies, ω. Each of the measurements corresponds to one equation in the form of (1).

The DBIM linearizes the problem by approximating $\mathbf{E}^t$ in the integrand of (1) as the incident electric field computed for the background dielectric profile. Full-wave computational electromagnetics simulations are used to compute the incident electric field inside V and at $\mathbf{r}_{obs}$, and the background Green's function. This step is denoted as the forward solution. The forward solution for all source-observation-frequency channels is used with the measured field data to form a system of scattering equations,

$$\mathbf{A}\mathbf{x} = \mathbf{b} \tag{3.2}$$

which is then solved to find an approximation to the contrast between the true properties and the background properties, $\mathbf{x} = \epsilon - \epsilon^b$. This is denoted as the inverse solution. The estimated contrast is used to update the properties of the background, and the forward and inverse solutions are repeated. This iterative process of updating the background by adding the latest estimate of the contrast, computing the forward solution (i.e., modifying $\mathbf{A}$ and $\mathbf{b}$) for that updated background profile, and then obtaining the inverse solution (i.e., solving for $\mathbf{x}$) is continued until the residual scattered fields are negligible. The reconstructed dielectric properties of the scatterer are given by the updated background once convergence has been reached.

A multi-frequency formulation of DBIM yields estimates for the dielectric properties by solving either for the real and imaginary parts of the complex permittivity at each frequency, or for the parameters in a frequency-dependent model for the complex permittivity. Here, we adopt the latter approach. Specifically, we use a single-pole Debye model as in [7]:

$$\epsilon(\omega) = \epsilon_0 \left(\epsilon_\infty + \frac{\Delta\epsilon}{1 + j\omega\tau} + \frac{\sigma_s}{j\omega\epsilon_0} \right) \tag{3.3}$$

where ϵ_0 is the permittivity of free space and the relaxation time constant τ is treated as a material-independent constant (set to 15 ps in our study, as in [7]). The unknowns are the three Debye parameters (ϵ_∞, $\Delta\epsilon$, and σ_s); thus, there are three unknowns per voxel. We assume k voxels in volume V, m source-observation channels, and f frequencies measured for each channel in this compact multi-frequency treatment of the linear system of (2). In this case $\mathbf{x} = [\mathbf{u}, \mathbf{v}, \mathbf{w}]'$, where $\mathbf{u} = \boldsymbol{\epsilon_\infty} - \boldsymbol{\epsilon}^b_{\boldsymbol{\infty}}$, $\mathbf{v} = \boldsymbol{\Delta\epsilon} - \boldsymbol{\Delta\epsilon}^b$, and $\mathbf{w} = \boldsymbol{\sigma_s} - \boldsymbol{\sigma}^b_{\boldsymbol{s}}$, is a $3k \times 1$ vector, $\mathbf{b}$ is a $2mf \times 1$ vector, and $\mathbf{A}$ is a $2mf \times 3k$ matrix. A more detailed description can be found in [7].

Since the problem $\mathbf{Ax} = \mathbf{b}$ is ill-posed, regularization techniques are required to obtain a unique solution. In this paper we adopt the conjugate gradient method for least square (CGLS) error minimization as implemented in [7] to regularize the solution. The degree of regularization is inversely proportional to the number of CGLS iterations. To determine an appropriate termination condition for the CGLS algorithm, we use an L-curve method, in which the solution norm $\|\mathbf{x}_i\|_2$ is plotted against the residual norm $\|\mathbf{Ax}_i - \mathbf{b}\|_2$ for CGLS iterations $i = 1, 2, 3 \ldots$. Usually this plot depicts an "L" shaped curve in the case of ill-posed problems. The early termination condition is determined by the number of iterations at which the curvature of the L-curve is maximum. This achieves a reduction in the residual while keeping the solution bounded.

DBIM with spatial priors

DBIM with spatial priors (DBIM-SP) assumes we have prior information about the structure of the breast. In particular, it assumes knowledge of the locations of different types of tissues, obtained from a high resolution image of the breast that has been segmented into regions corresponding to the different tissue types. DBIM-SP uses the fact that different tissues have different electrical properties, but within the same tissue type the properties variation is relatively small [10, 11].

Assuming we start with a homogeneous background, we constrain the solution, $\mathbf{x}$, such that if two voxels belong to the same tissue type, or equivalently, to the same region, the update of the properties of the two voxels should be similar. This suggests solving an augmented system of equations comprising not only the electric field integral equations, but also equations of the form $-x_i + x_j = 0$ for voxels i and j in the same region. Consider, for example, a problem consisting of two regions. For each set of unknowns ($\mathbf{u}$, $\mathbf{v}$, and $\mathbf{w}$) we can write the set of additional equations in matrix form as $\mathbf{M_0 u} = \mathbf{0}$, $\mathbf{M_0 v} = \mathbf{0}$, and

$\mathbf{M_0 w} = \mathbf{0}$, where $\mathbf{M_0}$ is of the form:

$$\mathbf{M_0} = \left[\begin{array}{ccccc|ccccc} -1 & 1 & 0 & 0 & \cdots & 0 & 0 & 0 & 0 & \cdots \\ -1 & 0 & 1 & 0 & \cdots & 0 & 0 & 0 & 0 & \cdots \\ -1 & 0 & 0 & 1 & \cdots & 0 & 0 & 0 & 0 & \cdots \\ \vdots & \vdots & \vdots & \vdots & \ddots & \vdots & \vdots & \vdots & \vdots & \ddots \\ \hline 0 & 0 & 0 & 0 & \cdots & -1 & 1 & 0 & 0 & \cdots \\ 0 & 0 & 0 & 0 & \cdots & -1 & 0 & 1 & 0 & \cdots \\ 0 & 0 & 0 & 0 & \cdots & -1 & 0 & 0 & 1 & \cdots \\ \vdots & \vdots & \vdots & \vdots & \ddots & \vdots & \vdots & \vdots & \vdots & \ddots \end{array}\right] \tag{3.4}$$

The upper left block of $\mathbf{M_0}$ enforces the constraint of equal properties in the first region, while the lower right block does so for the second region. Matrix $\mathbf{M_0}$ is highly sparse with dimensions $(k-2) \times k$. In the general case where there are n spatial prior regions, the dimensions would be $(k-n) \times k$. All spatial prior constraints can be summarized as $\mathbf{Mx} = \mathbf{0}$, where

$$\mathbf{M} = \begin{bmatrix} \mathbf{M_0} & \mathbf{0} & \mathbf{0} \\ \mathbf{0} & \mathbf{M_0} & \mathbf{0} \\ \mathbf{0} & \mathbf{0} & \mathbf{M_0} \end{bmatrix} \tag{3.5}$$

We introduce (5) as a soft constraint by minimizing:

$$\|\mathbf{Ax} - \mathbf{b}\|^2 + \lambda^2 \|\mathbf{Mx}\|^2. \tag{3.6}$$

The constraint parameter λ is used to weigh errors in satisfying the spatial prior constraints against errors in satisfying the linearized electric field integral equations. A large λ ensures the properties difference between two voxels in a region is small, while a small λ gives more importance to matching the electric field integral equations. Thus a small λ reduces emphasis on the spatial prior constraints and allows greater properties variation within a region.

To solve (6) we define an augmented system of equations as $\mathbf{A'x} = \mathbf{b'}$ where $\mathbf{A'} = [\mathbf{A}|\lambda\mathbf{M}]^T$, $\mathbf{b'} = [\mathbf{b}|\mathbf{0}]^T$. We use CGLS with an early termination to further regularize the solution. However, the number of CGLS iterations chosen by the CGLS L-curve algorithm in DBIM-SP tends to be much larger than that chosen in DBIM, especially when the spatial prior constraint parameter λ is large. This is because the additional spatial prior equations of DBIM-SP reduce the ill-posedness of the problem, and therefore it requires less regularization than conventional DBIM.

There are other options besides this choice of $\mathbf{M_0}$ for achieving smoothness within each region. Examples include comparing each voxel to an adjacent voxel in the same region (i.e., a first order differential regularizer within each region) and comparing each voxel to the average of the voxels in the same region (i.e., a Laplacian regularizer within each region). In the case of a hard constraint, all these approaches are equivalent. In the soft constraint formulation, these approaches will yield slightly different results. We have chosen the matrix $\mathbf{M_0}$ in (4) for simplicity of implementation.

3.4 Models and implementation details

Breast phantoms

Our testbed for investigating the performance of DBIM-SP included a locally homogeneous breast phantom and two realistic breast phantoms derived from MRIs of healthy women [66]: a Class 3 “heterogeneously dense” phantom (ID number 062204 in the online University of Wisconsin repository [67]), and a Class 2 “scattered fibroglandular” (ID number 010204) phantom. Figure 3.1 shows the relative permittivity of the phantoms at 2 GHz. The locally homogeneous phantom has the basic structure of the Class 3 phantom but is composed only of homogeneous adipose tissue and homogeneous fibroglandular tissue. This phantom allows us to evaluate the accuracy of property estimation using DBIM-SP under a baseline scenario in which the phantom matches the assumptions of the algorithm operating under a hard spatial prior constraint. The Class 3 and Class 2 phantoms were chosen as examples of two different types of breast densities. The Class 2 breast phantom has a larger volume than the Class 3 phantom, and consists of mostly adipose tissue with a few small scattered regions of fibroglandular tissue.

The frequency-dependent complex permittivities of skin [68] and breast tissues [11] in the phantoms were modeled using single-pole Debye models as in [7] over the frequency range of 0.5-3.5 GHz (see table I in [7] for the list of Debye parameters used in our models). The skin was assumed to be homogeneous with a thickness of 2 mm.

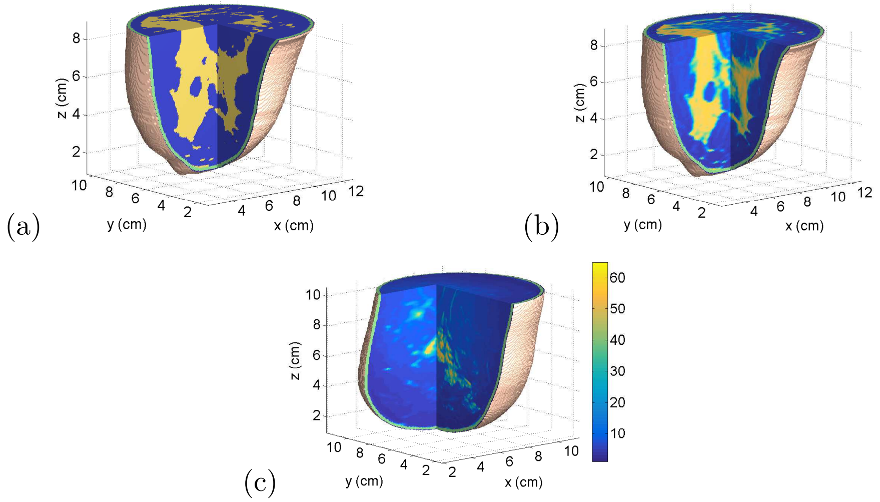

Figure 3.1: Relative permittivity at 2 GHz of breast phantoms used in the study. (a) Locally homogeneous phantom, (b) Class 3 phantom (heterogeneously dense), and (c) Class 2 phantom (scattered fibroglandular).

Simulated array measurements

The simulated array comprised 40 dipoles surrounding a particular breast phantom, all immersed in a lossless medium ($\epsilon_r = 2.6$). The dipoles were oriented vertically (z-polarized) and were arranged on a cylindrical surface in five coronal rings, with a minimum distance of 1 cm to the skin surface of the breast. The rings were equally spaced along the vertical extent of the phantom, and they were rotated 22.5° with respect to adjacent rings to maximize the distance between the dipoles.

Simulated array measurements were calculated using the finite-difference time-domain (FDTD) method [69] on a 0.5 mm grid. FDTD simulates the propagation of electromagnetic waves by solving Maxwell's differential equations in the time domain. Each transmitting dipole was excited by a modulated Gaussian pulse and the measurements at the receiving antennas were transformed to the frequency domain and recorded at 1.0, 1.5, 2.0, and 2.5 GHz. We use data only at four discrete frequencies to emulate the type of data we would obtain with a realistic experimental array as in [70, 71].

We added white Gaussian noise to the recorded electric field measurements to simulate different signal-to-noise ratios (SNR). Here, we define the SNR as the ratio between the total received power across all channels and the total power of the noise added to the channels. Previous reports of DBIM performance for noisy simulated array measurements indicated a significant degradation of imaging accuracy for SNR levels below about 20 dB (see Fig. 17 in [21]). Therefore we chose SNR levels of 30 dB and 10 dB as representative examples of lower and higher noise scenarios, respectively. An SNR of 30 dB for the simulated array used in this study corresponds to a noise floor that is approximately 90 dB below the transmitted power [7]. This is on the conservative end of typical noise floor estimates (see, for example, [64] and [8]).

Forward solver and inverse solution formulations

The initial guess used in our DBIM and DBIM-SP algorithms consisted of a spatially homogeneous interior with properties equal to the average properties of the interior of the breast. Gao et al [72] demonstrated that this is a robust choice of initial guess for the DBIM problem. In our investigation we have confirmed that DBIM-SP is far more robust than DBIM to the properties chosen for a spatially homogeneous initial guess. Specifically, DBIM-SP converges to a meaningful solution in approximately 10 iterations for homogeneous initial guesses with properties ranging from 100% fibroglandular (0% adipose) to 20% fibroglandular (80% adipose) tissues.

In each iteration, the Green's function and interior incident fields in the DBIM and DBIM-SP were calculated using the FDTD method on a 2 mm grid. The grid used in the forward solver in the reconstruction was chosen to be coarser than the grid used for data acquisition to introduce some model error and thereby avoid the so-called "inverse crime". The **A** matrix and **b** vector for the inverse solution were created from equations for every source-observation channel and for each of the four recorded frequencies. The dielectric properties of the immersion medium, and the dielectric properties, location, and thickness of the skin were considered known; therefore the unknowns correspond only to the Debye parameters for each voxel in the interior of the breast (as in [7]). The number of voxels in the interior of the breast in the locally homogeneous and Class 3 phantoms was $41,578$ and in the Class 2 phantom it was $65,003$. The number of source-observation channels for the 40-element array was 780 after eliminating the monostatic and redundant channels. Thus with $f = 4$, the $2mf$ number of elements in **b** was 6,240.

Spatial priors

Figure 3.2 shows the two regions used as spatial prior in the DBIM-SP for each phantom. The black region corresponds to adipose tissue and white region corresponds to fibroglandular tissue. Only two regions were considered since the phantoms do not have lesions. The regions were derived by applying a threshold on the phantom's properties that yielded an appropriate separation of the two tissue types. Note that because the data acquisition takes place on a 0.5 mm grid, and the reconstruction on a 2 mm grid, the spatial prior regions do not match the regions of the phantom exactly.

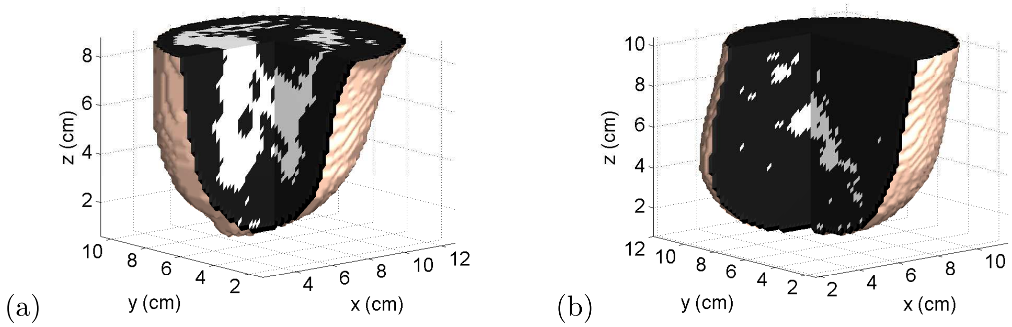

Figure 3.2: Spatial prior regions for each phantom. Black corresponds to the adipose region, and white corresponds to the fibroglandular region. (a) Regions used for the locally homogeneous phantom (Fig. 3.1(a)) and the Class 3 phantom (Fig. 3.1(b)). (b) Regions used for the Class 2 phantom (Fig. 3.1(c)).

Choice of the spatial prior constraint parameter

The amount of variation of the properties that is allowed in each spatial prior region depends on the choice of the constraint parameter λ. We identify values of λ that will yield well behaved and predictable results by plotting the normalized residual squared error of the spatial prior constraints ($\|\mathbf{Mx}\|_2^2$) versus the normalized residual squared error of the electric field integral equations ($\|\mathbf{Ax}-\mathbf{b}\|_2^2$). To do so we solve (6) for a wide range of values of λ using a homogeneous initial guess and a sufficiently large number of CGLS iterations. The number of CGLS iterations is determined by a stopping criteria based on the difference between the norms of the residual of two successive iterations. Our choice eliminates the L_2 regularization provided by the early termination of CGLS, and therefore does not obscure the effect of λ on the solution. The use of a warm start initialization between subsequent values of λ shortens considerably the computational time for solving the system. Figure 3.3 shows $\|\mathbf{Mx}\|_2^2$ versus $\|\mathbf{Ax}-\mathbf{b}\|_2^2$, both normalized by $\|\mathbf{b}\|_2^2$, for the Class 3 and Class 2 phantoms for 200 values of λ varying between 1×10^{-7} and 2×10^{-1}, while using 60 CGLS iterations. The plots depict an L-shape, reflecting the trade-off between satisfying the spatial prior constraints and satisfying the electric field integral equations. We denote the value of λ that corresponds to the point of maximum curvature of the L-curve as λ^*. Values of the constraint parameter that are smaller than λ^* put small to negligible weight on the spatial prior constraints, while values of the constraint parameter larger than λ^* noticeably limit the amount of variation in each spatial prior region.

Once λ^* is determined we perform DBIM-SP as described in section II.B.

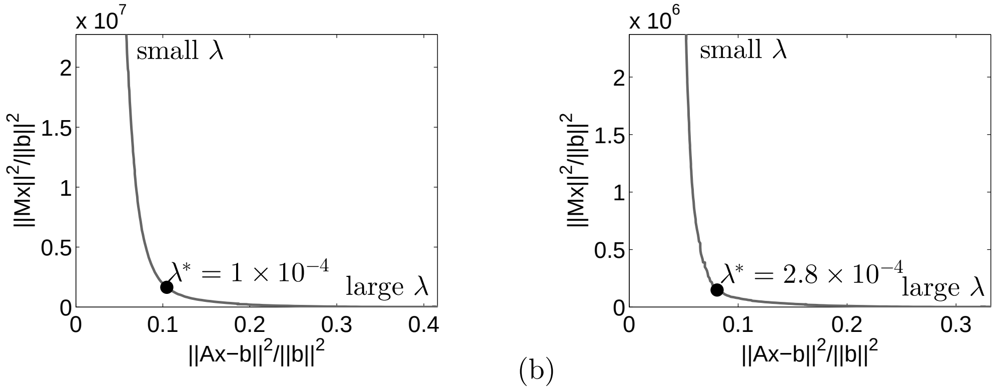

(a) (b)

Figure 3.3: Norm squared of normalized residual of spatial prior constraints versus norm squared of normalized residual of electric field integral equations for the first iteration of DBIM-SP, for a wide range of values of λ. The point of maximum curvature is denoted by λ^*. (a) Class 3 phantom. (b) Class 2 phantom.

3.5 Results

Locally homogeneous phantom

Figure 3.4 shows the actual and reconstructed dielectric properties with DBIM-SP ($\lambda = 500\lambda^*$) of adipose and fibroglandular tissue types for the locally homogeneous phantom in a low noise scenario (SNR = 30 dB). A relatively large λ was chosen to assess the accuracy of the estimated properties in an assumed locally homogeneous environment. The estimated relative permittivity and effective conductivity is accurate for both tissue types over the entire frequency range of the reconstructed solution (1.0 - 2.5 GHz).

We define the mean absolute error (MAE) associated with the reconstruction of the dielectric properties in a region with N voxels. The following expression illustrates the MAE metric for the relative permittivity (or effective conductivity, if ϵ_r is replaced by σ_{eff}) at a specific frequency:

$$\text{MAE} = \frac{1}{N}\sum_{i=1}^{N} |\epsilon_{r,i}^{\text{true}} - \epsilon_{r,i}^{\text{estimated}}| \tag{3.7}$$

We compute the MAE for the interior of the fibroglandular region, the interior of the adipose region, and both regions. Table 3.1 shows the results. The 2-GHz relative permittivity results for DBIM-SP with $\lambda = 500\lambda^*$ show an improvement factor of 20.5, 9.0, and 13.2 over standard DBIM for the adipose, fibroglandular, and combined regions, respectively. The corresponding improvement factors for effective conductivity at 2 GHz are 5.7, 36.8, and 8.0.

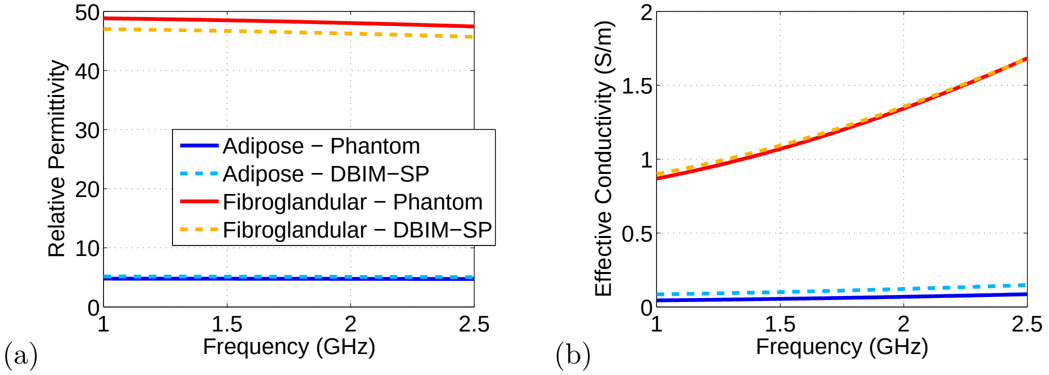

Figure 3.4: Comparison of the true (solid) and DBIM-SP reconstructed (dashed) dielectric properties in the adipose (light/dark blue) and fibroglandular (red/orange) tissue regions of the locally homogeneous breast phantom.

Class 3 phantom: heterogeneously dense tissue

Figures 3.5 and 3.6 show cross-sectional cuts (coronal, sagittal, and axial views) of the relative permittivity and effective conductivity, respectively, at 2 GHz of the Class 3 breast phantom (first row) and three different reconstructions for a 30 dB SNR: conventional DBIM (second row), DBIM-SP with a large λ, i.e., $\lambda = 500\lambda^*$ (third row), and DBIM-SP

TABLE 3.1: Mean absolute error (MAE) for the reconstruction of the locally homogeneous phantom with a 30 dB SNR.

Relative permittivity at 2 GHz			
	Adipose	Fibroglandular	Combined
DBIM	7.37	16.32	9.63
DBIM-SP ($\lambda = 500\lambda^*$)	0.36	1.81	0.73
Effective conductivity at 2 GHz			
	Adipose	Fibroglandular	Combined
DBIM	0.300	0.478	0.345
DBIM-SP ($\lambda = 500\lambda^*$)	0.053	0.013	0.043

with a relatively small λ, i.e., $\lambda = 5\lambda^*$ (fourth row). The reconstruction with conventional DBIM shows evidence of correctly identifying the general regions of adipose and fibroglandular tissue, but it suffers from blurred boundaries between the different tissues and inaccurate properties estimation. In particular, it significantly underestimates the properties of the fibroglandular tissue. In contrast, DBIM-SP preserves the edges between the different tissues, and is more accurate in the estimation of the properties. The reconstruction that results from using a large λ exhibits two locally homogeneous regions, each with properties close to the average properties of the tissues in respective regions of the phantom. The average relative permittivities at 2 GHz of the phantom are $\epsilon_r = 43$ for fibroglandular tissue and $\epsilon_r = 6$ for adipose tissue, while the DBIM-SP reconstruction yields relative permittivities of $\epsilon_r = 45$ and $\epsilon_r = 5$ for each respective region. The DBIM-SP reconstruction with a small λ preserves the boundaries between the tissues while capturing some of the local heterogeneity within the tissues.

Figure 3.7 shows cumulative distributions of the properties of each region for the phantom, the reconstruction using conventional DBIM, and reconstructions using DBIM-SP with different values of λ. The cumulative distribution plots display the percentage of voxels in the phantom and its reconstructions (y-axis) that are below a certain relative permittivity or effective conductivity (x-axis). Figure 3.7 clearly depicts how DBIM overestimates the dielectric properties of adipose tissue and underestimates those of fibroglandular tissue. Also, the cumulative distributions for DBIM are relatively smooth and flat compared to the cumulative distribution of the properties of the original phantom. This is because DBIM smooths the variation of the properties inside the whole imaging region. In contrast, DBIM-SP with $\lambda = 500\lambda^*$ results in no variation of the properties in each region, and as we decrease λ we obtain variations of the properties that tend to follow those of the original phantom. DBIM-SP with $\lambda = 0.5\lambda^*$ performs similarly to DBIM, indicating that the role of the spatial prior constraints for small λ is negligible, as expected.

Table 3.2 shows the MAE analysis for these reconstructions. We see that the improvement associated with the use of spatial priors is still very considerable in this far more complex scenario of a heterogeneously dense phantom. For example, the MAE for the relative permittivity at 2 GHz in the combined regions is reduced by a factor of 5.0 for DBIM-SP using a large $\lambda = 500\lambda^*$ and a factor of 3.3 for DBIM-SP using a moderate $\lambda = 5\lambda^*$ relative to standard DBIM.

Figures 3.8, 3.9, and 3.10 show the cross sections and cumulative distributions of the relative permittivity and effective conductivity at 2 GHz of the phantom and the reconstructions for a higher level of noise (SNR = 10 dB). We observe that DBIM completely breaks down at this level of SNR (Figures 3.8 and 3.9, second row), while DBIM-SP continues to perform well. The cumulative distribution of DBIM is much flatter at high noise, while the performance of DBIM-SP is very similar to the low noise results shown in Figure 3.7, even for small values of λ. The robustness to noise of DBIM-SP can also be appreciated by inspecting the MAE results shown in Table 3.3. The MAE for the DBIM-SP reconstructions for $\lambda = 500\lambda^*$ and $\lambda = 5\lambda^*$ are similar to the MAE obtained for these reconstructions in the low noise scenario.

In this section, we presented both relative permittivity and effective conductivity results from all of our dielectric properties images. The results illustrated that the relative permittivity and effective conductivity follow similar trends. That observation holds true for all imaging experiments in this study. Therefore, we only show results for the relative permittivity in the remaining sections of this paper to save space.

Class 2 phantom: scattered fibroglandular tissue

Figure 3.11 shows coronal, sagittal, and axial views of the relative permittivity at 2 GHz of the Class 2 breast phantom (first row) and three different reconstructions for a 30 dB SNR: conventional DBIM (second row), DBIM-SP with a relatively large λ, i.e., $\lambda = 500\lambda^*$, and DBIM-SP with a small λ, i.e., $\lambda = 5\lambda^*$. A comparison between Fig. 3.11(a) and Fig. 3.5(a) highlights the significant differences in the breast volume and tissue composition of the Class 2 and Class 3 phantoms. Despite these differences, the general imaging performance trends observed in the Class 3 reconstructions (Fig. 3.5(b),(c),(d)) hold here

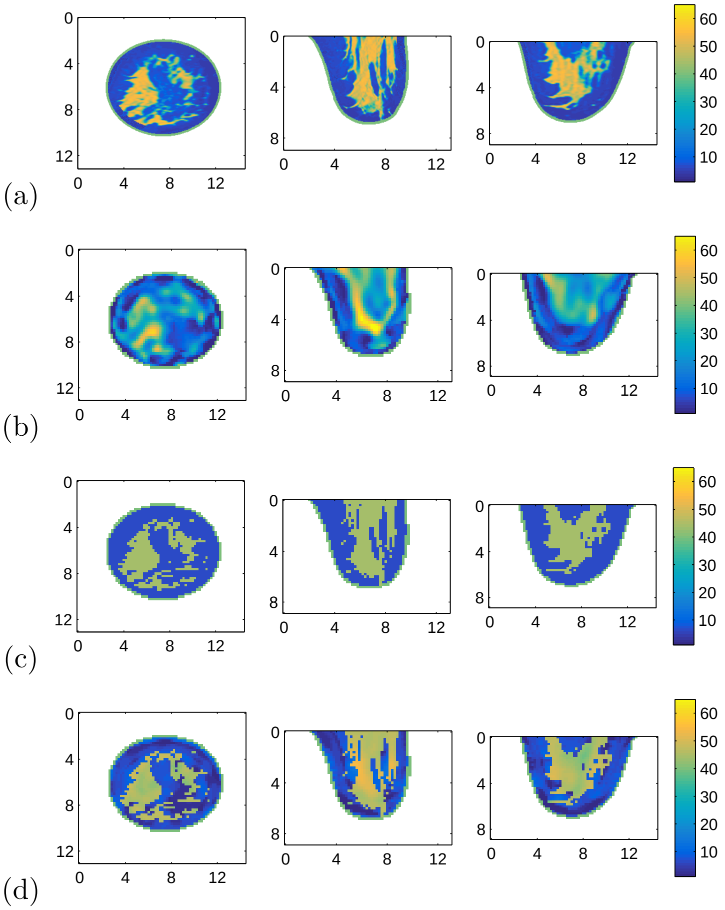

Figure 3.5: Coronal (left column), sagittal (middle column), and axial (right column) cross-sections of the relative permittivity at 2 GHz for the (a) Class 3 breast phantom, (b) standard DBIM reconstruction, (c) DBIM-SP reconstruction ($\lambda = 500\lambda^*$), and (d) DBIM-SP reconstruction ($\lambda = 5\lambda^*$). All reconstructions were obtained for 30 dB SNR. (Axes in cm.)

as well. Namely, DBIM once again is able to reconstruct some of the fibroglandular tissue, but those tissue properties are underestimated and the boundaries are blurred. In contrast, DBIM-SP achieves a high-resolution reconstruction with more accurate dielectric properties estimation. DBIM-SP with a relatively large λ yields spatially invariant properties in each primary tissue region of the image that are similar to the average properties in the corresponding regions of the phantom, while DBIM-SP with a smaller λ preserves

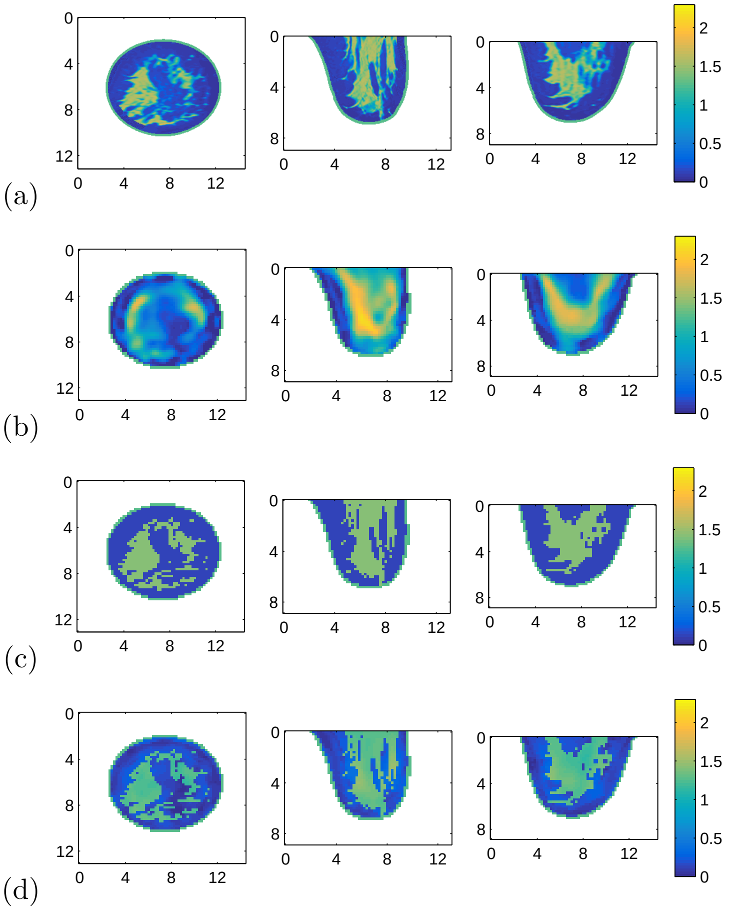

Figure 3.6: Coronal (left column), sagittal (middle column), and axial (right column) cross-sections of the effective conductivity at 2 GHz for the (a) Class 3 breast phantom, (b) standard DBIM reconstruction, (c) DBIM-SP reconstruction ($\lambda = 500\lambda^*$), and (d) DBIM-SP reconstruction ($\lambda = 5\lambda^*$). All reconstructions were obtained for 30 dB SNR. (Axes in cm.)

boundaries while capturing some of the mild properties variation within a specific tissue region.

Figure 3.12 shows the cumulative distributions of the relative permittivity at 2 GHz of each region for the Class 2 phantom, its conventional DBIM reconstruction, and several reconstructions using DBIM-SP with different values of λ. Similarly to the trends depicted in Fig. 3.7, here we see that DBIM smooths the properties of the phantom and underesti-

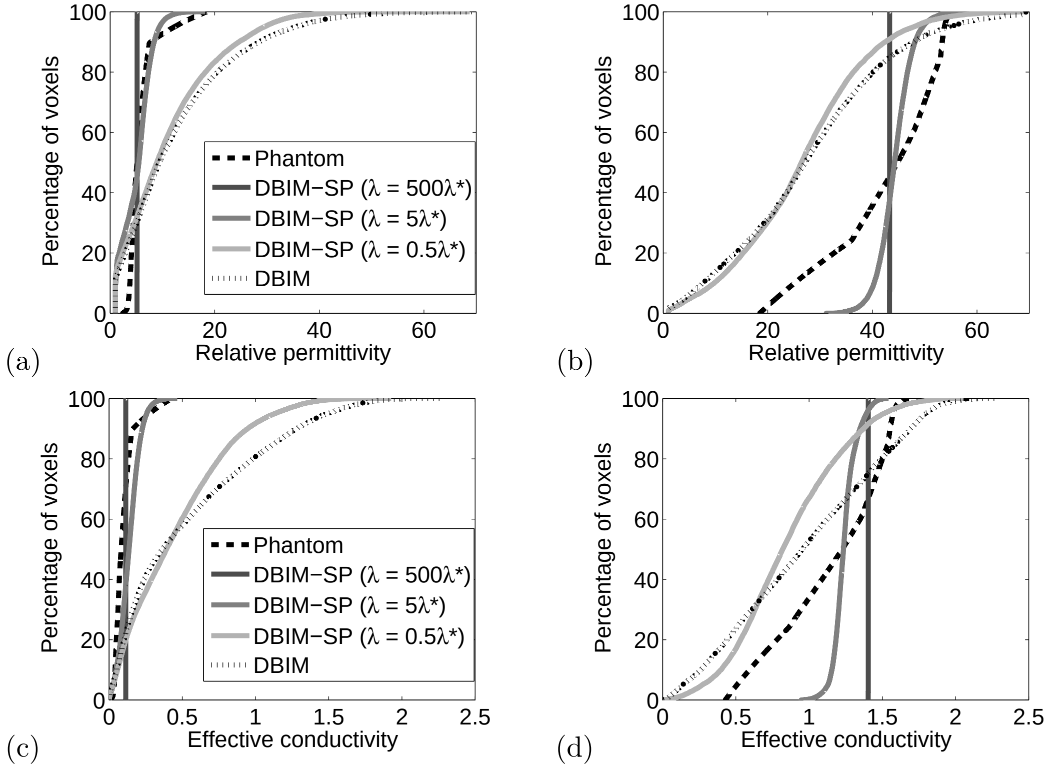

Figure 3.7: Cumulative distributions of the relative permittivity (top row) and effective conductivity (bottom row) at 2 GHz for Class 3 breast phantom reconstructions with 30 dB SNR. (a),(c) Adipose tissue region. (b),(d) Fibroglandular tissue region.

mates the properties of the fibroglandular tissue. Also, DBIM-SP with a large λ does not allow variations in each region, but as we decrease λ we start to capture some heterogeneity until DBIM-SP performs similarly to DBIM when $\lambda = 0.5\lambda^*$.

The MAE analysis shown in Table 3.4 indicates that the errors obtained for this phantom with DBIM and with DBIM-SP for different values of λ are smaller than for the Class 3 phantom, yet there is still a considerable reduction in the errors relative to standard DBIM performance. The error in the combined regions is reduced by factors of 1.6 and 3.4 with DBIM-SP using $\lambda = 500\lambda^*$ and $\lambda = 0.5\lambda^*$ respectively.

TABLE 3.2: Mean absolute error (MAE) for the reconstruction of the Class 3 phantom with a 30 dB SNR.

Relative permittivity at 2 GHz			
	Adipose	Fibroglandular	Combined
DBIM	7.91	18.34	10.54
DBIM-SP ($\lambda = 500\lambda^*$)	0.93	5.65	2.12
DBIM-SP ($\lambda = 5\lambda^*$)	2.28	5.80	3.17
DBIM-SP ($\lambda = 0.5\lambda^*$)	6.41	18.49	9.46
Effective conductivity at 2 GHz			
	Adipose	Fibroglandular	Combined
DBIM	0.376	0.507	0.409
DBIM-SP ($\lambda = 500\lambda^*$)	0.041	0.144	0.067
DBIM-SP ($\lambda = 5\lambda^*$)	0.069	0.179	0.097
DBIM-SP ($\lambda = 0.5\lambda^*$)	0.312	0.491	0.357

TABLE 3.3: Mean absolute error (MAE) for the reconstruction of the Class 3 phantom with a 10 dB SNR.

Relative permittivity at 2 GHz			
	Adipose	Fibroglandular	Combined
DBIM	36.67	25.33	33.81
DBIM-SP ($\lambda = 500\lambda^*$)	0.93	6.27	2.28
DBIM-SP ($\lambda = 5\lambda^*$)	2.33	6.01	3.26
DBIM-SP ($\lambda = 0.5\lambda^*$)	9.72	21.37	12.66
Effective conductivity at 2 GHz			
	Adipose	Fibroglandular	Combined
DBIM	0.716	0.643	0.698
DBIM-SP ($\lambda = 500\lambda^*$)	0.041	0.144	0.067
DBIM-SP ($\lambda = 5\lambda^*$)	0.052	0.225	0.096
DBIM-SP ($\lambda = 0.5\lambda^*$)	0.275	0.706	0.383

Errors in prior information

In this section we provide results from an investigation of DBIM-SP performance when the prior information contains greater errors than the mismatch that arises due to the discretization of the imaging region. Namely, we consider two types of error: i) offsets in the spatial prior regions relative to the phantom, and ii) error in the size of one of

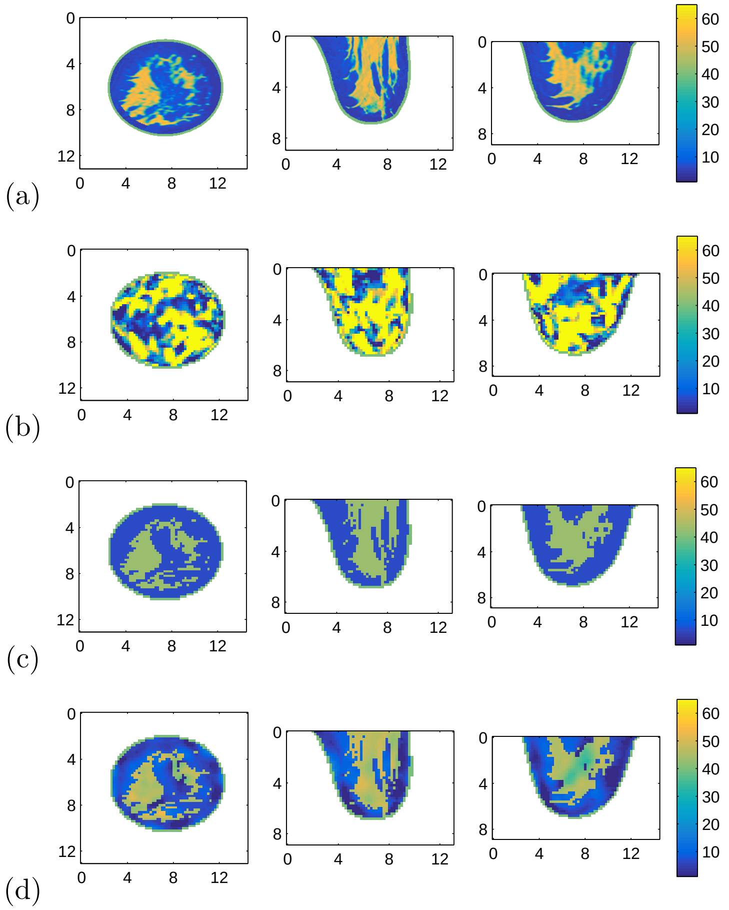

Figure 3.8: Coronal (left column), sagittal (middle column), and axial (right column) cross-sections of the relative permittivity at 2 GHz for the (a) Class 3 breast phantom, (b) standard DBIM reconstruction, (c) DBIM-SP reconstruction ($\lambda = 500\lambda^*$), and (d) DBIM-SP reconstruction ($\lambda = 5\lambda^*$). All reconstructions were obtained for 10 dB SNR. (Axes in cm.)

the spatial prior regions. The offsets represent shifts either to the right or to the left in the coronal plane. This type of error could occur in practice due to a misalignment between the reference coordinates in the MRI (or any other source of the spatial priors) and the microwave scan. The error in the size of one of the spatial prior regions could occur due to errors in image segmentation, for example. We present this type of error as a complementary scenario to the case of an offset to study the robustness of DBIM-SP to

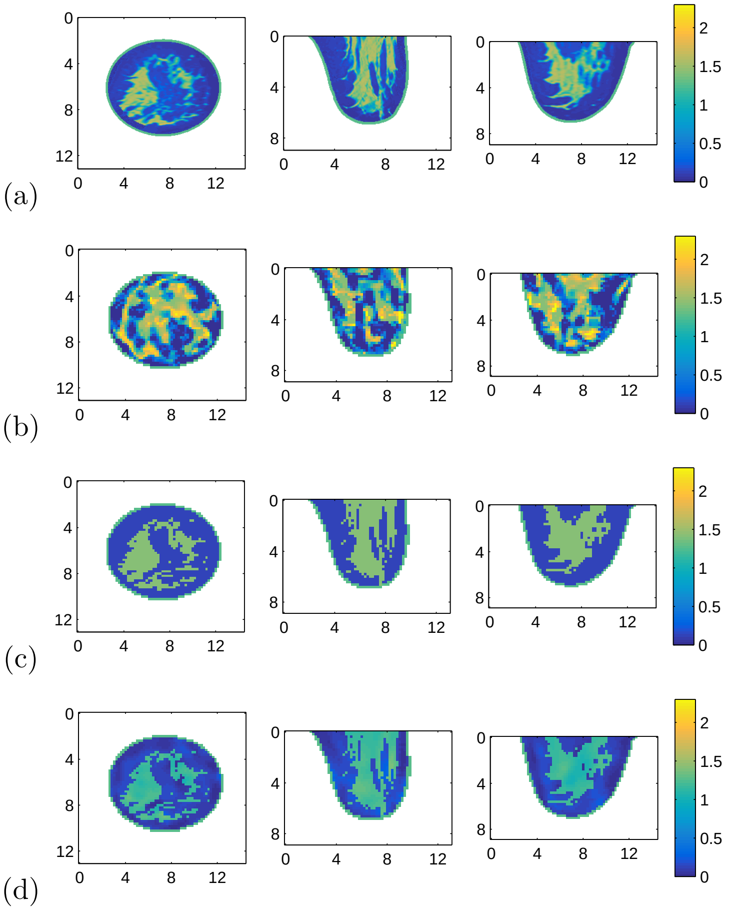

Figure 3.9: Coronal (left column), sagittal (middle column), and axial (right column) cross-sections of the effective conductivity at 2 GHz for the (a) Class 3 breast phantom, (b) standard DBIM reconstruction, (c) DBIM-SP reconstruction ($\lambda = 500\lambda^*$), and (d) DBIM-SP reconstruction ($\lambda = 5\lambda^*$). All reconstructions were obtained for 10 dB SNR. (Axes in cm.)

different types of errors.

We use a moderate λ (i.e. $\lambda = 5\lambda^*$) to exploit the soft constraints that allow reconstructions with heterogeneity within each region. The rationale behind this choice is that the soft constraint provides flexibility to allow the algorithm to adjust for errors due to a mismatch of the spatial prior. A large λ (e.g. $\lambda = 500\lambda^*$) estimates the average properties of the tissues in each spatial prior region, and therefore the reconstruction has no flexibility

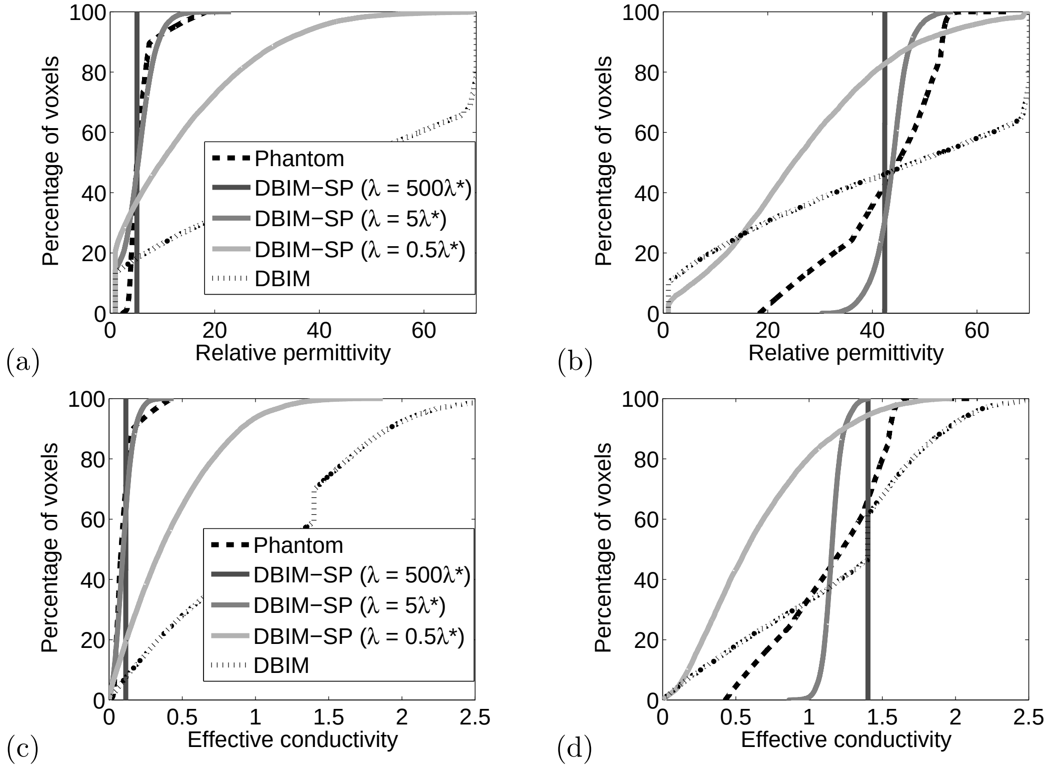

Figure 3.10: Cumulative distributions of the relative permittivity (top row) and effective conductivity (bottom row) at 2 GHz for Class 3 breast phantom reconstructions with 10 dB SNR. (a),(c) Adipose tissue region. (b),(d) Fibroglandular tissue region.

TABLE 3.4: Mean absolute error (MAE) for the reconstruction of the Class 2 phantom with a 30 dB SNR.

Relative permittivity at 2 GHz			
	Adipose	Fibroglandular	Combined
DBIM	2.41	19.32	2.63
DBIM-SP ($\lambda = 500\lambda^*$)	1.55	7.35	1.62
DBIM-SP ($\lambda = 5\lambda^*$)	0.69	6.67	0.77
DBIM-SP ($\lambda = 0.5\lambda^*$)	1.75	20.12	1.98

to adjust the reconstructed properties locally where mismatches occur. Figure 3.13 shows images of the Class 3 phantom using DBIM-SP with a moderate value for λ ($\lambda = 5\lambda^*$) for our study of the impact of offsets of the spatial prior regions in a low noise scenario

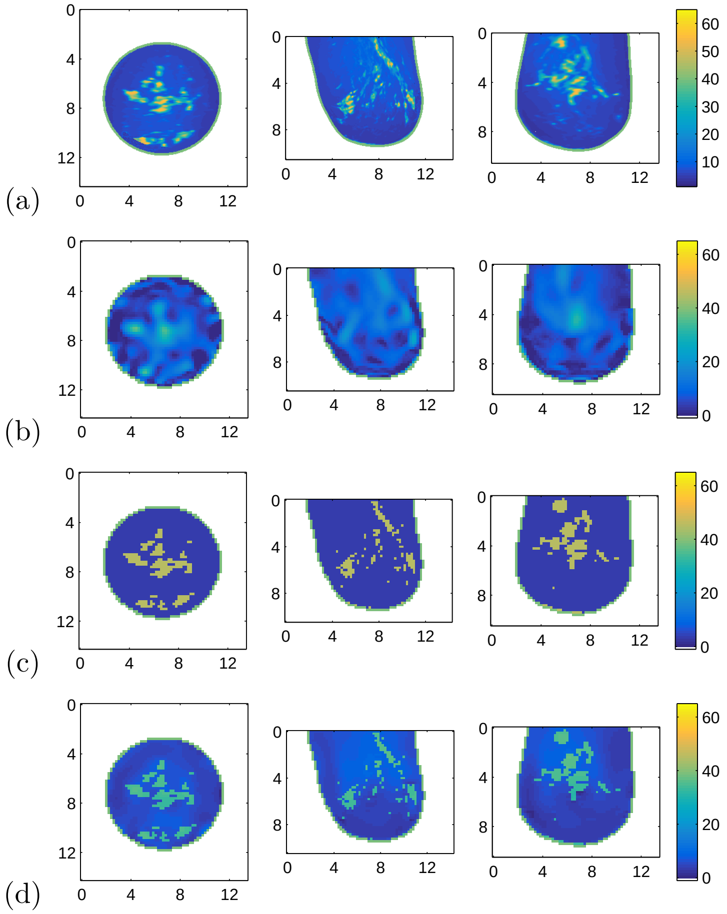

Figure 3.11: Coronal (left column), sagittal (middle column), and axial (right column) cross-sections of the relative permittivity at 2 GHz for the (a) Class 2 breast phantom, (b) standard DBIM reconstruction, (c) DBIM-SP reconstruction ($\lambda = 500\lambda^*$), and (d) DBIM-SP reconstruction ($\lambda = 5\lambda^*$). All reconstructions were obtained for 30 dB SNR. (Axes in cm.)

(SNR = 30 dB). The first row shows the reconstruction with no errors in the prior, the second row uses a prior in which the fibroglandular region was shifted 4 mm to the left, and the third row uses a prior in which the fibroglandular region was shifted 4 mm to the right. The results show that the algorithm is robust to errors in the prior information. We observe that the algorithm compensates for the mismatches between the tissues and the spatial prior regions by changing the reconstructed properties within each region. In the

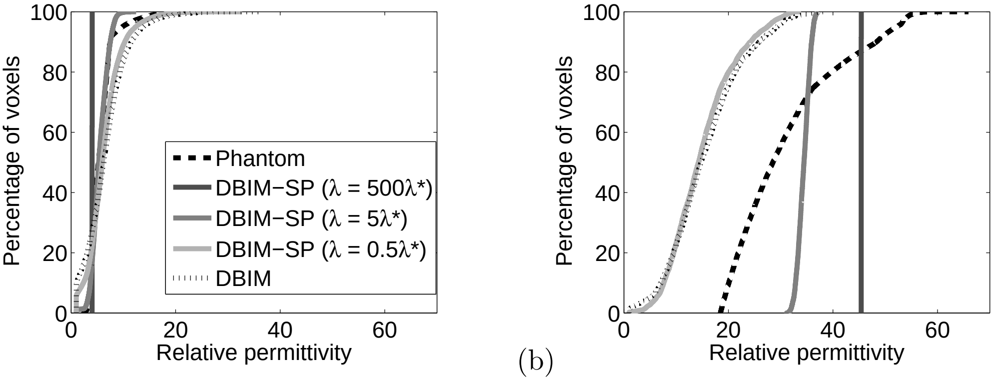

(a) (b)

Figure 3.12: Cumulative distributions of the relative permittivity at 2 GHz for Class 2 reconstructions with 30 dB SNR. (a) Adipose tissue region. (b) Fibroglandular tissue region.

third row (prior shifted to the right) we see in the coronal view (first column) that the estimation of properties of the adipose region where there is supposed to be fibroglandular tissue is considerably higher than in the rest of the adipose region. In the sagittal view (second column) we see that there is a large mismatch between the spatial prior regions and the true tissue distribution, and the reconstruction compensates for the mismatch by raising the properties of the adipose tissue where there is a mismatch. In the second row (prior shifted to the left) we observe a similar effect.

Table 3.5 shows the MAE for the reconstructions when there are erroneous shifts in the spatial prior regions for the Class 3 breast phantom in low noise (30 dB SNR) and high noise (10 dB SNR) scenarios. We observe a slight degradation of the performance as the mismatch increases, especially for rightward shifts of the fibroglandular region. The performance for shifts to the left and to the right does not degrade in a similar way due to the asymmetry and heterogeneity of the phantom. By comparing these results to those in Table 3.2 for conventional DBIM in a low noise scenario, we see that DBIM-SP yields a lower MAE than conventional DBIM for up to 4 mm of mismatch.

Another way to visualize the effect of errors in the prior information is to compare the average properties of each tissue in the reconstructions. Figure 3.14 shows the average properties of the adipose and fibroglandular tissues in the reconstructions of the Class 3 phantom using DBIM-SP (with $\lambda = 5\lambda^*$) for different amounts of erroneous shifts in the prior with 30 dB and 10 dB SNR. The true average (phantom average) and the average obtained using conventional DBIM in a low noise scenario are also shown in the plots. The estimation of the average properties of each tissue type is still accurate for small errors in the prior. Interestingly, DBIM-SP with errors in the prior performs better than DBIM at estimating the average properties of each tissue for up to a 6 mm error (shift) in the prior. Similar performance degradation due to shifts in the prior are observed at low SNR for both MAE and average properties. The addition of noise does not increase sensitivity to this type of error in the prior information.

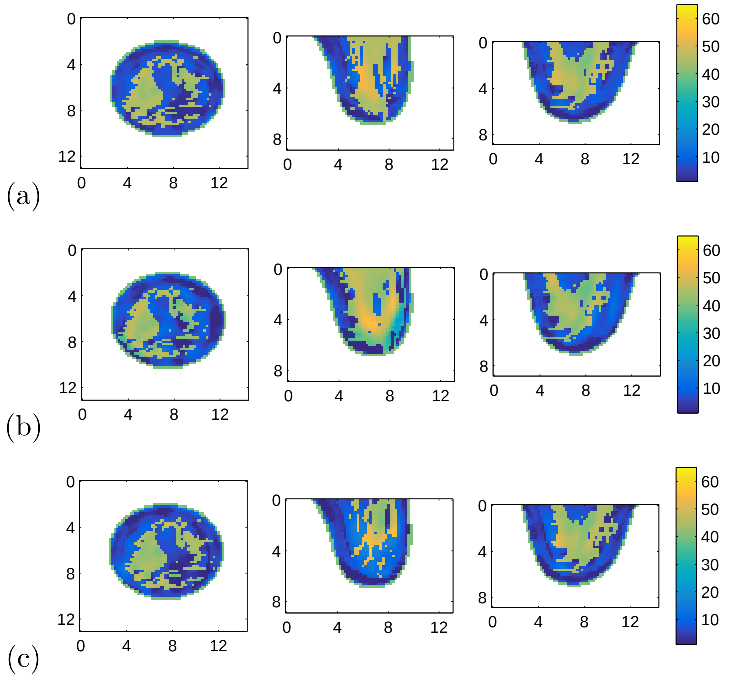

Figure 3.13: Coronal (left column), sagittal (middle column), and axial (right column) cross-sections of the relative permittivity at 2 GHz for the Class 3 breast phantom using: (a) DBIM-SP reconstruction without errors in prior, (b) DBIM-SP reconstruction with 4 mm error in prior to the left, and (c) DBIM-SP reconstruction with 4 mm error in prior to the right. All reconstructions were obtained for 30 dB SNR and $\lambda = 5\lambda^*$. (Axes in cm.)

Table 3.6 and Figure 3.15 show the corresponding results for the Class 2 phantom. Again, the results reveal that DBIM-SP is robust in the presence of small errors in the prior information.

Figure 3.16 shows images of the Class 3 phantom using DBIM-SP with $\lambda = 5\lambda^*$ for our second investigation involving a mismatch in size. Here we consider the specific case when

TABLE 3.5: Mean absolute error (MAE) for the reconstruction of the Class 3 phantom using DBIM-SP ($\lambda = 5\lambda^*$) with erroneous shifts in the prior regions and different levels of SNR. The $-$ sign represents a shift of the fibroglandular region to the left and the $+$ sign represents a shift to the right.

Relative permittivity at 2 GHz						
	Adipose		Fibroglandular		Combined	
Shift	30 dB	10 dB	30 dB	10 dB	30 dB	10 dB
-8 mm	6.09	6.25	17.84	20.46	9.05	9.83
-6 mm	5.69	6.11	15.42	16.49	8.15	8.73
-4 mm	4.59	3.94	10.87	11.08	6.17	5.74
-2 mm	2.89	2.77	5.82	6.86	3.63	3.80
0 mm	**2.28**	**2.33**	**5.68**	**6.01**	**3.17**	**3.26**
+2 mm	4.41	4.44	10.26	10.81	5.88	6.05
+4 mm	6.46	5.86	14.95	14.97	8.60	8.16
+6 mm	7.42	8.08	17.80	18.40	10.03	10.69
+8 mm	7.85	8.75	20.44	21.19	11.03	11.89
Effective conductivity at 2 GHz						
	Adipose		Fibroglandular		Combined	
Shift	30 dB	10 dB	30 dB	10 dB	30 dB	10 dB
-8 mm	0.242	0.258	0.434	0.484	0.290	0.315
-6 mm	0.214	0.204	0.393	0.414	0.259	0.257
-4 mm	0.143	0.122	0.282	0.282	0.178	0.163
-2 mm	0.073	0.064	0.167	0.246	0.096	0.110
0 mm	**0.069**	**0.052**	**0.179**	**0.225**	**0.097**	**0.096**
+2 mm	0.134	0.113	0.301	0.460	0.176	0.200
+4 mm	0.200	0.174	0.432	0.502	0.259	0.257
+6 mm	0.241	0.201	0.510	0.648	0.309	0.314
+8 mm	0.276	0.230	0.558	0.688	0.347	0.346

the spatial prior for the fibroglandular region is 10% smaller (first row), and 23% smaller (second row). The smaller regions were obtained by shrinking the fibroglandular region of the original spatial prior of Figure 3.2 by 0.5 mm on every edge only in the axial dimension (first row) and in all dimensions (second row). We observe similar effects for these two cases. Namely, DBIM-SP increases the properties of the tissues on the edges between the fibroglandular and adipose regions to account for the mismatch.

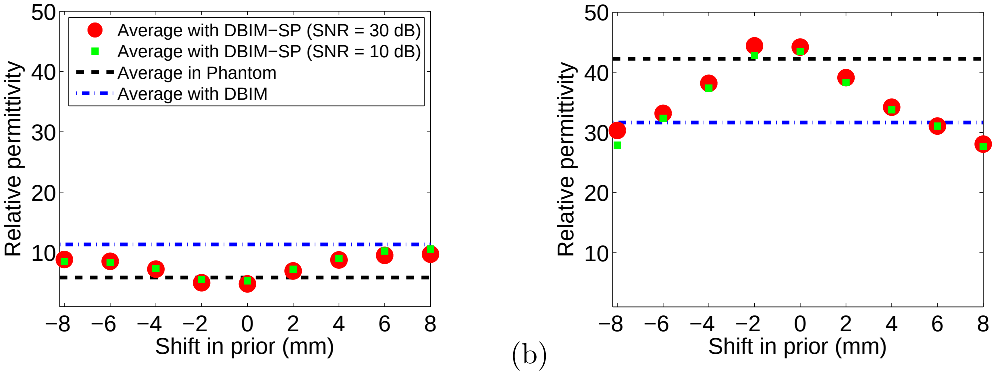

(a) (b)

Figure 3.14: Average relative permittivity at 2 GHz of (a) adipose tissue and (b) fibroglandular tissue using DBIM-SP with different levels of erroneous shifts in the prior regions for the imaging of the Class 3 phantom. Red circular markers correspond to reconstructions with 30 dB SNR and green square markers correspond to reconstructions with 10 dB SNR. The black dashed line corresponds to the phantom average and the blue point-dashed line corresponds to the average using conventional DBIM with 30 dB SNR.

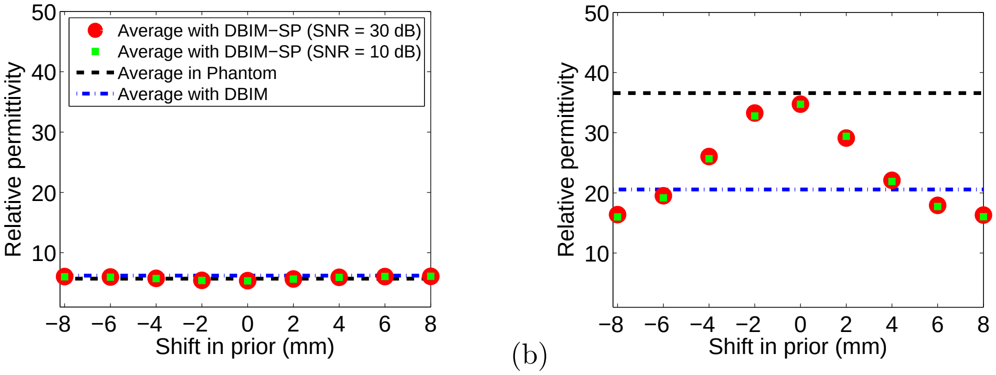

(a) (b)

Figure 3.15: Average relative permittivity at 2 GHz of (a) adipose tissue and (b) fibroglandular tissue using DBIM-SP with different levels of erroneous shifts in the prior regions for the imaging of the Class 2 phantom. Red circular markers correspond to reconstructions with 30 dB SNR and green square markers correspond to reconstructions with 10 dB SNR. The black dashed line corresponds to the phantom average and the blue point-dashed line corresponds to the average using conventional DBIM with 30 dB SNR.

TABLE 3.6: Mean absolute error (MAE) for the reconstruction of the Class 2 phantom using DBIM-SP ($\lambda = 5\lambda^*$) with erroneous shifts in the prior regions and different levels of SNR. The $-$ sign represents a shift of the fibroglandular region to the left and the $+$ sign represents a shift to the right.

Relative permittivity at 2 GHz						
	Adipose		Fibroglandular		Combined	
Shift	30 dB	10 dB	30 dB	10 dB	30 dB	10 dB
-8 mm	1.52	1.82	23.51	23.85	1.80	2.10
-6 mm	1.44	1.76	20.58	20.89	1.68	2.00
-4 mm	1.16	1.55	14.59	14.87	1.33	1.72
-2 mm	0.78	1.24	8.05	8.37	0.88	1.33
0 mm	**0.69**	**1.18**	**6.77**	**6.79**	**0.77**	**1.25**
+2 mm	1.00	1.46	12.02	11.88	1.14	1.60
+4 mm	1.36	1.76	18.47	18.60	1.57	1.97
+6 mm	1.56	1.92	22.14	22.37	1.82	2.18
+8 mm	1.61	1.95	23.57	23.89	1.89	2.23
Effective conductivity at 2 GHz						
	Adipose		Fibroglandular		Combined	
Shift	30 dB	10 dB	30 dB	10 dB	30 dB	10 dB
-8 mm	0.051	0.057	0.666	0.685	0.059	0.065
-6 mm	0.048	0.053	0.592	0.613	0.055	0.061
-4 mm	0.040	0.047	0.444	0.464	0.045	0.053
-2 mm	0.031	0.040	0.316	0.317	0.035	0.043
0 mm	**0.029**	**0.038**	**0.294**	**0.300**	**0.032**	**0.041**
+2 mm	0.036	0.044	0.443	0.434	0.041	0.049
+4 mm	0.043	0.051	0.586	0.595	0.050	0.058
+6 mm	0.049	0.056	0.671	0.686	0.057	0.064
+8 mm	0.050	0.058	0.697	0.716	0.058	0.067

3.6 Discussion and Conclusions

Our proposed DBIM-SP approach uses extremely sparse matrices with elements either 1 or -1. This high degree of sparsity enables efficient implementation—both in terms of memory and computation requirements—of a full 3-D reconstruction algorithm where the number of voxels is on the order of thousands. In our approach, the matrix $\mathbf{M}_0$, which stores all the spatial prior information, i.e. all the coefficients to form the spatial prior constraints, is of dimensions 41,576 × 41,578 for the locally homogeneous and Class 3

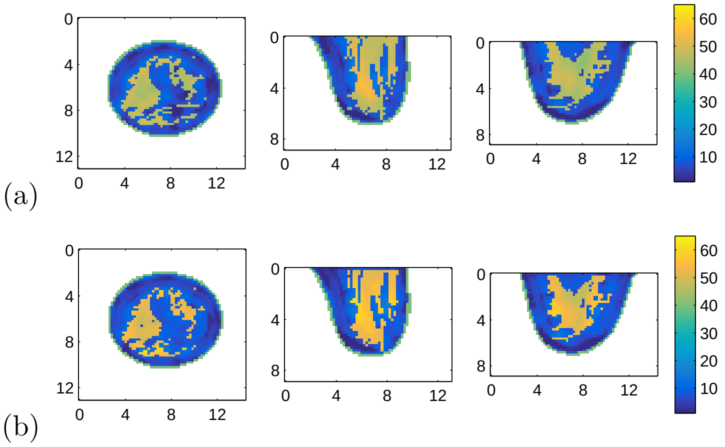

Figure 3.16: Coronal (left column), sagittal (middle column), and axial (right column) cross-sections of the relative permittivity at 2 GHz for the Class 3 breast phantom using (a) DBIM-SP with a fibroglandular spatial prior that is 10% smaller in volume than the true size, (b) DBIM-SP with a fibroglandular spatial prior that is 23% smaller in volume than the true size. All reconstructions were obtained for 30 dB SNR and $\lambda = 5\lambda^*$. (Axes in cm.)

phantoms and of dimensions 65,001 × 65,003 for the Class 2 phantom. Its density (i.e. the percentage of non-zero elements) is 0.0048% and 0.0031%, respectively. Therefore, the corresponding memory requirements for storing $\mathbf{M}_0$ in each case are only 1.6 MB and 2.6 MB. The computational time for performing reconstructions with DBIM-SP is only 2% higher than the computational time of conventional DBIM once the parameter λ^* is selected. This small increase is due to the additional sparse computations needed to invert the system with spatial prior constraints. Finding λ^* consumes additional time, but only needs to be done once per breast scan. The computational time of this process depends on how many λs are evaluated in the L-curve method described in section III.E. Using a warm start between λs significantly reduces this computational time.

We showed that DBIM-SP performs substantially better than the conventional DBIM at estimating the properties of the tissues in all phantoms. In fact, it achieves nearly perfect property estimation when the assumptions of the algorithm are satisfied to a great extent, as is the case when the phantom consists of locally homogeneous tissues. DBIM-SP also performs substantially better than regularization methods that do not use spatial prior information to promote boundary preservation and smoothness within regions. For example, the level set method presented in [14] which promotes smoothness within two regions achieves a MAE of 5.48 for the relative permittivity and 0.168 for the effective conductivity at 2 GHz for the Class 3 breast phantom with a 30 dB SNR. DBIM-SP improves these results by 42% when using $\lambda = 5\lambda^*$; that is, DBIM-SP ($\lambda = 5\lambda^*$) achieves a MAE of 3.17 and 0.097, respectively. Additionally, our results suggest that DBIM-SP is robust to noise and to errors in the model assumptions. The accuracy of estimating the average properties with DBIM-SP is high in all phantoms even in the presence of high levels of noise and even when there are relatively large offsets in the spatial prior information.

We demonstrated that different levels of variation of the estimated properties inside each region can be achieved by controlling the constraint parameter λ. In other spatial prior algorithms that implement soft constraints [64, 52, 51, 50], the parameter that sets the weight of the spatial prior constraints is linked to the L_2 regularization of the problem, and therefore it is difficult to obtain variations inside each region without the solution diverging. In our approach, the L_2 regularization is performed independently by using an L-curve method that controls the number of CGLS iterations. This allows solutions to have some heterogeneity within each region while keeping the solution bounded.

The appropriate value of λ will depend on the particular result that is being pursued. If it is of interest to estimate the average value of the dielectric properties of a region, a large λ should be chosen. If some heterogeneity within each region is of interest while preserving the boundaries within each tissue type, a small λ should be chosen. The value of λ^* serves as a lower bound for λ. As demonstrated in section III.E, values of λ smaller than λ^* put negligible weight on the spatial prior constraints.

Allowing variations inside each region is particularly important for robustness with respect to errors in the prior. We demonstrated that the algorithm compensates for errors in the location of the spatial prior regions by raising/lowering the properties in the parts of the regions that are mismatched with the actual phantom. Similar effects were observed when the fibroglandular spatial prior region was smaller than the actual fibroglandular tissue region.

This self-correcting feature of DBIM-SP suggests that this approach would be robust with respect to other types of errors in the prior information. For example, if we set a false inclusion as a third region immersed in the adipose tissue, DBIM-SP has the flexibility to reconstruct its properties as those corresponding to adipose tissue. If we create a false inclusion in the adipose tissue that is linked to the fibroglandular region, so that we still only have two regions, the algorithm again has the flexibility to lower the estimated properties of the false inclusion compared to the fibroglandular tissue in that region. Similarly, DBIM-SP would allow the estimated dielectric properties of a tumor to differ from those of the surrounding healthy fibroglandular tissue regardless of whether there was a specific, distinct spatial prior for the tumor.

An important requirement of DBIM-SP is accurate co-registration between the imaging modality that provides the spatial prior information and the microwave imaging scan. As discussed in section IV.D, misalignments of more than 6 mm may result in poorer image quality than conventional DBIM. However, co-registration is an active area of investigation, and the system presented in [52] has shown to produce good alignment results.

4 A CLINICAL STUDY OF THE IMPACT OF MICROWAVE ABLATION ON THE DIELECTRIC PROPERTIES OF BREAST TISSUE

This chapter is intended for submission to *Physics in Medicine and Biology.*

4.1 Abstract

Percutaneous microwave ablation (MWA) is a promising technology for patients with breast cancer, as it has potential to treat individuals who have less aggressive cancers or do not respond to targeted therapies in the neoadjuvant or pre-surgical setting. In this study we investigate the changes induced by MWA in the microwave dielectric properties of breast tissue. While these changes have been characterized for relatively homogeneous tissues such as liver, those prior results are not directly translatable to breast tissue because of the extreme tissue heterogeneity present in the breast. This study was motivated in part by the expectation that the changes in the dielectric properties will be impacted by breast composition of the targeted volume, and this knowledge is essential for the successful development of MWA systems for breast cancer. We performed ablations in 14 human ex-vivo prophylactic mastectomy specimens from surgeries conducted at the UW Hospital and monitored the temperature in the vicinity of the MWA antenna during ablation. After ablation we measured the dielectric properties of the tissue and analyzed the tissue samples to determine both the tissue composition and the extent of damage due to the ablation. We observed that MWA induced cell damage across all tissue compositions, and found that the microwave frequency-dependent relative permittivity and conductivity of damaged tissue are lower than those of healthy tissue, especially for tissue with high fibroglandular content. The results provide information for future developments on breast MWA systems.

4.2 Introduction

The majority of new breast cancer cases are diagnosed at an early and localized stage wherein the tumor is no more than 2 cm in size [73]. There is growing interest in applying minimally invasive ablative therapies to patients with these small breast carcinomas to minimize the side effects and risks of surgical treatment, particularly in individuals who have less aggressive cancers and in those for whom surgery is prohibitive due to comorbidities [74, 75, 76]. Additionally, there is a significant number of patients who do not respond to targeted therapies in the neoadjuvant or presurgical setting. The response of a primary breast tumor to either neoadjuvant chemo or endocrine therapy ranges between 5 and 50% [77], and these patients have a worse prognostic outcome [78]. Ablative therapies are a promising option for treating these tumors before surgery.

Percutaneous microwave ablation (MWA) is a minimally invasive thermal therapy that delivers microwave energy to the tumor via an interstitial antenna [26]. The microwave energy absorbed in the tumor induces the cytotoxic effects of heat, resulting in protein denaturation and coagulation necrosis [56]. MWA has already emerged as a well-accepted technique for treating unresectable malignant hepatic tumors [79, 22], in part because of its advantages relative to other thermal therapies. Namely, MWA achieves higher temperatures, larger ablation volumes (as needed), and shorter ablation times [53], thereby avoiding the discomfort patients experience with prolonged heating.

MWA is under investigation for treating other types of cancer, including malignant breast tumors [19, 20, 80]. Zhou *et al.* found that the rate of complete ablation of small breast tumors was higher than that of radio-frequency ablation, high-intensity focused ultrasound, laser ablation, and cryoablation [20]. Additionally, Yu *et al.* have shown a reduction in volume and palpability of the lesions and satisfying cosmetic outcomes [80]. These preliminary *in vivo* studies suggest that MWA is a promising alternative to surgery for minimally invasive treatment of breast cancer.

Knowledge about microwave-frequency dielectric properties changes throughout the breast tissue during MWA is essential for the successful development of MWA systems for breast cancer. Lazebnik *et al.* [11] and [10] characterized the dielectric properties of ex vivo breast tissue at room temperature. However, the temperature increase during MWA and the accompanying physiological changes in the tissue induce changes in the microwave dielectric properties as the ablation progresses. The dielectric properties of other tissues have been characterized over wide temperature ranges (e.g., [57] and references therein), motivated by the interest in improving simulation tools for designing hepatic ablation systems. However, breast tissue is very different than liver tissue in that it is composed of fibrous, glandular, and adipose tissue types, and this is highly heterogeneous. The heterogeneity present in breast tissue impacts changes in dielectric properties throughout the ablation zone depending on the breast composition of the target volume.

In this study we investigate MWA in heterogeneous breast tissue and characterize the changes in temperature during ablation and the resulting change in tissue microwave dielectric properties post-ablation. We performed ablations in 14 human ex-vivo prophylactic mastectomy specimens from surgeries conducted at the University of Wisconsin Hospital and Clinics. The ablations were performed at 1.9 GHz using between 35-100 W of power for 2 to 5 minutes. The temperature was monitored during ablation in the vicinity of the antenna, and dielectric properties were measured post-ablation after dissecting the ablated zone. We evaluated samples of the tissue to determine both the tissue composition and the extent of damage due to the ablation. All this information allows us to draw conclusions on the dynamics and effects of microwave ablation of heterogeneous breast tissue. The results provide information for future developments on breast MWA systems.

The paper is organized as follows. Section 2 presents the experimental procedures performed in this study, including the handling of the mastectomy specimens, as well as the MWA details and measurement details. Section 3 presents the results of this study, namely temperature, histology analysis, and dielectric spectroscopy measurements taken during the experiments. Section 4 discusses the results and the implications of our findings. Section 5 presents a summary and conclusion of the investigation.

4.3 Experimental Procedure

Source of tissue and tissue handling procedure

Microwave ablation was performed in 14 whole-breast mastectomy specimens obtained from prophylactic mastectomy surgeries at the University of Wisconsin Hospital and Clinics. By using prophylactic mastectomy specimens, we focus on the effects and performance of MWA in healthy (non-cancerous) tissue. The subjects who underwent the mastectomy surgeries were between 37 and 56 years old, with a mean age of 43 years old. Ten of the subjects had contralateral breast cancer at the time of surgery, and three of them had received neoadjuvant chemotherapy treatment in the six months previous to the surgery. In pre-operative radiology examination, twelve subjects were classified as BI-RADS density class 3 “heterogeneously dense”, one was classified as BI-RADS density class 2 “scattered fibroglandular elements”, and one was classified as BI-RADS density class 1 “predominantly fatty”.

As soon as the surgeon removed the breast from the subject, it was transported from the operating room to the hospital pathology grossing area where the pathologists’ assistant weighed the specimen and inked its exterior, as per standard protocol. The weights of the specimens ranged between 400 g to 1720 g. Immediately following this initial examination, MWA was performed and the measurements were taken. The microwave ablations began 20 to 35 minutes after the specimens left the operating room.

During the MWA procedure temperature measurements were taken at four locations. Immediately after the power was turned off dielectric measurements and histological samples were obtained from the specimen from the same four locations. Finally, the tissue was handed back to the pathologist's assistant to gross the sample as per standard protocol. The complete experiment, including the microwave ablation procedure and the measurements, had to be done under strict time constraints to ensure that the tissue was placed in a preservative within one hour of being removed from the subjects, to comply with the tissue handling guidelines set by the American Society of Clinical Oncology and the College of American Pathologists.

MWA details

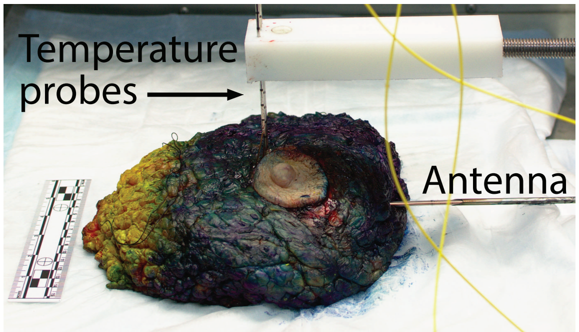

Figure 4.1: Photograph of the microwave ablation and temperature monitoring configuration. The rigid ablation antenna is inserted horizontally into the mastectomy specimen while four fiber-optic temperature probes are inserted vertically into the tissue through biopsy needles. The yellow and dark blue color of the specimen is due to ink applied to the specimen surface as part of the standard pathology grossing procedure.

Figure 4.1 shows the experimental set-up for MWA at the grossing room's lab bench. The blue and yellow color of the specimen is due to the ink applied by the pathologist's assistant. With the posterior of the breast lying down on the lab bench, the MWA antenna was inserted horizontally into the specimen. Given the highly heterogeneous composition of the breast (adipose tissue with regions of fibrous and glandular tissue), inserting the antenna by itself was difficult and would have bent the antenna. Therefore, to aid the insertion, we used a hand-made 4 mm diameter stainless-steel needle guide that was then retracted to the outside of the tissue. The antenna insertion was aimed in such a way that the active portion of the antenna would be underneath the nipple to target tissue with fibroglandular content.

Two different antennas were used in this study. For the first two experiments we used a balun-free helical monopole antenna, as described in [59], which was modified to operate at 1.9 GHz in breast tissue that has a 30% fibroglandular composition. This antenna offers benefits such as a small diameter and compact heating zone; however, it is quite sensitive to the dielectric environment of the surrounding tissue. For specimens 3-14 we used a floating sleeve dipole (FSD) antenna [81] modified to operate at 1.9 GHz in breast tissue that has 30% fibroglandular composition. The FSD design produces larger heating zones and has a larger diameter than the helical monopole, making it more invasive. However, it is less sensitive to the tissue environment than the helical monopole design and is physically more robust. Due to the ex-vivo nature of this study, the sensitivity and physical strength benefits of the FSD design outweighed its increased invasiveness and larger heating zone, and this design was used for the majority of the experiments. The modifications made to these antennas can be found in [82].

The ablations were performed using a continuous 1.9 GHz signal. The power levels and ablation times are shown in table 4.1. The power and times varied between 35 and 100 W and 2 to 5 minutes. For the first two experiments, we used lower power levels as we were still determining the necessary power levels to achieve high temperatures in less than 5 minutes. Starting with specimen 3, we adopted using always 100 W and modifying the ablation time between 2 and 5 minutes, to ensure that the specimen reached temperatures above 60 °C for significant amounts of time.

The equipment used for microwave ablation consisted of a 1.9 GHz signal generator, namely an HP 8350B sweep oscillator with the 83522A plug-in to cover 1.9 GHz. The signal was amplified to the desired power level with a DMS 7066 amplifier. The high power signal was passed through a three-port circulator to the ablation antenna. The circulator directed any reflected power from the antenna through a 40 dB attenuator to a Gigatronics 8542 universal power meter. The power meter arrangement facilitated monitoring the reflected power and therefore the power that was actually being delivered into the tissue.

An Agilent N5221A vector network analyzer (VNA) was used to record the input reflection coefficient (S11) for the antenna inside the tissue, prior to the ablation. The antenna

TABLE 4.1: Power level, duration, and antenna type used for each ablation experiment.

Specimen	Power (W)	Time (minutes)	Antenna
1	35	5	Helical monopole
2	40	5	Helical monopole
3	100	2	FSD
4	100	2	FSD
5	100	5	FSD
6	100	4.5	FSD
7	100	4.5	FSD
8	100	4	FSD
9	100	4	FSD
10	100	5	FSD
11	100	5	FSD
12	100	5	FSD
13	100	4.5	FSD
14	100	5	FSD

was then disconnected from the VNA and attached to the output of the power amplifier.

Measurements

We obtained temperature measurements, dielectric spectroscopy measurements, and samples for histological analysis from four locations with respect to the antenna in a radial horizontal direction. The locations were: 5 mm to the left, 5 mm to the right, 10 mm to the right, and 15 mm to the right of the center of the active portion of the antenna. A schematic of the measurement configuration is shown in Figure 4.2. The schematic shows the cross-section transverse to the center of the active portion of the antenna.

Temperature

Four fiber optic temperature probes were inserted vertically into the tissue using 14 gauge biopsy needles passing through a plastic template to ensure correct probe spacing. The temperature probes are shown as vertical lines in Figure 4.2. All the needles were retracted from the tissue prior to the start of the ablation, leaving only the non-conductive temperature probes and the antenna present in the tissue. Temperature measurements at the four locations were recorded every 1 second while the power for the ablation was turned on.

Three temperature measurements were excluded from our results due to the temperature probes coming out of the tissue or getting damaged during the experiment.

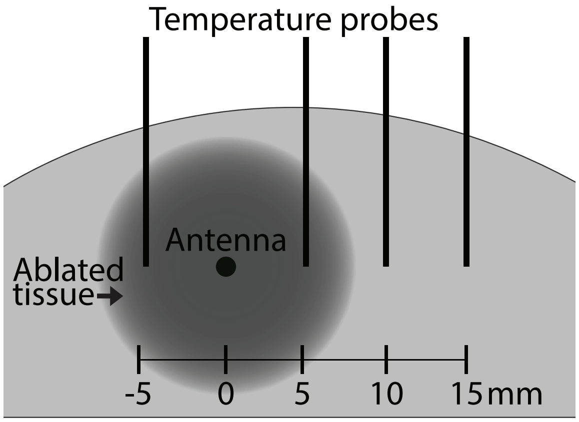

Figure 4.2: Schematic showing measurement locations relative to the MWA antenna. In this cross-sectional view, the ablation antenna is oriented perpendicular to the plane of the page. The temperature probes are shown as vertical black lines. The tips of the temperature probes are positioned along a horizontal line perpendicular to the longitudinal axis of the antenna and spaced in 5-mm increments away from the antenna. Dielectric spectroscopy measurements and samples for histological analysis were taken from these same temperature measurement locations. The dark region represents an example of ablated tissue.

Dielectric spectroscopy measurements

After power for the ablation was turned off, the tissue was cut along the plane of the temperature probes and transverse to the antenna (along the plane shown in the schematic in Figure 4.2). A second cut was made, parallel to the first, to facilitate placing the slice of tissue flat on the lab bench. Dielectric spectroscopy measurements of the tissue in the same locations in which the temperature probes were placed were taken immediately after the tissue was sliced.

The dielectric spectroscopy measurements were performed over the frequency range of 0.5 to 10 GHz using the Agilent Technologies 85070E Dielectric Probe Kit. The slim-form probe used for these measurements has a diameter of 2.2 mm and an approximate sensing volume extending 1.5 mm into the tissue from the surface, with a width of 5 mm [83]. The dielectric probe was calibrated while the ablation was being performed, therefore the time between probe calibration and the dielectric measurements was always under 5 minutes. Two dielectric probe measurements were recorded in each of the measurement locations. After the dielectric probe measurements were complete, the tissue was lightly dried with a

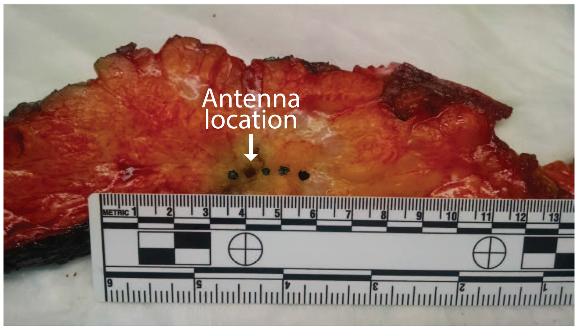

Figure 4.3: Photograph of a sliced tissue specimen post ablation. The orientation here is the same as the plane of Fig. 4.2. Black ink spots mark the locations of the four dielectric measurements. The second dark circle from the left is the hole where the MWA antenna was inserted.

paper towel, and the measurement locations were inked with green ink using a toothpick. These ink spots facilitated subsequent histological evaluation of the tissue composition at the measurement locations. Figure 4.3 shows the slice of tissue after inking. The four ink spots are visible as well as the hole from the antenna insertion (second from the left).

The data sets were fitted to Debye models. Given the small frequency range in which the samples were characterized, the Debye models provided good fits that were comparable to those of more flexible models such as Cole-Cole, while having less ambiguity in the model parameters. To identify dielectric measurements that mischaracterized the tissue samples due to experimental errors, such as poor contact between the probe and the tissue, we conduct a Kramers-Kronig consistency test similar to the test performed in [11]. Here we evaluate the quality of the physical model fit to determine if the data satisfies the Kramers-Kronig relation. The quality of the fit was determined by its root mean squared error:

$$e = \sqrt{\sum_{i=1}^{N} \|\boldsymbol{\epsilon}^*_{\text{meas},i} - \boldsymbol{\epsilon}^*_{\text{fit},i}\|^2 / N} \tag{4.1}$$

where $\boldsymbol{\epsilon}^*_{\text{meas},i}$ is the complex permittivity measured at frequency point i and $\boldsymbol{\epsilon}^*_{\text{fit},i}$is the corresponding complex permittivity of the Debye fit. The number of frequency points recorded N was 951. We set the threshold at $e = 0.001$. Any measurements that produced fits with $e > 0.001$ were excluded from our results and analysis. This value was chosen to exclude the cases in which the best fitting Debye model did not match the frequency dependence of the measured data set. A total of 10 characterized tissue samples were excluded based on this criterion.

Another 8 measurements were excluded due to the location of the measurements not corresponding to the standard locations shown in the schematic in figure 4.2. The exclusions left 94 dielectric spectroscopy measurements for final analysis.

Histological analysis

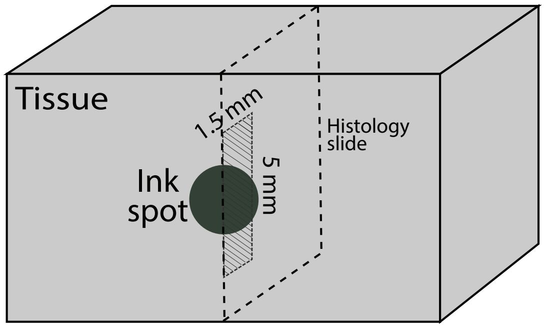

Figure 4.4: Illustration showing the orientation of the histology section taken at the location of a black ink spot. The 1.5-mm by 5.0-mm region beneath the ink spot marks the area assessed during histological analysis of the section.

After the dielectric spectroscopy measurements were completed and the location of the measurements was inked, a small piece of tissue at each of the measurement locations was removed and sent for histological analysis. The analysis consisted in evaluating the tissue composition (proportion of adipose and fibroglandular tissue) and the damage observed in the sample (proportion of fibroglandular cells that showed evidence of thermal damage). Thermal damage was described by cautery-like effects and nuclear disruptions in epithelial cells, and it could only be noticed in fibroglandular cells (not adipose cells). The volume analyzed by the pathologist consisted of an area extending 1.5 mm into the tissue from the surface, with a width of 5 mm. This region was chosen to correspond to the sensing volume of the 2.2 mm diameter open-ended coaxial probe used for the dielectric measurements. Figure 4.4 shows a schematic of the histology slide obtained from an the probe measurement location (ink spot) and the region that was analyzed with respect to it.

Of the 56 histology slides taken, four were excluded from our results and analysis since they did not correspond to the standard locations shown in the schematic in figure 4.2.

4.4 Results

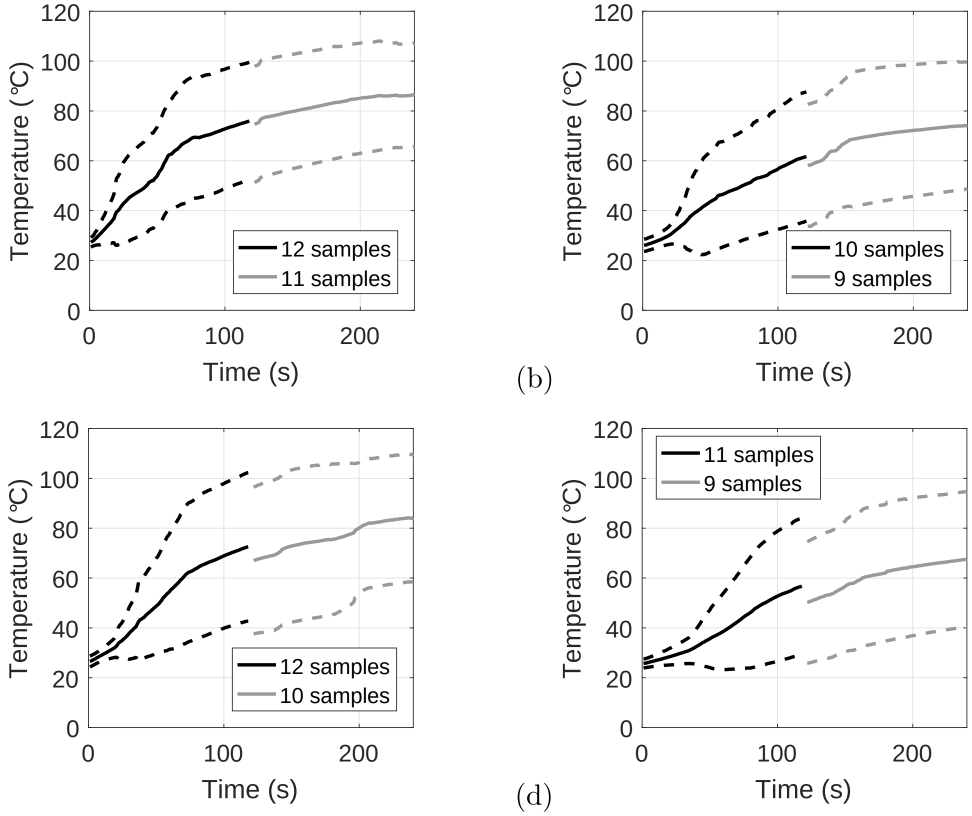

(a) (b) (c) (d)

Figure 4.5: Mean (solid) and standard deviation range (dotted) of temperatures observed at the following locations as a function of time for the first 4 minutes of MWA: (a) 5 mm to the left of the antenna, (b) 5 mm to the right of the antenna, (c) 10 mm to the right of the antenna, and (d) 15 mm to the right of the antenna. The discontinuities are due to the availability of measurement data sets for a larger number of tissue specimens during the first 2 minutes of ablation. Only measurements for ablations at 100 W were considered in this analysis.

Figure 4.5 shows the mean temperatures, as well as one standard deviation range, observed at each of the four locations, as a function of the time the power was on. In these plots, only the data for experiments that used 100 W of power was considered, to examine the evolution of temperature for a constant power level. The number of samples available in each location varies because of the data that was excluded from our results. The jumps are due to the varying duration of the experiments. We observe that within the 10 mm next to the center of the active portion of the microwave ablation antenna, the temperature increase behaves quite similarly (plots (a), (b), and (c)). In these locations, the temperature observations reached averages above 60°C within the first two minutes of ablation. In the location 15 mm away from the antenna the temperature increase was slower, achieving average temperatures above 60°C after two and a half minutes. The sudden increase in temperature we observe in the 75$^{\text{th}}$ percentile curve in plot (b) and 25$^{\text{th}}$ percentile in plot (c) was something observed a number of times during the experiments. This sudden increase could be due to steam reaching the temperature probe or a slight movement of the temperature probe due to tissue deformation.

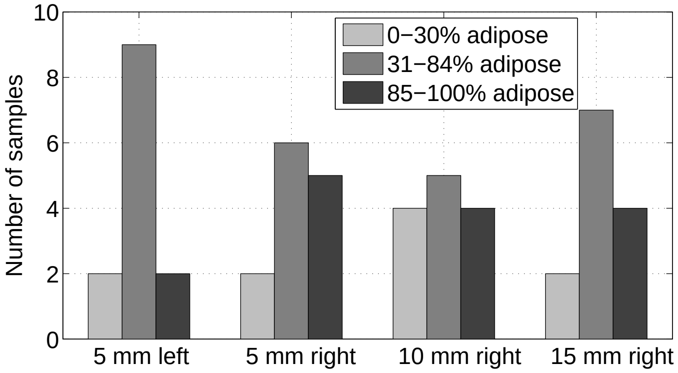

Figure 4.6: Histogram showing tissue composition of each sample, as determined via histological analysis. The bars show the number of cases at each measurement location (5 mm to the left and 5/10/15 mm to the right) in each of the following composition groups: 0-30% adipose, 31-84% adipose, and 85-100% adipose. Twelve of the 15 samples in the 85-100% adipose group were 100% adipose.

Figure 4.6 shows the histology results for the composition of the samples in the four locations. In this histogram, we group the data into three groups according to the proportion of adipose tissue present in the sample in the region of interest. The groups are 0-30% adipose content, 31-84% adipose content, and 85-100% adipose content. This grouping criterion follows that of [11]. We observe that the samples in the four locations span the whole range of possible tissue compositions for breast tissue. Of the 15 samples in the 85-100% adipose tissue, 12 of them were 100% adipose tissue. These samples did not give us any further information about the damage of the tissue because the histology analysis did not allow to appreciate damage in adipose cells.

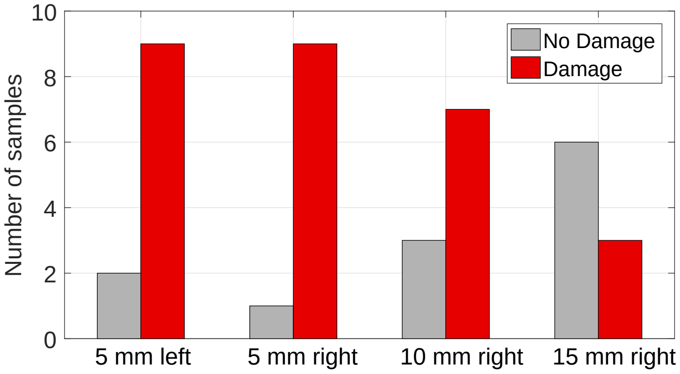

Figure 4.7: Histogram showing the histological outcomes for thermal damage assessment. The bars show the number of cases at each measurement location exhibiting “damage” versus “no damage”. The 12 samples of 100% adipose tissue are not reported here since their damage state cannot be assessed via histological analysis.

The histology results for observed damage of the samples that contained at least some non-adipose cells are summarized in figure 4.7. Here we consider that a sample was damaged if 30% or more of the non-adipose cells showed nuclear disruptions and observable cautery-like effects. We chose 30% because this was the smallest proportion of damaged cells observed in the samples that showed damage, i.e. the samples in the “no damage” group, in fact, did not show any signs of damage. The figure shows that, as expected, damage is more predominant in the locations closer to the antenna and the proportion of samples where damage was observed decreases as we move further away from the antenna.

Figure 4.8 plots the histology results for composition and damage, together with the peak temperatures observed for each sample. Here red circles indicate samples that show damage, and blue triangles indicate non-damaged samples. Firstly, we note that there are samples across all tissue compositions that show damage. This indicates that the presence of adipose tissue does not impede ablation of other types of tissues. Additionally, we observe that 78% of the samples that reached temperatures above 60°C showed evidence of damage, while none of the samples that reached less than 40°C showed signs of damage.

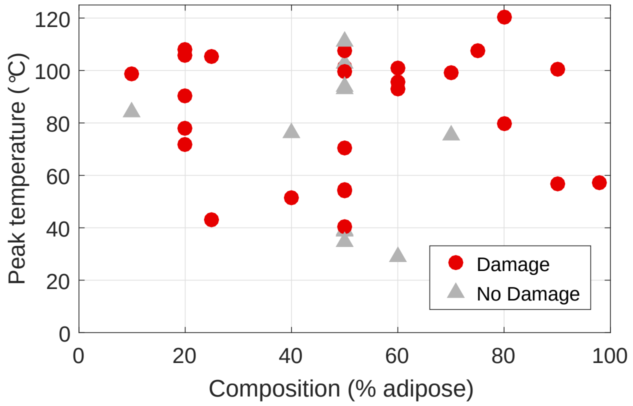

Figure 4.8: Peak temperature observed at each measurement location versus adipose content of the tissue at that location. The marker style indicates whether damage was or was not observed during the histological analysis.

Some samples seem to have reached very high temperatures, and however not present damage. This seemingly inconsistency might be due to the temperature being high for only a short amount of time or to poor co-location between the temperature measurements and the samples taken for histological analysis, meaning that the location of the temperature measurement might have been slightly different than the site from where we took the histology slide.

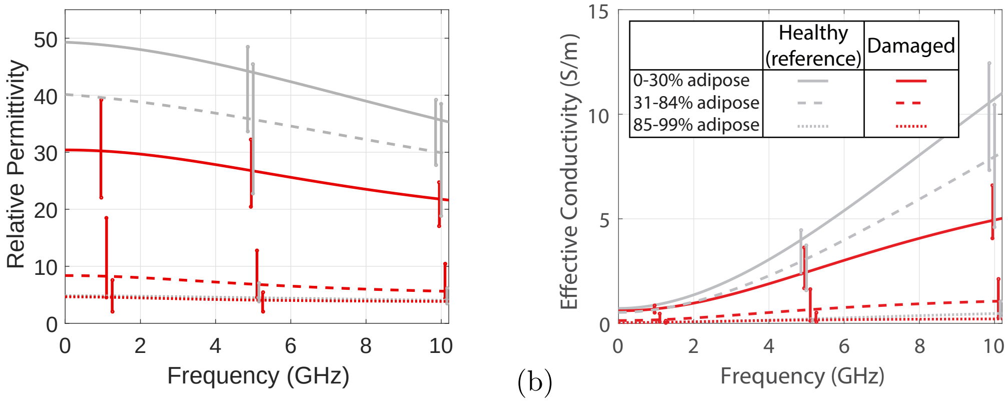

(a) (b)

Figure 4.9: Median fitted dielectric properties of ablated breast tissue (red lines, this study) compared to healthy breast tissue (gray lines, [11]). The variability bars show the 25th and 75th percentiles.

Finally, figure 4.9 shows the median relative permittivity and effective conductivity of the samples that showed damaged, for each of the three composition groups. These curves were calculated using the median values of the Debye fit parameters for the measurements in each composition group. For reference, the plots also show dielectric properties of healthy tissue for each composition group, as reported by [11]. The variability bars show the 25th and 75th percentiles of the properties of each group. We observe that the dielectric properties of damaged tissue are considerably lower than those of healthy tissue, especially for tissue with high fibroglandular content. This is consistent with what has been observed for other tissue types, such as liver [30], where the dielectric properties of ablated tissue are lower than those of healthy tissue.

4.5 Discussion

Performing these ablations in ex vivo human breast tissue was somewhat challenging, mainly because of the heterogeneity of the tissue. Insertion of the temperature probes through the fibrous tissue was difficult, and the angles of insertion could have been affected causing misalignment of the measurement locations. This could explain some of the inconsistencies in the data, such as samples reaching high temperatures but not showing signs of damage. Also, we observed considerable tissue deformation during the course of the ablation, where the tissue would swell up above the active region of the antenna. The deformation was likely a side-effect of tissue contraction due to dehydration during ablation. This distortion is potentially problematic as it introduces uncertainty in the locations of the temperature probes with respect to the antenna.

This issue of exact location of measurement sites also arises for the dielectric measurements and histological analysis. After dissecting the tissue, the hole where the antenna was inserted is evident, and therefore the four locations for the dielectric measurements can be determined confidently by using a ruler. However, after measuring, we ink the measurement spot, the pathologist's assistant takes the tissue samples, and the pathologist analyzes the samples in the specified area. Because these three steps are done at different moments in time and by different people, there is likely some mismatch between the areas being analyzed.

Another practical consideration is that due to the fibrous tissue in the breast being very tough and the adipose tissue being very brittle, a stainless-steel needle was needed to aid the antenna insertion procedure to guide the insertion in the desired direction and protect the integrity of the antenna. This indicates that in practice, a physically strong antenna will be necessary to perform ablations of tumors in breast tissue.

Of particular note is the fact that the presence of adipose tissue in a given region does not impede the ablation of the fibroglandular tissue in that region. The samples showing evidence of thermal damage span the full range of fibroglandular percentages. This is an important result for assessing the efficacy of MWA in breast tissue: because the breast is highly heterogeneous it is important that a proposed therapy is capable of destroying target cells which are surrounded by adipose tissue.

As expected, the relative permittivity and effective conductivity in the microwave frequency range of ablated breast tissue were lower than that of healthy breast tissue. This was observed for tissue samples across all composition groups. This result is important for antenna design considerations, as the antenna has to perform in tissue that will be changing dielectric properties during the course of the ablation. Also, this result is encouraging for MWA monitoring strategies that use radar or inverse scattering techniques. However, further investigations need to be done to increase the number of samples and provide a more statistically significant analysis.

4.6 Conclusion and Summary

This study demonstrates a protocol for acquiring dielectric and histological data in conjunction with MWA of ex-vivo human breast tissue. High temperatures, above 60 °C, and accompanying cell damage were achieved for tissue across the whole range of possible compositions (fibroglandular/adipose content). An important result is that the presence of adipose tissue in a given region does not impede the damage of fibroglandular tissue in that region. This is relevant because malignant cells are similar to fibroglandular cells. Finally, we found that the ablation generally decreased the permittivity and conductivity of tissue. These results provide a valuable reference point for the development of future microwave ablation of breast tumor treatments and accompanying ablation monitoring techniques.

5 CHARACTERIZATION AND ANALYSIS OF WIDEBAND TEMPERATURE-DEPENDENT DIELECTRIC PROPERTIES OF LIVER TISSUE FOR NEXT-GENERATION MINIMALLY INVASIVE MICROWAVE TUMOR ABLATION TECHNOLOGY

This chapter was previously published in *2018 IEEE/MTT-S International Microwave Symposium - IMS* [84].

5.1 Abstract

Microwave ablation (MWA) is a minimally invasive thermal therapy that delivers microwave energy to a malignant tumor via an interstitial antenna. To date, MWA systems have primarily operated at 915 MHz or 2.45 GHz. Knowledge of the temperature-dependent tissue dielectric properties at frequencies above 2.45 GHz is essential for future development of MWA systems that leverage advantageous antenna design and ablation performance characteristics at higher frequencies. This information is also critical for the development of real-time microwave sensing techniques for MWA monitoring. We report measured and modeled wideband (0.5-20 GHz) temperature-dependent (25-93°C) dielectric properties of ex vivo porcine liver tissue during MWA. The temperature-dependent dielectric properties were modeled using two-pole Debye models with temperature-dependent parameters described by third-order polynomials. The results address a gap in present knowledge of properties over both a wide frequency band and wide range of temperatures relevant to MWA.

5.2 Introduction

Percutaneous microwave ablation (MWA) is a minimally invasive thermal therapy for treating cancer. It consists of delivering a cytotoxic microwave-induced thermal dose to the tumor via an interstitial antenna [26]. Microwave-induced heating of tissue to temperatures above 50-60°C induces protein denaturation and coagulation necrosis [56]. MWA has already emerged as a well-accepted technique for treating unresectable malignant hepatic tumors [79, 22]. While clinical microwave ablation treatments have been performed using 915 MHz and 2.45 GHz systems [53], there are compelling advantages in using higher frequencies. A recent study of MWA at frequencies between 1.9 and 26 GHz—a range that includes three ISM bands—showed that the use of higher frequencies produces more spherical ablation zones [85]. Furthermore, operating at higher frequencies facilitates the design of shorter antennas that offer greater agility and flexibility in reaching the target tissue, compared to conventional low-frequency MWA antennas.

Knowledge of the dynamic behavior of tissue dielectric properties at higher microwave frequencies during MWA treatment is essential for the successful development of next-generation minimally invasive MWA systems. Such data is also critically important for the development of wideband or multiband microwave imaging techniques for real-time monitoring of MWA, regardless of the ablation frequency [86, 87]. Wideband dielectric properties (0.5 - 20 GHz) of bovine liver tissue over the temperature range between 20°C and 60°C have been previously reported [57] (and references therein). However, during MWA treatment the tissue temperature easily rises above 60°C, at which point the tissue undergoes significant irreversible changes in physiology. The dielectric properties of animal liver tissue over a much wider range of temperatures (20°C to 120°C) have only been reported at 2.45 GHz [31, 30, 88].

This paper addresses the gap in the present knowledge of tissue dielectric properties over a wide range of frequencies, and simultaneously, a wide range of temperatures relevant to MWA. In this study we measured and analyzed wideband temperature dependent dielectric properties of liver tissue during MWA. We performed four ex-vivo liver ablations and recorded in situ temperature and dielectric spectroscopy measurements during the ablations. We modeled the measured temperature-dependent dielectric properties using two-pole Debye models with temperature-dependent parameters. The results provide valuable information for the future development of MWA and ablation monitoring systems.

5.3 Methods

Experimental Procedure

We performed microwave ablations in four samples of ex-vivo porcine liver tissue specimens. In all cases, the livers were kept sealed in a thermally insulated container from the time of excision to experiment, and the experiments were concluded within 5 hours of excision. The ablations were performed at a power level of 40 W using a 1.9 GHz floating sleeve dipole antenna and system hardware similar to that reported in [89]. Ablation durations ranged between 1 and 17 minutes.

Figure 5.1 shows the experimental set-up. The MWA antenna was inserted horizontally into the tissue, and the temperature and dielectric probes were inserted vertically at a radial distance of approximately 1 cm from the active region of the antenna. The temperature measurements were performed with a Neoptix fiber-optic temperature sensor. The dielectric spectroscopy measurements were performed over the frequency range of 0.5 to 20 GHz using an Agilent 85070E dielectric probe kit with a slim-form probe. The 2.2-mm-diameter probe has an approximate sensing volume extending 1.5 mm into the tissue from the surface, with a width of 5 mm [83]. Two thin fiberoptic temperature probes were bundled with the dielectric probe, one at each side, to reduce uncertainty in the temperature of the tissue that was being characterized. The temperature of the tissue at the tip of the dielectric probe was assumed to be the average between the two temperature probes. The tips of the temperature probes were positioned approximately 1 mm above the tip of the dielectric probe to ensure that the dielectric measurements were not affected by the presence of the temperature probes[1]. Temperature and dielectric spectroscopy measurements were recorded every 20 seconds during each ablation. This resulted in a total of 127 measurements of wideband dielectric properties of liver tissue at different temperatures.

Data analysis

The following two-pole Debye model was fit to each dielectric spectroscopy data set by minimizing the squared error in the complex permittivity over frequency:

$$\epsilon'(\omega) - j\epsilon''(\omega) = \epsilon_\infty + \frac{\Delta\epsilon_1}{1 + j\omega\tau_1} + \frac{\Delta\epsilon_2}{1 + j\omega\tau_2} + \frac{\sigma_s}{j\omega\epsilon_0}. \tag{5.1}$$

A two-pole Debye model was chosen over a single pole model because it provided a better fit over the wide frequency band of the measurements. We evaluated the quality of each fit and excluded the measurement data set if the root-mean-square error exceeded a set threshold. This type of exclusion criteria has been previously used to ensure consistency with the Kramers-Kronig relation and eliminate measured data that may have been corrupted by experimental artifacts [57].

This process yielded six Debye parameters (ϵ_∞, σ_s, $\Delta\epsilon_1$, τ_1, $\Delta\epsilon_2$, and τ_2) as a function of temperature. We fit a third-order polynomial to each Debye-parameter-versus-temperature

---

[1] The validity of this configuration was confirmed using reference liquid measurements.

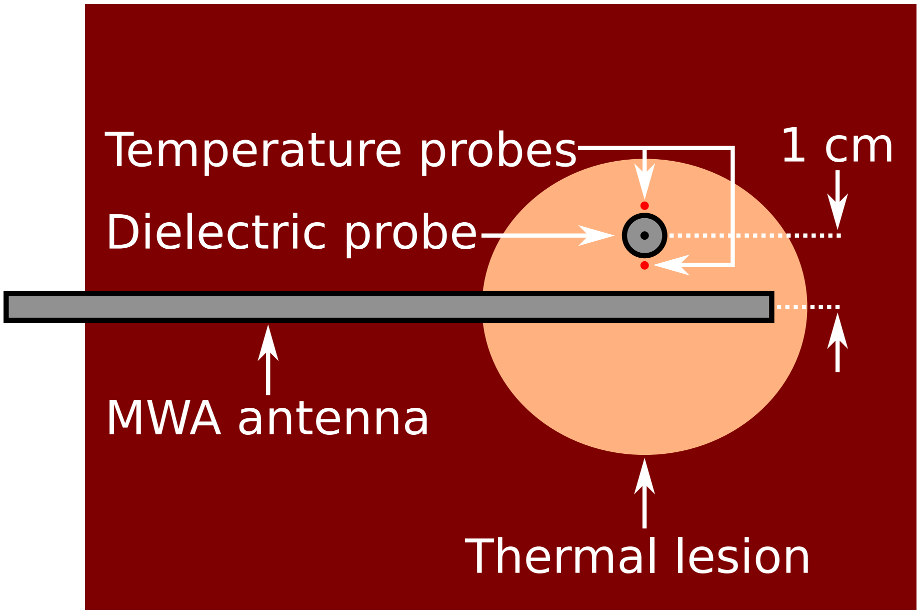

Figure 5.1: Top view of the experimental configuration for characterizing the temperature-dependent dielectric properties during ablation. The MWA antenna is oriented horizontally inside the tissue specimen while the dielectric probe and two temperature probes are oriented vertically at a radial distance of approximately 1 cm from the active central portion of the antenna.

curve. This allowed us to capture the wideband, temperature-dependent dielectric properties of liver tissue during ablation using a very compact model.

5.4 Results

The temperatures recorded during the MWA procedures ranged from 25°C to 93°C. Six of the 127 measurements were excluded because the root-mean-square error of the Debye fit exceeded the chosen threshold. Approximately 65% of the remaining 121 data sets corresponded to temperatures above 60°C, which are the temperatures of greatest interest in this study.

Figure 2 shows the parameters of the two-pole Debye fits for each measurement (individual black circles) as a function of temperature and their corresponding polynomial fit (solid red curves). All six parameters demonstrate temperature dependent effects during

MWA. Table I shows the coefficients of the third-order polynomial fits for each two-pole Debye parameter.

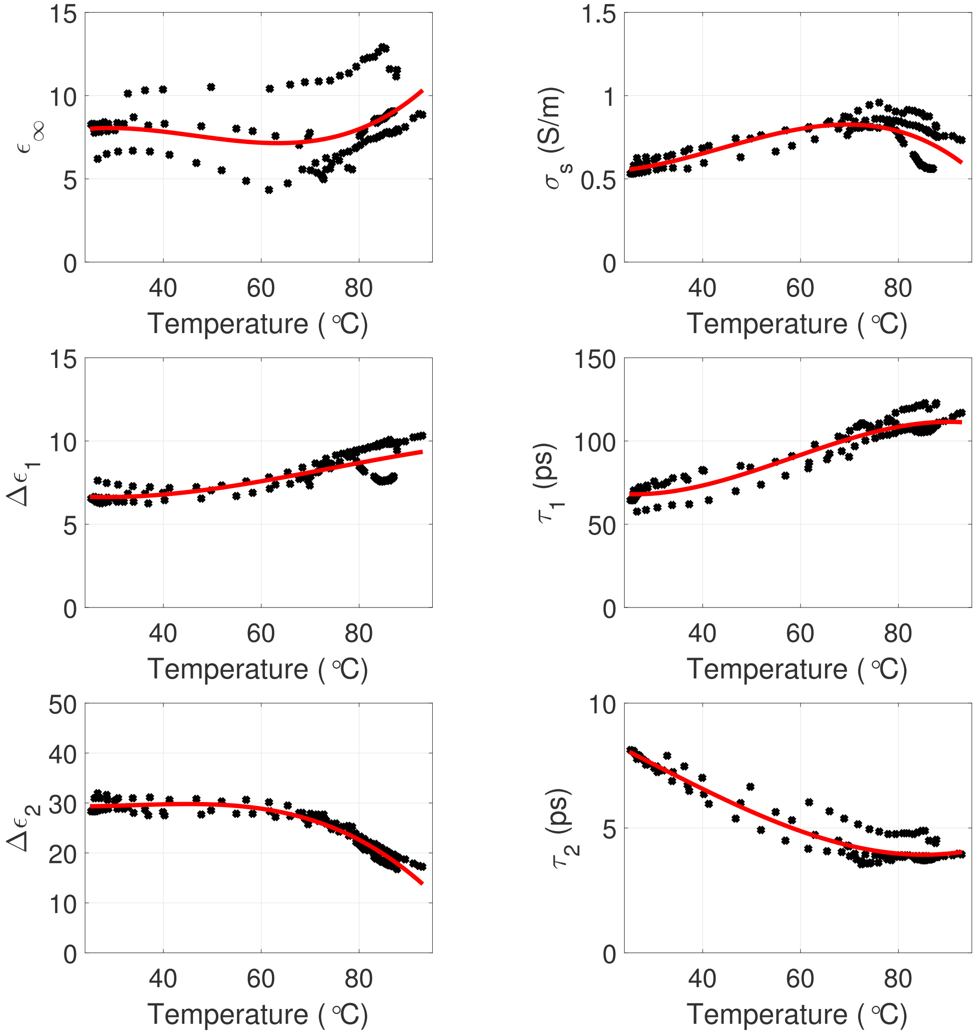

Figure 5.2: Two-pole Debye parameters as a function of temperature for each measurement (black) and the corresponding third-order polynomial fits (red).

Figure 3 shows our models for the dielectric properties—relative permittivity and conductivity—as a function of temperature for five representative frequencies: 1, 2.45, 5, 10, and 15 GHz. We observe that for the lower frequencies (i.e. 1 GHz and 2.45 GHz), the total decrease in relative permittivity is around 30-35% as temperature increases from

TABLE 5.1: Coefficients of third-order polynomial fit ($a_3t^3 + a_2t^2 + a_1t + a_0$) to each two-pole Debye parameter as a function of temperature (t in °C)

	a_3 ($\cdot 10^{-5}$)	a_2 ($\cdot 10^{-3}$)	a_1	a_0
ϵ_∞	4.48	-6.22	0.25	5.00
σ_s (S/m)	-0.42	0.55	-0.02	0.67
$\Delta\epsilon_1$	-0.90	2.00	-0.09	7.82
τ_1 (ps)	-32.88	57.36	-2.32	95.28
$\Delta\epsilon_2$	-8.56	8.71	-0.26	31.83
τ_2 (ps)	1.03	-0.87	-0.08	10.33

25°C to 93°C. A higher frequencies the relative permittivity initially increases with temperature and reaches a maximum at about 60°C. It then quickly decreases as the tissue temperature approaches 100°C. In contrast, the conductivity at frequencies greater than 5 GHz decreases steadily as a function of temperature. At frequencies below 5 GHz the conductivity increases slightly until the tissue reaches 70°C and then decreases.

Figure 4 shows a comparison between our dielectric properties model evaluated at 2.45 GHz and previously published data at 2.45 GHz [57, 30, 90]. We observe that our model is consistent with the trends reported in these previous studies within the range of overlapping temperatures and frequencies. Note that the results in [57] considered a maximum temperature of 60°C and that the temperature-dependent properties reported in [30] were measured only at 2.45 GHz during MWA. We also observe that the variability across these studies falls within the variability bars of the single-temperature, single-frequency study of [90]. The upward slope in conductivity for temperatures up to 60°C was also observed in [57], while [30] found a slight decrease in conductivity for this temperature range.

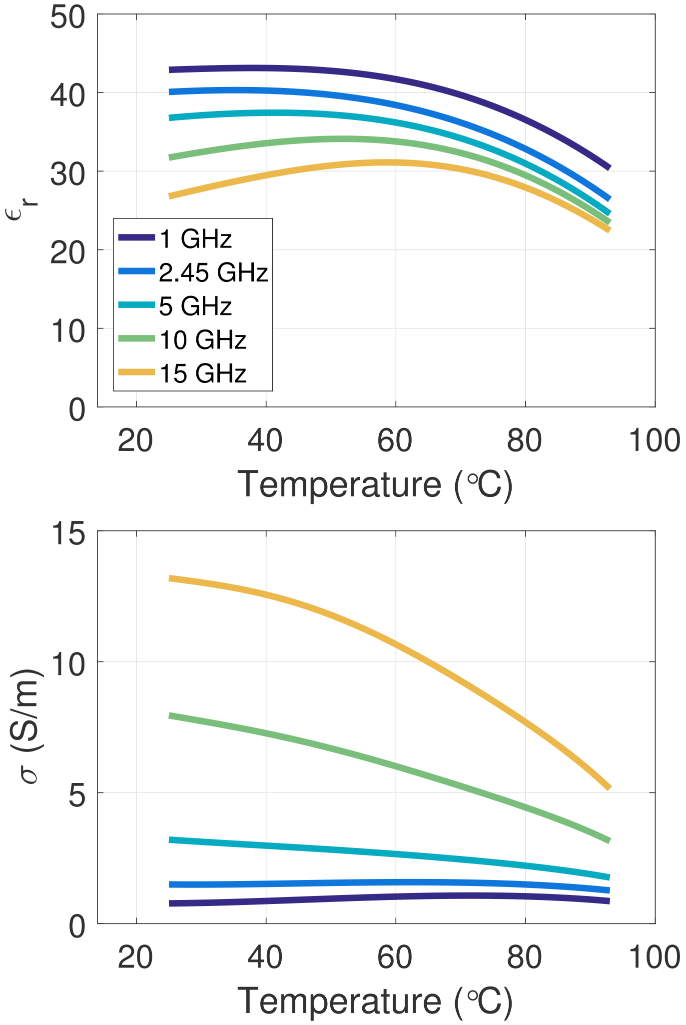

Figure 5.3: Relative permittivity and conductivity as a function of temperature during MWA ablation for five discrete frequencies calculated from the two-pole temperature-dependent Debye models.

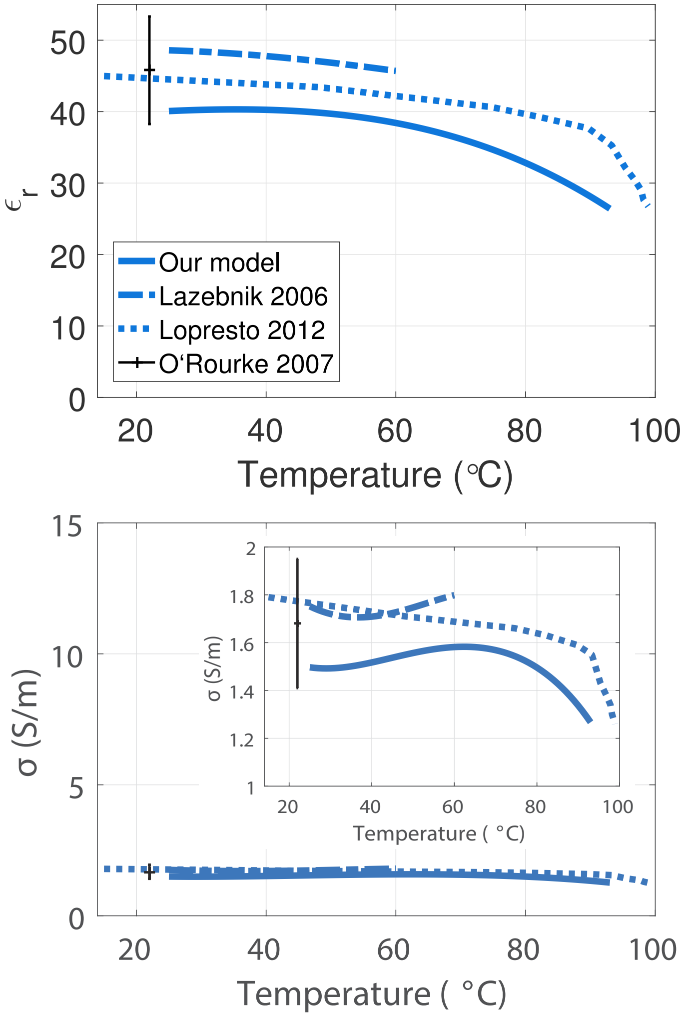

Figure 5.4: Comparison of models of relative permittivity and conductivity at 2.45 GHz of liver tissue as a function of temperature. The solid line corresponds to our model, the dashed line corresponds to the model in [57], the dotted line corresponds to properties measured during MWA [30], and the error bar corresponds to the variability observed in [90]. The insert in the conductivity plot shows greater detail by limiting the vertical axis range.

6 MICROWAVE ABLATION MONITORING IN REAL-TIME THROUGH MICROWAVE INVERSE SCATTERING USING PRE-COMPUTED PATIENT-SPECIFIC BREAST MODELS AND CANDIDATE ABLATION ZONES

6.1 Introduction

The lack of suitable imaging technologies for monitoring and verifying completeness of MWA is a limiting factor in the practical application of MWA for the treatment of cancer. The use of microwave imaging has long been investigated as a technique for monitoring hyperthermia treatment, for which the targeted temperature increase is typically less than 10 °C. In MWA treatments, the temperature increase is much higher, typically above 20 °C. The microwave-frequency dielectric properties of tissue undergo significant changes during ablation, not only because of the temperature dependence of the properties, but also because of the physiological changes as the tissue coagulates. The changes in the dielectric properties of tissue during ablation studied in Chapters 3 and 4 provide a strong physical basis for using microwave imaging to monitor MWA. However, conventional quantitative 3D microwave imaging algorithms for imaging high-contrast objects are computationally expensive and hence not suitable for real-time imaging. Additionally, the regularization techniques required to solve the inverse scattering ill-posed problem produce overly smooth images, making it difficult to determine an appropriate boundary for the ablation zone.

The proposed approaches estimate the ablation zone dimensions by choosing from a set of possible candidate ablation zones that are based on patient specific models. Real time monitoring can be achieved because all the expensive necessary electromagnetic simulations can be pre-computed.

6.2 Approach 1: Born Approximation

We can expect to know the dielectric properties of the breast before ablation to some extent, given that the patient will have had several medical images taken, including perhaps microwave imaging with spatial priors, which would at least provide an approximate 3D map of the dielectric properties inside the breast. Consider an array of antennas surrounding the breast, the dielectric properties of the breast pre-ablation to be the background properties for wave propagation, and the scatterer $\epsilon(\mathbf{r}')-\epsilon^b(\mathbf{r}')$ in Equation 2.1 to be the ablation zone at time $t = t_N$. The Green's function and the incident field for the background can be computed before the start of the ablation. For m source-observation channels and f frequencies we can build a set of mf equations of this form. Consider linearizing each equation by approximating the total field inside the volume by the field inside the volume when the scatterer is not present, i.e. $\mathbf{E}^t \approx \mathbf{E}^b$. This is known as the Born Approximation. Discretizing the equations as in [7], we can express this system as:

$$\mathbf{A}\mathbf{x} = \mathbf{b}. \tag{6.1}$$

Directly solving this problem using classical regularization techniques would result in overly smooth solutions for the ablation zone. We propose imaging the ablation zone by first defining a set of candidate ablation zones $\{\mathbf{x}_i\}_{i=1}^{n}$, where each $\mathbf{x}_i$ is the dielectric contrast of a particular candidate ablation zone. The ablation zone at time $t = t_N$ can be estimated by finding the $\mathbf{x}_i$ that best solves 6.1, i.e. the $\mathbf{x}_i$ that solves the problem:

$$\text{Minimize}_i \|\mathbf{A}\mathbf{x}_i - \mathbf{b}\|_2. \tag{6.2}$$

The appropriate shapes, sizes, and dielectric contrast of the candidate ablation zones can be defined by using *a priori* knowledge about the evolution of the ablation zone (Aim 2).

Because the electromagnetic simulations for wave propagation in the background (tissue pre-ablation) can be computed before the start of the ablation, this approach is suitable for real-time monitoring. Only a quick comparison of the cost function in 6.2 for the different candidate ablation zones has to be done at time $t = t_N$.

A clear limitation of this approach is that the Born Approximation breaks down when the scatterer is big or its dielectric contrast is high. Preliminary studies on the effects of MWA on dielectric properties have shown reduction in relative permittivity as high as 40% for liver tissue [30], and depending on the size of the tumor the target ablation zone size can be of various centimeters in diameter. To overcome this limitation, we present Approach 2.

6.3 Approach 2: Updated Born Approximation

Instead of approximating at every time $t = t_N$ the total field inside the volume, $\mathbf{E}^t$, by the field obtained when the scatterer is not present, consider approximating the total field by the field obtained when the scatterer corresponds to the ablation zone estimated at time $t = t_{N-1}$, i.e. when the properties inside the volume are $\epsilon^b + \hat{\mathbf{x}}^{N-1}$. This leads to a system of equations $\mathbf{A}'\mathbf{x} = \mathbf{b}$ for every time $t = t_N$ during the ablation. As in the first approach, the ablation zone is estimated by choosing the candidate ablation zone $\mathbf{x}_i$ that best solves the system.

This approach updates the Born Approximation every time the estimated ablation zone changes, allowing for higher dielectric contrast and larger ablation zones to be the scatterer in the electric field integral equations. The rationale for updating the approximation of the total field with the field given the current estimate is that the size of the ablation zone increases slowly, therefore the estimate of the ablation zone at time $t = t_{N-1}$ provides a good approximation for computing the total field inside the volume. This approach requires computing the electric field inside the volume for every candidate ablation zone. However, despite the extra computations, this approach is still suitable for real-time monitoring because all the expensive electromagnetic simulations can be done before the start of the ablation.

6.4 Approach 3: Compare measured and simulated fields

Here we present a very straightforward way of estimating the ablation zone at a time $t = t_N$. It consists of comparing the measured fields at the observation points with simulated fields at the observation points for each candidate ablation zone. We choose the candidate ablation zone $\mathbf{x}_i$ that minimizes $\|\mathbf{E}_{\text{measured}} - \mathbf{E}^{\epsilon^b+\mathbf{x}_i}_{\text{simulated}}\|_2$.

This approach also requires to compute the electric fields for each candidate ablation zone before the start of the ablation. It is more simple to implement, but the robustness to noise and to errors in the model have to be evaluated.

6.5 Performance evaluation: Homogeneous tissue in 2D

Test bed and simulation set up

The first simulation test bed for evaluating the performance of the three approaches is simulations of ablations of homogeneous tissue in 2D. In particular, the tissue has an ellipsoidal shape with frequency-dependent dielectric properties of average fibroglandular tissue, as determined in [10], and it is surrounded by a layer of skin of 2 mm. The ablation zone has circular shape, growing up to 15 mm in radius. Because the dielectric contrast of ablated tissue is still being studied, two dielectric contrasts of ablation zones were considered: low, which corresponds to a 20% drop in relative permittivity and 15% drop in effective conductivity, and high, which corresponds to a 40% drop in relative permittivity and 30% drop in effective conductivity. Figure 6.1 shows the test bed for the two contrasts of ablation zones investigated.

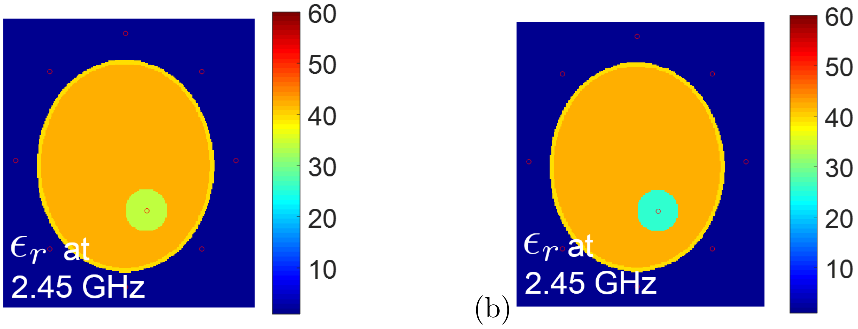

(a) (b)

Figure 6.1: Simulation test beds for the (a) low contrast ablation zone and (b) high contrast ablation zone of homogeneous tissue in 2D.

An array of 8 antennas in air surrounding the tissue and one antenna inside the breast (which can be the MWA antenna) was considered to transmit and receive the signals. Measurements during ablation were simulated using FDTD, and were recorded at 2.4, 2.45, and 2.5 GHz. For each simulated ablation, measurements were recorded 100 times when the ablation zone was 1, 3, 5, 7, 9, 11, 13, and 15 mm. White Gaussian noise was added to every simulated measurement.

The candidate ablation zones were also considered to be circular and centered at the MWA antenna. Low contrast candidate ablation zones were considered for the low contrast ablation case, and high contrast candidate ablation zones were considered for the high contrast ablation case.

Robustness to errors in background properties

It is likely that our knowledge of the properties of the pre-ablated tissue will not perfect. To study the robustness of these approaches to errors in the assumed background properties we perform two experiments: a scenario in which the assumed relative permittivity of the background is underestimated by 5%, and a scenario in which the assumed relative permittivity of the background is overestimated by 5%.

The dielectric properties of the candidate ablation zones will be based, as before, on a percent drop with respect to the background properties. Since the background will be under or over estimated, the error will propagate to the set of candidate ablation zones. In other words, not any candidate ablation zone will provide an exact match to the actual ablation zone.

Results

Figure 6.2 shows the results for estimating the size of the ablation zone for the simulated ablations using the three approaches. The first row shows the result for the low contrast ablation case and the second row shows the results for the high contrast ablation case. The SNR in these cases was 30 dB. In each plot the darkness of the square above the actual ablation zone size (x-axis) correlates to the number of times the ablation zone was estimated to be a certain size (y-axis). The dotted line corresponds to the desired estimation. Using the Born Approximation (approach 1) results in poor estimates of the ablation zone size when the contrast of the ablation is large. Updating the Born Approximation (approach 2) and comparing the measured fields to pre-computed simulations of different ablation zone candidates (approach 3) produces good estimates of the ablation zone size for both the low contrast and high contrast ablation cases.

Figure 6.3 shows the results for a high noise scenario, particularly an SNR of 10 dB. In this case, several estimation errors of up to 4 mm in radius occur in the low contrast case. However, approaches 2 and 3 perform much better when the contrast of the ablation zone is high, reducing the error to only ±2 mm.

Figure 6.4 shows the results for an SNR of 30 dB when the assumed relative permittivity of the background is underestimated (first row) and overestimated (second row). Focusing on the performance of approaches 2 and 3, we can conclude that when the properties of

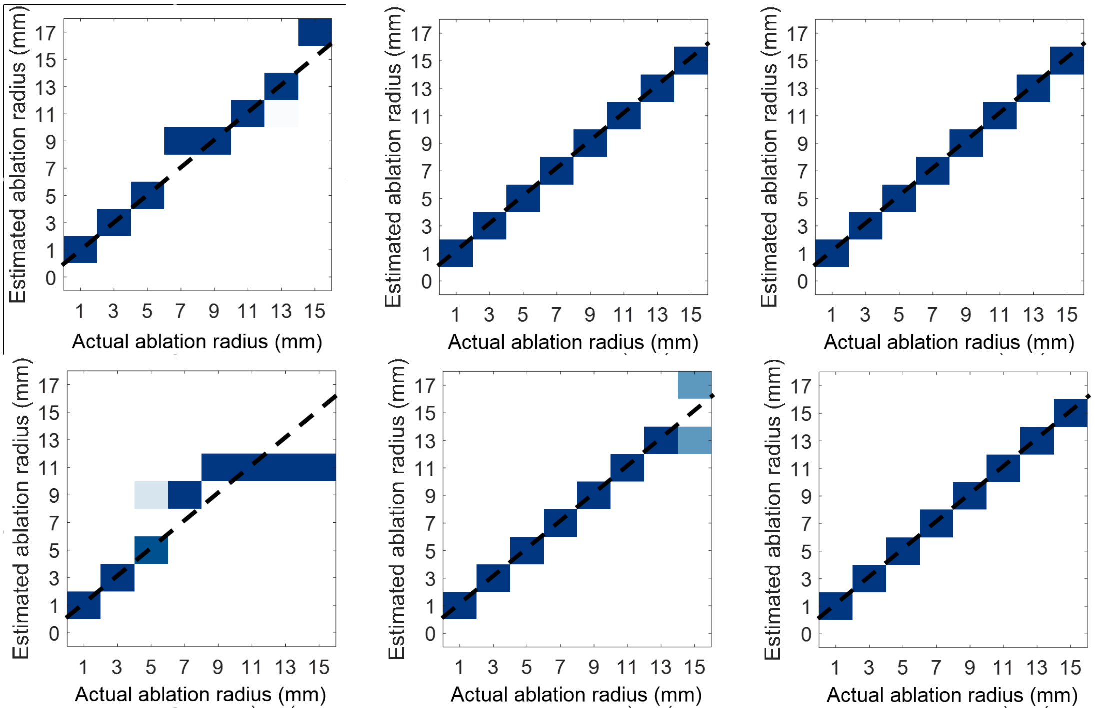

Figure 6.2: Approach 1: Born Approximation (left column), Approach 2: Updated Born Approximation (middle column), and Approach 3: Compare fields (right column) results for ablation of homogeneous tissue in 2D with a 30 dB SNR. The first row shows results for the low contrast ablation zone, and the second row shows results for the high contrast ablation zone.

the assumed background are underestimated, the estimated ablation zone size is generally smaller than the actual ablation zone. Contrarily, when the properties of the assumed background are overestimated, the size of the ablation zone is generally overestimated.

6.6 Performance evaluation: Heterogeneous breast tissue in 2D

Test bed and simulation set up

Now we will study how these approaches perform in simulations of ablations of heterogeneous breast tissue in 2D. A 2D cross section of the Class 3 breast phantom in [67] was chosen to represent the pre-ablated tissue. The ablation zone was considered to be circu-

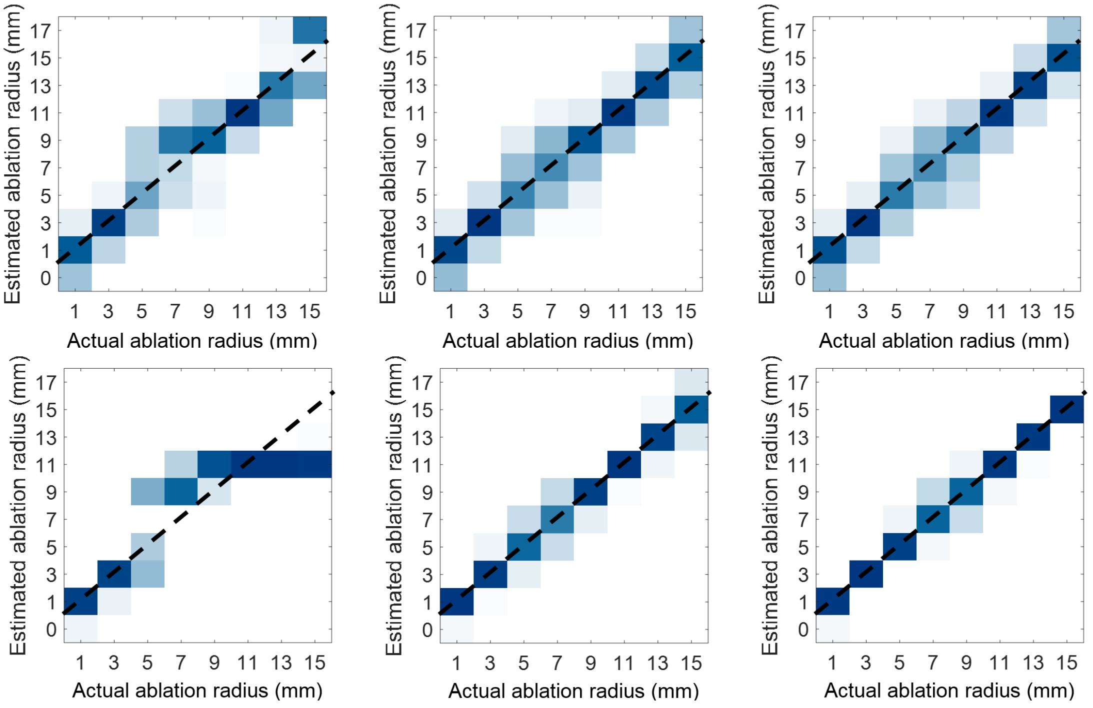

Figure 6.3: Approach 1: Born Approximation (left column), Approach 2: Updated Born Approximation (middle column), and Approach 3: Compare fields (right column) results for ablation of homogeneous tissue in 2D with a 10 dB SNR. The first row shows results for the low contrast ablation zone, and the second row shows results for the high contrast ablation zone.

lar, growing up to 15 mm in radius. In this case, we assumes that only the properties of fibroglandular tissue are affected by the ablation. In particular, we assume a drop of the properties of the tissue to a value of 80% of the relative permittivity of healthy fibroglandular tissue and 85% of the effective conductivity of healthy fibroglandular tissue. Figure 6.5 (a) shows the test bed for this simulation.

Similarly to the setup for homogeneous tissue, an array of 8 antennas in air surrounding the breast and one antenna inside the breast was considered to transmit and receive the signals. Measurements during ablation were simulated using FDTD, and were recorded at 2.4, 2.45, and 2.5 GHz. For each simulated ablation, measurements were recorded 100 times when the ablation zone was 1, 3, 5, 7, 9, 11, 13, and 15 mm. White Gaussian noise was added to every measurement.

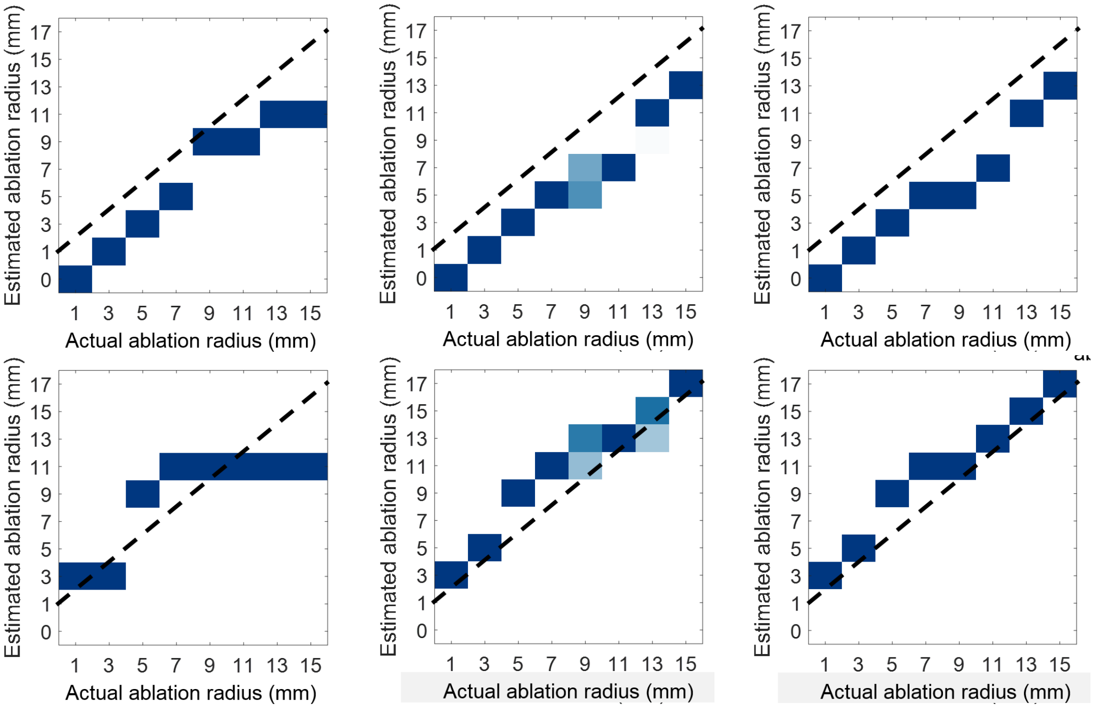

Figure 6.4: Approach 1: Born Approximation (left column), Approach 2: Updated Born Approximation (middle column), and Approach 3: Compare fields (right column) results for the ablation of homogeneous tissue in 2D with a 30 dB SNR. The first row shows results for an underestimated background, and the second row shows results for an overestimated background.

The candidate ablation zones were considered to also be circular centered at the MWA antenna and affecting only fibroglandular tissue.

Robustness to errors in background properties

In this case we will consider a different type of error for studying the robustness of these approaches to errors in the background properties. We assume we know the location of the different types of tissues in the breast: adipose and fibroglandular, and their average properties, not their spatial heterogeneous distribution. Figure 6.6 shows the exact distribution of dielectric properties of the 2D breast slice pre-ablation and the approximated background.

As before, because the dielectric contrast of the candidate ablation zones is based on

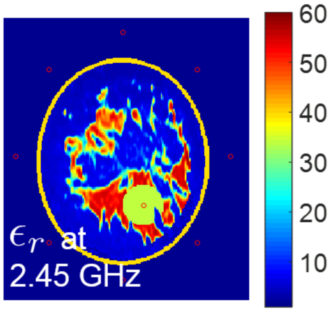

Figure 6.5: Simulation test bed for the ablation of a 2D cross-section of breast tissue.

our estimation of the background, there will be an inevitable error and not any candidate ablation zone will provide an exact match to the actual ablated breast.

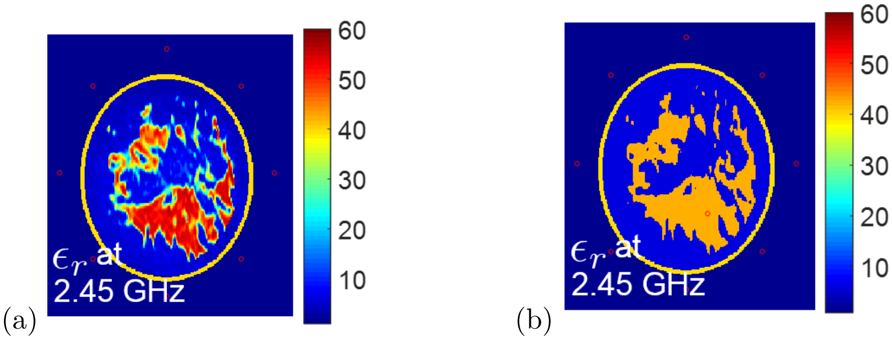

(a) (b)

Figure 6.6: (a) Exact distribution of dielectric properties of the breast pre-ablation) and (b) approximated distribution of dielectric properties of the breast pre-ablation.

Results

Figure 6.7 shows the results for estimating the size of the ablation zone for an ablation using the three approaches in a low noise scenario (SNR = 30 dB). The first row shows the results for when there is perfect knowledge of the properties of the pre-ablated breast. In this case we see that updating the Born Approximation (approach 2) and comparing the measured and simulated fielsd (approach 3) perform perfectly. Using the Born Approximation by itself (approach 1) fails when the size of the ablation zone is large.

The second row in 6.7 shows the results for when the properties of the breast pre-ablation are correspond to the approximate model. In this case we observe errors for all approaches, usually underestimating the ablation zone size.

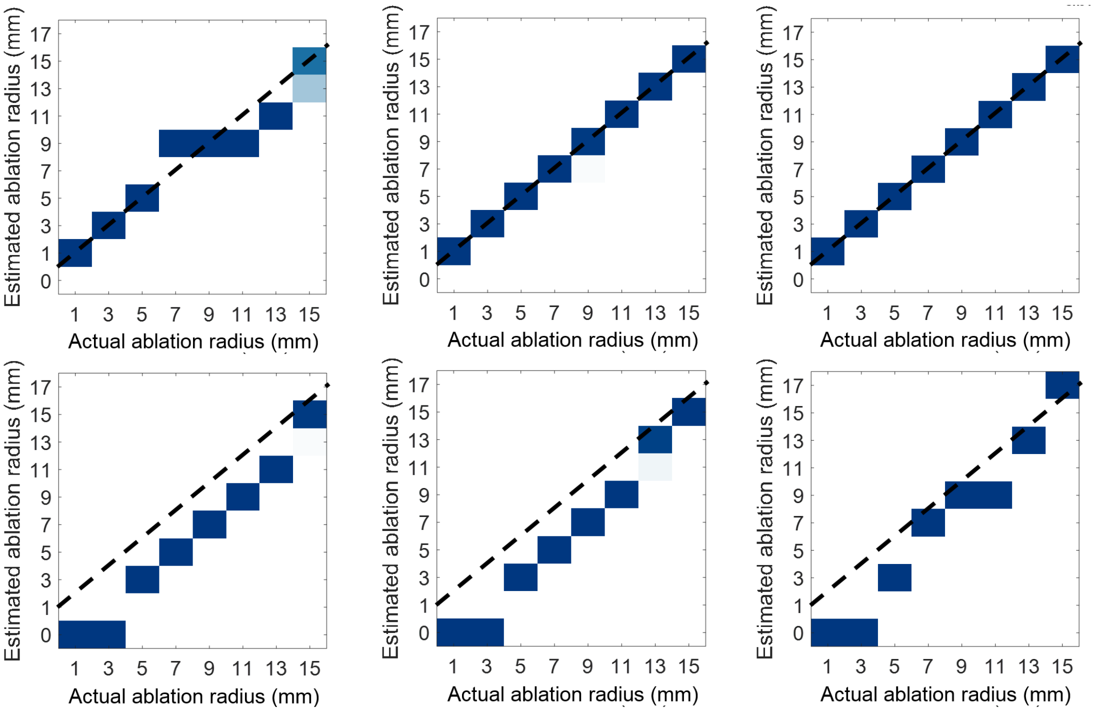

Figure 6.7: Approach 1: Born Approximation (left column), Approach 2: Updated Born Approximation (middle column), and Approach 3: Compare fields (right column) results for ablation of heterogeneous breast tissue in 2D with a 30 dB SNR. The first row shows results with exact knowledge of the pre-ablation properties, and the second row shows results with assumed approximate pre-ablation properties.

6.7 Performance evaluation: Homogeneous tissue in 3D

Test bed and simulation set up

Finally, the performance of the approaches will be evaluated on simulations of ablations of homogeneous tissue in 3D. In particular, we will consider tissue that is shaped like the breast and has a 2 mm external layer of skin, but the inside is homogeneous with frequency-dependent dielectric properties as average fibroglandular breast tissue [10]. The ablation zone is considered to be spherical, growing up to 15 mm in radius, with a dielectric contrast corresponding to a drop of 40% in relative permittivity and 30% in effective conductivity. This can be considered a high contrast scenario. Figure 6.8 shows the test bed for this investigation.

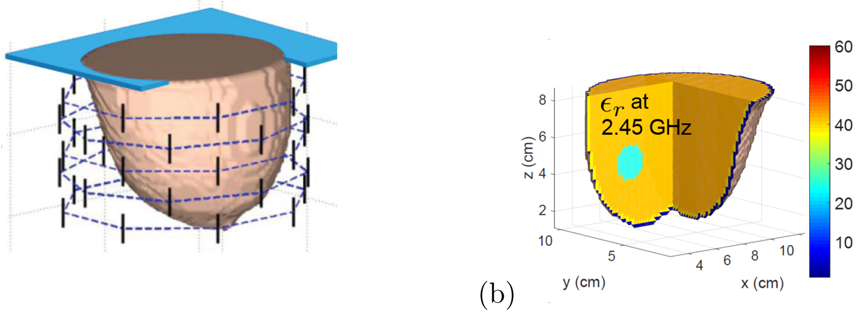

(a) (b)

Figure 6.8: Simulation test beds for 3D ablations of homogeneous tissue. (a) Antenna array and (b) distribution of dielectric properties of the tissue during ablation.

An array of 40 antennas in air surrounding the breast was considered to transmit and receive the signals. Measurements during ablation were simulated using FDTD, and were recorded at 2.4, 2.45, and 2.5 GHz. For each simulated ablation, measurements were recorded 100 times when the ablation zone was 1, 3, 5, 7, 9, 11, 13, and 15 mm. White Gaussian noise was added to each measurement. The candidate ablation zones were considered to also be spherical.

Results

Figure 6.9 shows the results for the three approaches. Using the Born Approximation (approach 1) performs very poorly in this case. However, updating the Born Approximation (approach 2) and comparing the fields (approach 3) perform very well, especially as the ablation zone gets larger in size.

6.8 Discussion and Conclusion

Three microwave imaging approaches were proposed for monitoring MWA. These approaches use pre-computed data and a set of candidate ablation zones based on patient-specific models and *a priori* knowledge of the evolution of the ablation zone. Therefore, these approaches are suitable for real-time monitoring of MWA.

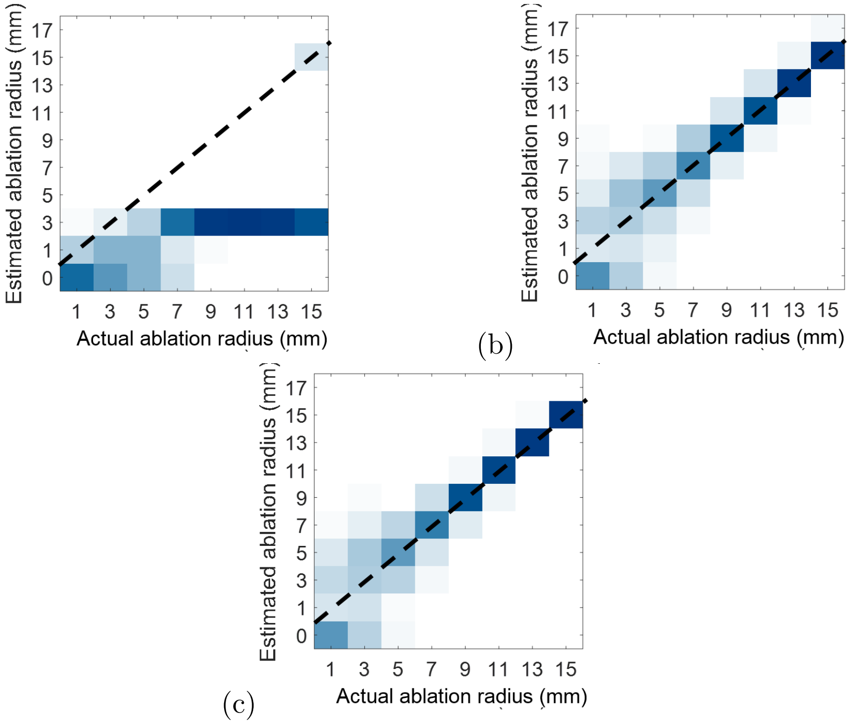

(a) (b) (c)

Figure 6.9: Approach 1: Born Approximation (left column), Approach 2: Updated Born Approximation (middle column), and Approach 3: Compare fields (right column) results for ablation of homogeneous tissue in 3D with a 30 dB SNR.

Performance evaluation of these approaches was conducted under a set of different scenarios, starting from a simple case of ablation of homogeneous tissue in 2D to ablation of heterogeneous tissue in 2D. Finally validation of the performance of these approaches was obtained for 3D in a simulation of an ablation of homogeneous tissue. The accuracy of the estimations was observed assuming perfect knowledge of the dielectric properties of pre-ablated tissue and ablated tissue, and for when there are errors in the assumed properties of the pre-ablated tissue.

Updating the Born Approximation (approach 2) and comparing the measured fields to simulated fields (approach 3) to find the ablation zone size proved to be very accurate at estimating the ablation zone size. Both methods performed similarly. Using the Born Approximation failed for large ablation sizes and high contrast ablation zones, as expected. Errors in the assumed background led to errors in estimating the ablation zone size. An underestimated assumed background led to underestimation of the ablation zone size, while an overestimated background led to overestimation of the ablation zone size. For the complex scenario of ablation of heterogeneous breast tissue, we found that the approximate model did not provide good estimates of the ablation zone size, generally underestimating it. This leads to believe that average properties of the different tissues in the breast might not be a good enough approximation of the background properties in this heterogeneous environment.

Even though these approaches provide reasonably good estimates, further studies in 3D need to be performed more thoroughly to evaluate their performance. All three approaches, especially approaches 2 and 3, rely heavily on computational electromagnetic simulations that have to be performed before the start of the ablation. Also, they rely heavily on the model of the tissue pre-ablation and on the model of the evolution of the ablation, for example, on the ablation zone shape and its dielectric properties.

7 REAL-TIME MONITORING OF MICROWAVE ABLATION USING A SPATIAL TEMPERATURE MODEL AND A TIME-DIFFERENCE-OF-ARRIVAL METHOD

This chapter is intended for submission to the *IEEE Transactions on Antennas and Propagation.*

7.1 Abstract

Microwave ablation is a cancer treatment that rapidly achieves malignant tissue denaturation and necrosis by heating the cells to cytotoxic temperatures. Due to the short duration of microwave ablation treatments, real-time monitoring is crucial to ensure treatment is complete and temperatures are safely maintained in healthy tissue. Microwave imaging has recently been explored as a monitoring modality, as there is a strong correlation between the tissue's dielectric properties and temperature. In this paper, we present a microwave imaging method that combines the time-difference of arrival of sensing signals with spatial models of the temperature during ablation to accurately estimate tissue temperature in real-time. We obtain and model the spatial distribution of the temperature during ablation using coupled electromagnetic-thermal computational simulations. We demonstrate that our method achieves highly accurate results for ablations at different power levels in the presence of noise.

7.2 Introduction

Microwave ablation (MWA) is a cancer treatment that achieves malignant tissue denaturation and necrosis by heating the cells to cytotoxic temperatures, usually above 50 °C [26]. The tissue is targeted through a minimally invasive interstitial antenna, and the energy is delivered in a volume around the ablation antenna. MWA can treat larger volumes in a shorter amount of time and is less sensitive to the effects of blood perfusion than other thermal therapies such as radiofrequency ablation and hyperthermia [91, 21].

Due to the shorter duration of MWA treatments, which usually last less than 10 minutes, real-time monitoring of the procedure is crucial to ensure completeness of the treatment and avoid targeting tissue beyond the malignancy. Ultrasound is useful to precisely position the ablation antenna at the center of the target zone, but the formation of microbubbles during the ablation procedure hides the ablated region, limiting its usefulness for real-time monitoring [27]. Magnetic resonance imaging is effective at imaging the ablated region but has several drawbacks regarding cost and compatibility, and its lack of portability makes it impossible to follow the progression of the ablation in real-time [28, 92]. Fiber-optic temperature probes are useful for monitoring the temperature of the tissue, but the information they provide is limited to where the tip of the probe is placed.

In recent years, microwave imaging, which maps the dielectric properties or dielectric contrast of the imaging volume, has been explored as a MWA monitoring modality. The rationale for using microwave imaging relies on studies that show that the dielectric properties of the tissues change during ablation, due to a strong temperature dependence. Furthermore, there is an irreversible change in dielectric properties once the tissue has been damaged [84, 30, 31, 57]. The microwave imaging techniques that have been recently explored are either based on inverse scattering methods [93, 62] or radar methods [94, 61]. In inverse scattering, the imaging volume is illuminated with electromagnetic fields radiated from antennas outside surrounding the volume, and the scattered fields are processed to determine the dielectric properties inside the volume. The temperature map is obtained by correlating the dielectric properties to temperature. These methods rely heavily on linear approximations of the inverse scattering problem, which is also highly ill-posed; therefore the accuracy and resolution of the obtained images are limited [39]. A radar method proposed by Kidera *et al.* [94] uses the time difference of arrival (TDOA) from signals sent from the ablation antenna itself to an array of antennas outside the imaging volume to determine the extent of the ablation zone. This method proved to have good results in cases where the ablation zone consisted of a uniform change in dielectric properties. However, in reality, the ablation zone's temperature and dielectric properties are smooth and heterogeneous; therefore the method is not suitable in realistic scenarios.

In this paper we extend the TDOA method to estimate the temperature profile of the tissue during ablation in realistic scenarios. We accomplish this by modeling the spatial distribution of temperature during ablation and including it in the solving part of the TDOA problem. Recent literature on the temperature dependence of dielectric properties of liver tissue during MWA for a wide range of frequencies and temperatures [84] allowed us to study the evolution of ablation of liver tissue accurately by using coupled electromagnetic (EM)-thermal computational simulations, which allowed us to update the SAR pattern due to the changing dielectric environment as the ablation progresses. From these simulations, we obtained and modeled the spatial distribution of temperature of the tissue during ablation. This information can be combined with a TDOA calculation to estimate the temperature around the antenna during ablation accurately.

This paper is organized as follows. Section II presents the methods, which include the coupled computational simulations of MWA at different power levels and the importance of incorporating temperature-dependent dielectric properties to the simulations, the analysis of the spatial profiles of the temperature at any moment during ablation and our spatial temperature model, and our method which incorporates this model to a TDOA calculation. Section III presents the results of the algorithm and evaluates its performance for different ablation power levels and added noise. Section IV concludes.

7.3 Methods

Computational Simulations

CST Microwave Studio is used for our coupled EM-thermal computational simulations of MWA of liver tissue. We chose the floating-sleeve dipole (FSD) antenna design from [85] operating at 1.9 GHz as the ablation antenna because it performs well over a wide frequency range and has a compact specific absorption rate (SAR) pattern. The radius of the antenna is 1.75 mm, and it is inserted vertically in the center of a block of liver tissue. The simulated dimensions of the liver tissue are 24 cm wide and deep, and the tip of the antenna is placed 3 cm above the bottom of the tissue. This ensures the microwaves are highly attenuated before reaching any tissue boundary.

The wide-band dielectric properties assumed for the liver tissue are based on [84], and the tissue is considered to be at normal body temperature, *i.e.* 37 °C, at the beginning of the simulation. During the course of the simulation, the tissue dielectric properties are adjusted due to the temperature changes every 10 seconds. This modifies the SAR pattern throughout the tissue. The time step interval of 10 s produces a smooth change in temperature for every location in the tissue for 20 W to 40 W of input power. We simulate five-minute ablations and assume that during the ablation the tissue is subject to blood perfusion as in [95].

Figures 7.1, 7.2, and 7.3 highlight the importance of incorporating the temperature dependence of the dielectric properties of the tissue in the simulations of MWA. The figures show results for ablation at 40 W. Figure 7.1 compares the maximum temperature reached

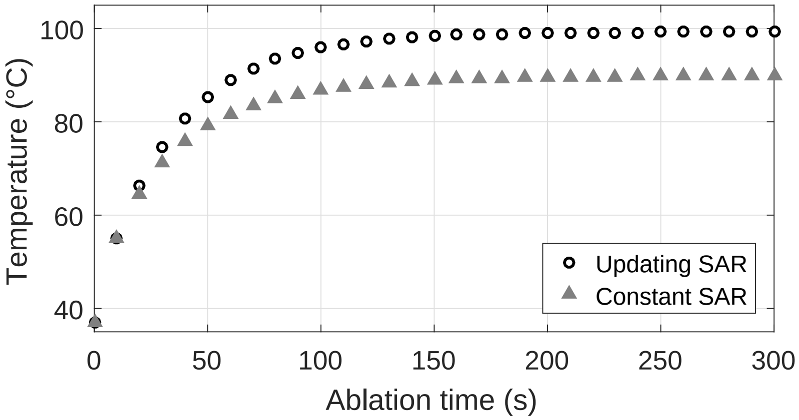

Figure 7.1: Maximum temperature of liver tissue during coupled electromagnetic-thermal computational simulation of microwave ablation at 1.9 GHz and 40 W updating the SAR pattern every 10 s during ablation (black circles), and without updating the SAR pattern, *i.e.* keeping the SAR pattern constant as determined by the initial homogeneous dielectric properties of the tissue (gray triangles).

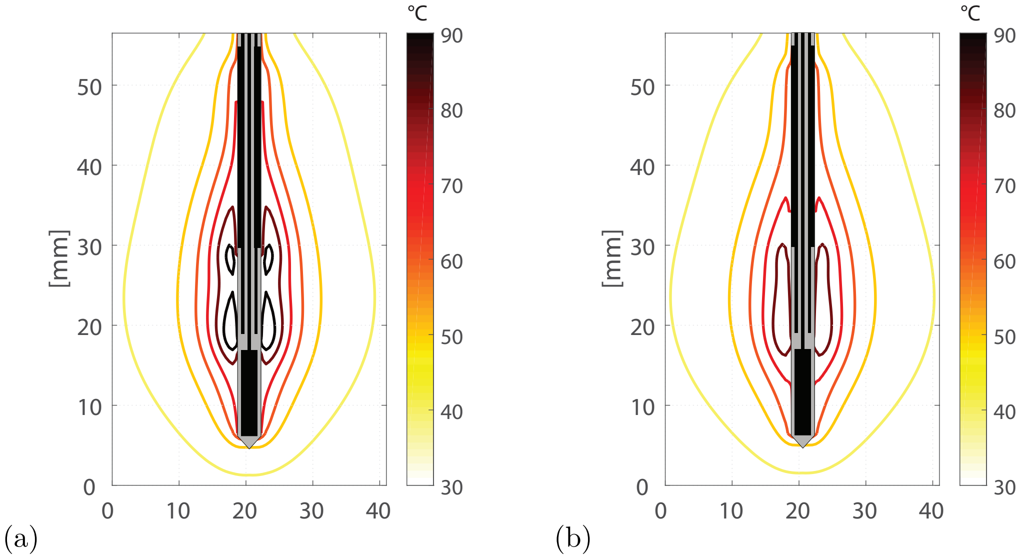

(a) (b)

Figure 7.2: 2D cross-sections through the center of the antenna of the temperature profiles of the tissue after 300 s of simulated ablation at 1.9 GHz and 40 W. (a) Updating the SAR pattern every 10 s during ablation, and (b) without updating the SAR pattern.

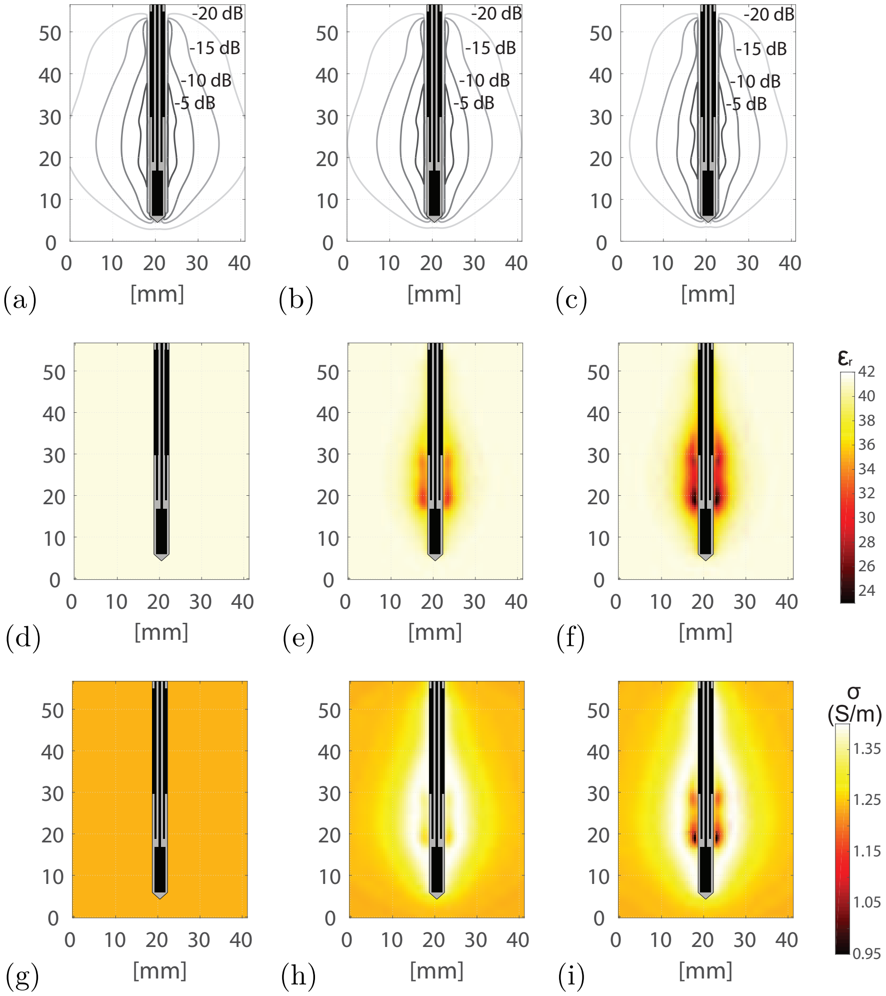
(a) (b) (c) (d) (e) (f) (g) (h) (i)

Figure 7.3: 2D cross-sections through the center of the antenna of the evolution of SAR pattern (a,b,c), relative permittivity at 1.9 GHz (d,e,f), and conductivity at 1.9 GHz (g,h,i) during ablation at 1.9 GHz and 40 W using temperature-dependent dielectric properties model in [84]. The left column shows the properties before ablation, the center column shows the properties after 60 s of ablation, and the right column shows the properties after 300 s of ablation.

by the tissue during the ablation when the dielectric properties' temperature dependence is incorporated and when it is not incorporated. The temperature of the tissue increases more rapidly when the dependency is considered, and the temperatures reached are considerably higher, *i.e.* more than 10 °C after five minutes of ablation. These higher temperatures agree with what has been observed in experimental studies such as [95, 84]. Figure 7.2 shows a 2D cross-section through the center of the ablation antenna of the temperature profile at the end of the five minutes of ablation. The ablated region, considered to be the region where the tissue reaches temperatures above 50 °C, is slightly more compact and reaches higher temperatures when temperature dependent dielectric properties are incorporated.

Figure 7.3 shows the same 2D cross-section as Fig. 7.2 but of SAR pattern, relative permittivity at 1.9 GHz, and conductivity at 1.9 GHz at different times during the ablation ($t = 0$ s, $t = 60$ s, $t = 300$ s). Here we can see the evolution of the electromagnetic properties of the setup during the ablation. Note that over time the SAR pattern becomes more compact, the relative permittivity decreases, especially close to the antenna, and the conductivity decreases next to the antenna but increases in the region further around it. The trends in these results were observed for ablations at different input power levels up to 40 W. Power levels greater than 40 W resulted in tissue temperatures exceeding 105 °C, the maximum temperature for which we had dielectric properties' information. Therefore we did not include power levels greater than 40 W in our analysis.

Spatial Distribution of Temperature During MWA and Exponential Model

Figure 7.4 shows the 1D temperature profile of the liver tissue as a function of distance from the center of the antenna at different times during ablation for 40 W and 30 W input power. The direction of these temperature profiles is perpendicular to the ablation antenna, and they extend outward from its dipole gap. We observe that the tissue reaches its maximum temperature between 2.25 and 2.75 mm away from the antenna. From the location of maximum temperature, the tissue temperature decreases rapidly as a function of distance from the antenna.

We fit exponential decay curves of the form

$$T(x) = a \cdot e^{-bx} + 37, \quad \text{for } x \geq 2.5 \text{ mm} \tag{7.1}$$

to the temperature decays for ablations at 20 W, 30 W, and 40 W, every 10 seconds during the ablation. The dashed lines in Fig. 7.4 show the corresponding exponential fits. The values of a and b in the fits ranged between $[18.48, 109.27]$ and $[-0.2728, -0.1901]$ respectively. The average and standard deviation of the RMSE of the 30 fits during the 40

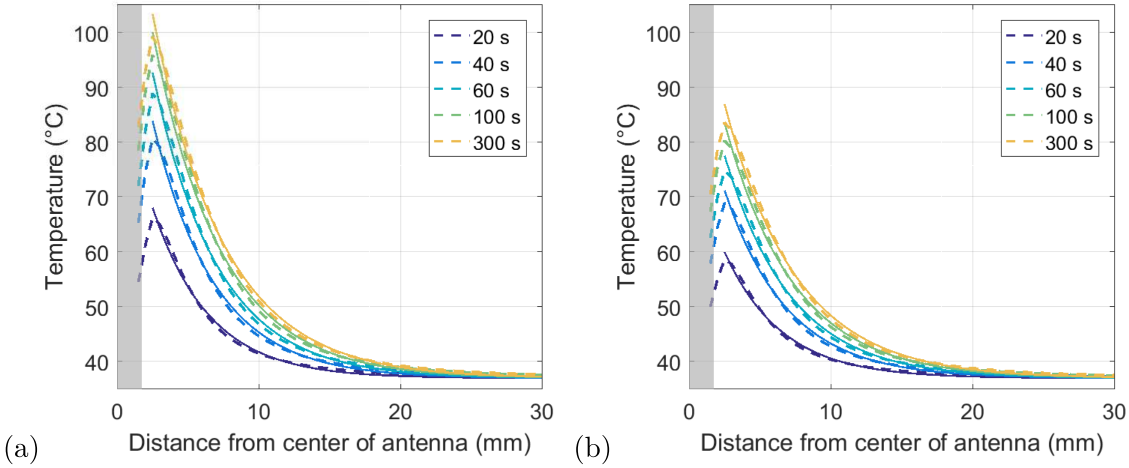

(a) (b)

Figure 7.4: 1D temperature profiles as a function of distance from the center of the antenna during ablation (dashed lines), and their corresponding exponential decay fits (solid lines) for (a) 40 W ablation and (b) 30 W ablation (b). The profile extends from the dipole gap in the direction perpendicular to the antenna. The shaded area corresponds to the extent of the MWA antenna.

W ablation were 0.59 ± 0.09 °C, for the 30 W ablation were 0.48 ± 0.08 °C, and for the 20 W ablation were 0.32 ± 0.06 °C. These average errors of less than a degree provide strong support for modeling the spatial distribution of temperature using the exponential model (Eq. 7.1).

TDOA Method With Incorporated Temperature Spatial Distribution Model

Figure 7.5 shows the data acquisition configuration for the MWA monitoring strategy. The FSD ablation antenna is used to ablate the liver tissue and send out a Gaussian pulse every few seconds (or a synthesized Gaussian pulse) that is used for monitoring. In our ablation simulations we use a Gaussian pulse centered at 2.45 GHz. An identical FSD antenna is placed at a distance from the ablation antenna. This antenna records the received pulses. The elapsed time of the ablation is denoted by t, where $t = 0$ corresponds to a time before the ablation or just at the start of the ablation, as shown in Fig. 7.5(a), and $t > 0$ corresponds to a time during the ablation, as shown in Fig. 7.5(b). This setup allows us to estimate the temperature profile between the two antennas at the depth of the active-most portion of the antennas, which corresponds to the dipole gap.

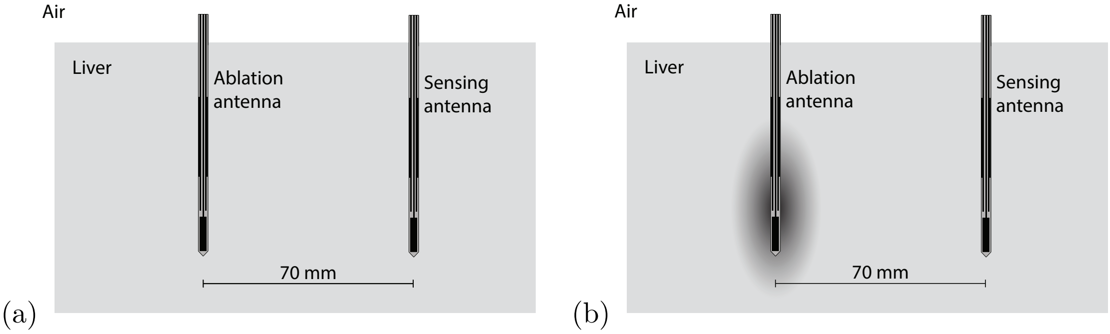

Figure 7.5: 2D cross-section of the data acquisition setup on plane through the center of antennas. (a) Before the ablation at time $t = 0$ s. (b) During the ablation at a time $t > 0$ s. The dark gray area corresponds to the ablation zone.

The dielectric properties of the tissue change spatially during the course of the ablation. This change leads to a TDOA between the signal before ablation ($t = 0$) and the signals during ablation ($t > 0$). The TDOA of a signal at a time $t = n$, $n > 0$, during ablation can be measured, or estimated by the following cross-correlation calculation:

$$\Delta\tau_n = \text{argmax}_\tau [s_0(y) * s_n(y)](\tau) \tag{7.2}$$

where $s_0(y)$ is the received time signal before ablation at $t = 0$, $s_n(y)$ is the received time signal during ablation at $t = n$, and $*$ denotes the cross-correlation operator.

Theoretically, in a one-dimensional non-dispersive wave propagation scenario, the TDOA between two signals traveling between a point $x = 0$ and $x = D$ through a changing dielectric environment is equal to the space integral of the difference of the inverse of the propagation speeds of the waves throughout the trajectory of propagation, as in the following calculation:

$$\Delta\tau_n = \int_{x=0}^{x=D} \left(\frac{1}{v_n(x)} - \frac{1}{v_0(x)} \right) dx \tag{7.3}$$

where $v_n(x)$ is the propagation speed of the wave through the tissue at time $t = n$ and $v_0(x)$ is the propagation speed at time $t = 0$.

In our TDOA algorithm, we will compute the TDOA using the previous expression and making some assumptions. We assume a discrete domain where the propagation speed at each location can be estimated by using the relative permittivity at frequency f of the tissue at that location. The frequency f is chosen to be the predominant frequency present in the signals received by the sensing antenna. For our data acquisition setup and Gaussian pulse, the predominant frequency of the received signal is $f = 1$ GHz. Also, we discretize the grid to 0.5 mm voxels. In our setup, the trajectory between $x = 0$ and $x = D$ corresponds to the path between the ablation antenna and the sensing antenna located at a distance D. Therefore, the variable x can also be regarded as the distance from center of the ablation antenna, in the direction perpendicular to the antenna extending outward from its dipole gap. The propagation speed of the wave throughout the tissue before the ablation is denoted as $v_0(x)$ and during the ablation at a time $t = n$ it is denoted as $v_n(x)$.

In this way, the propagation speed before ablation can be estimated by:

$$v_0(x) = \frac{c}{\sqrt{\epsilon_{r,0}}} = v_0 \tag{7.4}$$

where c is the speed in vacuum and $\epsilon_{r,0}$ is the relative permittivity of healthy liver at frequency f. Before ablation, the propagation speed throughout the tissue is constant due to the homogeneity of healthy liver tissue. During the ablation, at a time $t = n$, the propagation speed is a function of distance from the ablation antenna x, since the tissue properties become heterogeneous. It can be estimated by:

$$v_n(x) = \frac{c}{\sqrt{\epsilon_{r,n}(x)}} \tag{7.5}$$

where $\epsilon_{r,n}(x)$ is the relative permittivity at frequency f at a distance x from the ablation antenna.

The strong correlation between relative permittivity and temperature [84] allows us to estimate the temperature profile at a time $t = n$ during ablation from the measured TDOA, since $\epsilon_{r,n}(x) = \epsilon_{r,n}(T_n(x))$. In our algorithm we solve for the temperature profile of the form of Eq. 7.1 that minimizes the difference between the measured TDOA and the approximated theoretical TDOA. Mathematically we solve for:

$$\begin{aligned} [a_n, b_n] \quad &= \text{argmin}_{a,b} \quad \left\| \Delta\tau_n - \sum_i \left(\frac{\Delta x}{v_{n,i}(a,b)} - \frac{\Delta x}{v_0} \right) \right\|^2 \\ \text{subject to:} \quad & 18 \le a \le 110 \\ & -0.27 \le b \le -0.18 \end{aligned} \tag{7.6}$$

and estimate the temperature profile $T_n^*(x)$ between the ablation antenna and the sensing antenna at time $t = n$ as:

$$T_n^*(x) = a_n \cdot e^{-b_n x} + 37, \text{ for } x \geq 2.5 \text{ mm} \tag{7.7}$$

In equation 7.6 the summation consists of the discretized version of Eq. 7.3. The number of elements in the summation will depend on the grid size. However, note that it only needs to consider voxels close to the ablation antenna, where there is a change in dielectric properties. Far enough from the ablation antenna the summation terms do not contribute to the summation, because the properties of the tissue will remain unchanged compared to before ablation.

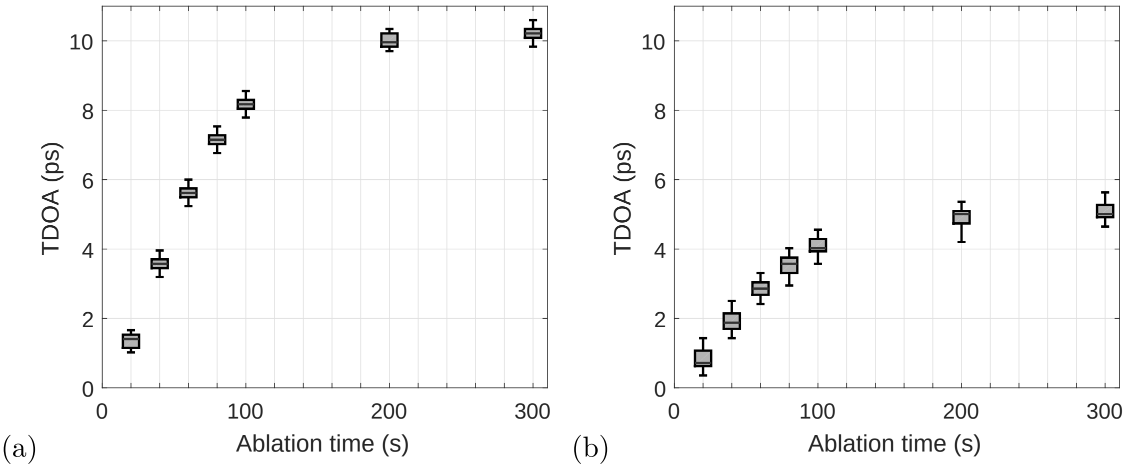

Figure 7.6: Boxplots of time difference of arrival (TDOA) during ablation at 1.9 GHz. The boxplots show the distribution (median,maximum, minimum, 10^{th} and 90^{th} percentile) for 1000 noise realizations at a 30 dB SNR. (a) 40 W input power, (b) 30 W input power.

7.4 Results

We evaluated the performance of our algorithm for computational simulations of MWA of liver tissue at 40 W and 30 W, at 1.9 GHz. During the ablations, the monitoring signal (Gaussian pulse) was sent out and recorded every 20 seconds. We added noise to the received signals. In a typical microwave imaging array that uses a VNA to source and record the signals, the practical observed noise floor lies around -80 dB. In our data acquisition configuration, the received signal is around 20 to 30 dB lower than the transmitted signal,

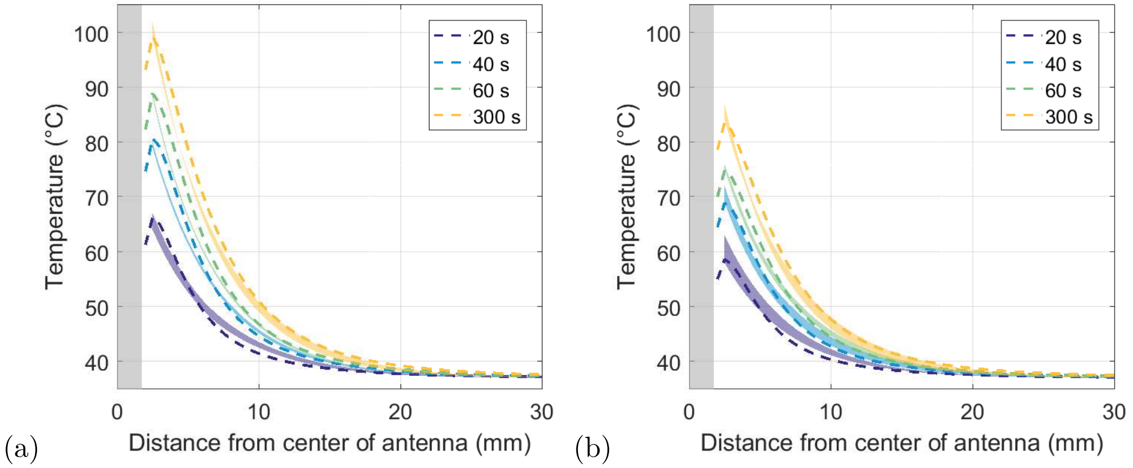

Figure 7.7: Actual (dashed line) and estimated (solid band) temperature profiles for different times during ablation. The shaded region corresponds to the range of temperature profiles between the 10th and 90th percentiles of estimations obtained for 1000 noise realizations at a 30 dB SNR. (a) 40 W input power, (b) 30 W input power. The gray shaded area corresponds to the area occupied by the ablation antenna.

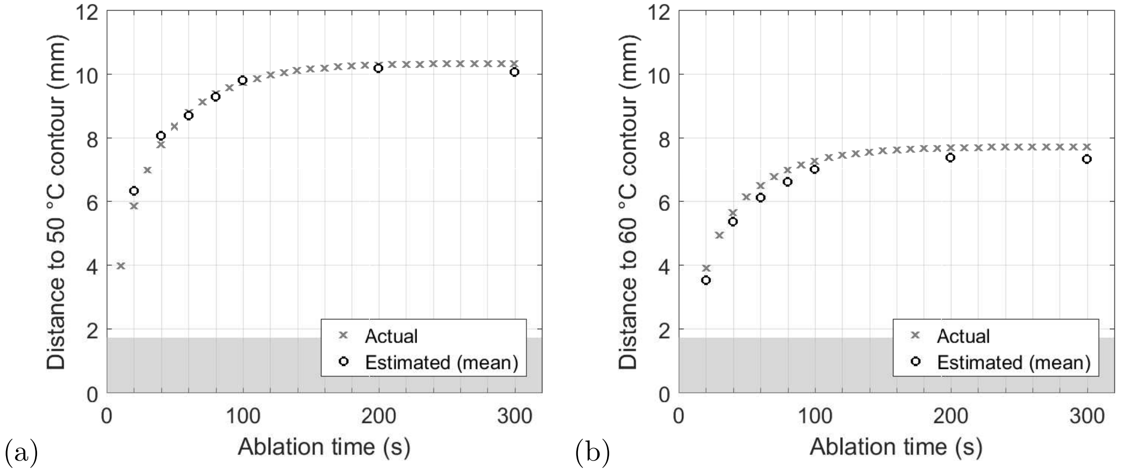

Figure 7.8: Actual and mean of the estimated distances for 1000 noise realizations at a 30 dB SNR to the (a) 50 °C contour and the (b) 60 °C contour during a 40 W ablation of liver tissue. The gray shaded area corresponds to the area occupied by the ablation antenna.

so we expect an SNR around 50 dB for the received signal. To be conservative, we added noise to simulate a 30 dB SNR.

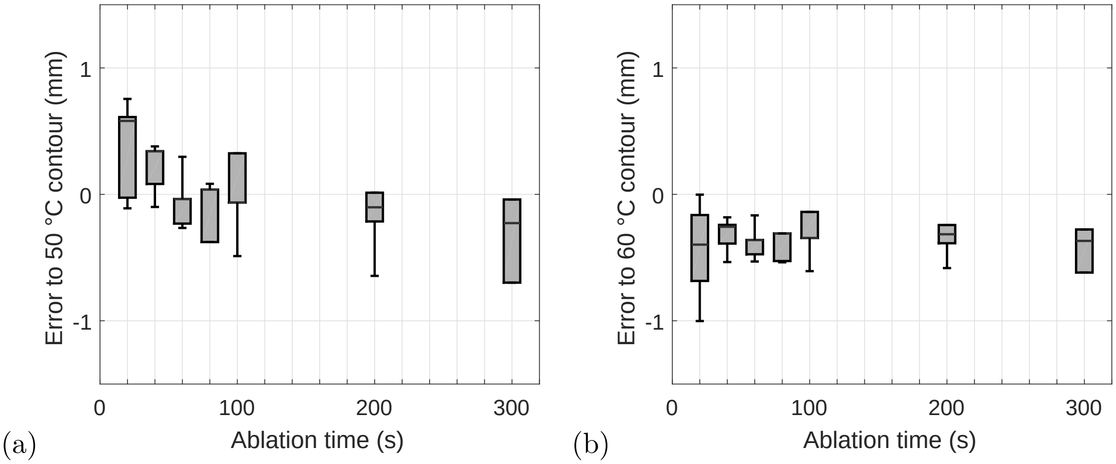

Figure 7.9: Distribution of the errors for the estimated distances to (a) 50 °C contour and (b) 60 °C contour during a 40 W ablation of liver tissue. The box plots show the median, minimum, maximum, 10th percentile, and 90th percentile of the error distribution for 1000 noise realizations at a 30 dB SNR.

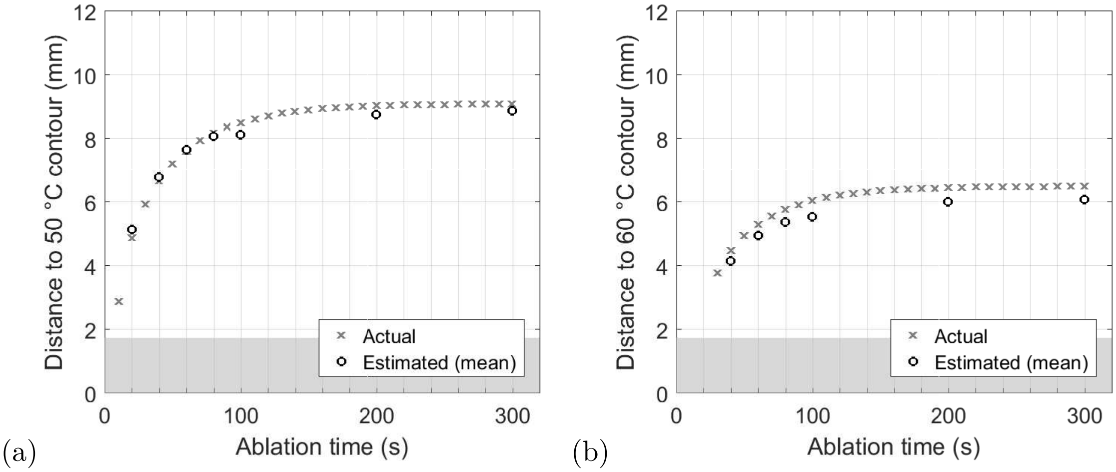

Figure 7.10: Actual and mean of the estimated distances for 1000 noise realizations at a 30 dB SNR to the (a) 50 °C contour and the (b) 60 °C contour during a 30 W ablation of liver tissue. The gray shaded area corresponds to the area occupied by the ablation antenna.

Figure 7.6 shows the TDOAs obtained during ablation from the cross-correlation calculation in Eq. 7.2. The plot summarizes the results for 1000 noise realizations at a 30 dB SNR, showing the median, minimum, maximum, and 10th and 90th percentiles. We

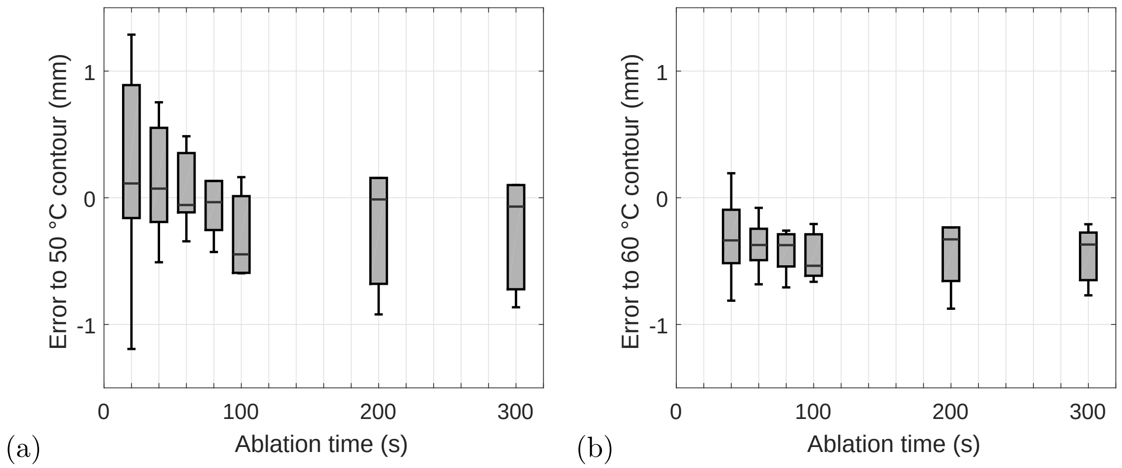

Figure 7.11: Distribution of the errors for the estimated distances to (a) 50 °C contour and (b) 60 °C contour during a 30 W ablation of liver tissue. The box plots show the median, minimum, maximum, 10^{th} percentile, and 90^{th} percentile of the error distribution for 1000 noise realizations at a 30 dB SNR.

observe that for realistic ablations at 40 W and 30 W of input power, the TDOAs are in the order of picoseconds. As expected, we observe the TDOAs increase over time during the ablations, and they are larger for 40 W than for 30 W, due to more drastic changes in the tissue dielectric properties. The variability we observe in the TDOA due to the noise present in the signals is in the order of half a picosecond for a 30 dB SNR.

Figure 7.7 shows the estimated temperature profiles as a function of distance from the center of the ablation antenna at different times during the ablation (20 s, 40 s, 60 s, and 300 s). We estimated the temperature profiles with our method, by solving Eq. 7.6. The solid line shows the actual temperature profile for reference, while the shaded bands show the range between the 10^{th} and 90^{th} percentiles of the estimated temperature profiles. We observe that the estimated curves closely follow the actual curves during ablation.

The estimated temperature profiles can be used to calculate important information during the ablation, such as the radius of the ablation zone, which can be considered to be the distance to a relevant temperature contour. Figures 7.8 and 7.9 show the estimated distances to the 50 °C and 60 °C contours during ablation at 40 W. The distances to these two temperature contours have clinical application because they indicate the area up to which doctors can confirm that the tissue has been damaged. Figure 7.8shows the actual distance and the mean of our estimated distances for 1000 noise realizations at 30 dB SNR. We observe that the size of the ablated zone increases as the ablation progresses to reach around 1 cm in radius, and the mean of our estimations is very close to the actual distances at all times during ablation. Figure 7.9 shows the distribution of the errors for the estimations of the distances to these two contours. We observe errors of less than 1 mm; therefore the method is highly accurate for ablation zones this size.

Figures 7.10 and 7.11 show the actual and estimated distances to the 50 °C and 60 °C contours for ablation at 30 W. For this power of ablation, the ablated region is smaller in radius, reaching around 9 mm in radius. Again we observe that the errors of our estimations are less than 1 mm during the ablation.

7.5 Conclusions

Our proposed TDOA method uses a spatial temperature model obtained from coupled EM-thermal computational simulations to reliably estimate the temperature distribution of the tissue at any moment during MWA. We showed that coupling the EM and thermal MWA simulations every 10 seconds to incorporate temperature-dependent dielectric properties and update the SAR pattern, has significant effects on the spatial and temperature characteristics of the ablated region.

We demonstrated that the TDOA principles can be used to estimate the temperature of the tissue in realistic ablations by simplifying the calculation discretizing the spatial domain and assuming the propagation speed at the predominant frequency of the received signal. Furthermore, the TDOA calculation can be used in combination with the spatial temperature model, obtained from computational simulations, to solve for the temperature profiles during ablation accurately.

We showed that the method achieves highly accurate results in high noise scenarios. The estimated radius the ablation zones, determined by distances to relevant temperature contours, had errors of less than 1 mm.

BIBLIOGRAPHY

[1] J. Ferlay, I. Soerjomataram, R. Dikshit, S. Eser, C. Mathers, M. Rebelo, D. M. Parkin, D. Forman, and F. Bray, “Cancer incidence and mortality worldwide: Sources, methods and major patterns in GLOBOCAN 2012: Globocan 2012,” *International Journal of Cancer*, vol. 136, pp. E359–E386, Mar. 2015.

[2] R. L. Siegel, K. D. Miller, and A. Jemal, “Cancer statistics, 2016: Cancer Statistics, 2016,” *CA: A Cancer Journal for Clinicians*, vol. 66, pp. 7–30, Jan. 2016.

[3] D. A. Berry, K. A. Cronin, S. K. Plevritis, D. G. Fryback, L. Clarke, M. Zelen, J. S. Mandelblatt, A. Y. Yakovlev, J. D. F. Habbema, and E. J. Feuer, “Effect of screening and adjuvant therapy on mortality from breast cancer,” *New England Journal of Medicine*, vol. 353, pp. 1784–1792, Oct. 2005.

[4] M. B. Mainiero, A. Lourenco, M. C. Mahoney, M. S. Newell, L. Bailey, L. D. Barke, C. D’Orsi, J. A. Harvey, M. K. Hayes, P. T. Huynh, P. M. Jokich, S.-J. Lee, C. D. Lehman, D. A. Mankoff, J. A. Nepute, S. B. Patel, H. E. Reynolds, M. L. Sutherland, and B. G. Haffty, “ACR appropriateness criteria breast cancer screening,” *Journal of the American College of Radiology*, vol. 10, pp. 11–14, Jan. 2013.

[5] W. A. Berg, “Tailored supplemental screening for breast cancer: What now and what next?,” *American Journal of Roentgenology*, vol. 192, pp. 390–399, Feb. 2009.

[6] D. Saslow, C. Boetes, W. Burke, S. Harms, M. O. Leach, C. D. Lehman, E. Morris, E. Pisano, M. Schnall, S. Sener, R. A. Smith, E. Warner, M. Yaffe, K. S. Andrews, C. A. Russell, and for the American Cancer Society Breast Cancer Advisory Group, “American Cancer Society guidelines for breast screening with MRI as an adjunct to mammography,” *CA: A Cancer Journal for Clinicians*, vol. 57, pp. 75–89, Mar. 2007.

[7] J. D. Shea, P. Kosmas, S. C. Hagness, and B. D. Van Veen, “Three-dimensional microwave imaging of realistic numerical breast phantoms via a multiple-frequency inverse scattering technique,” *Medical Physics*, vol. 37, no. 8, p. 4210, 2010.

[8] T. Rubaek, P. M. Meaney, P. Meincke, and K. D. Paulsen, “Nonlinear microwave imaging for breast-cancer screening using Gauss-Newton’s method and the CGLS inversion

algorithm," *IEEE Transactions on Antennas and Propagation*, vol. 55, pp. 2320–2331, Aug. 2007.

[9] A. Abubakar, P. M. van den Berg, and J. J. Mallorqui, "Imaging of biomedical data using a multiplicative regularized contrast source inversion method," *IEEE Transactions on Microwave Theory and Techniques*, vol. 50, pp. 1761–1771, July 2002.

[10] M. Lazebnik, D. Popovic, L. McCartney, C. B. Watkins, M. J. Lindstrom, J. Harter, S. Sewall, T. Ogilvie, A. Magliocco, T. M. Breslin, W. Temple, D. Mew, J. H. Booske, M. Okoniewski, and S. C. Hagness, "A large-scale study of the ultrawideband microwave dielectric properties of normal, benign and malignant breast tissues obtained from cancer surgeries," *Physics in Medicine and Biology*, vol. 52, pp. 6093–6115, Oct. 2007.

[11] M. Lazebnik, L. McCartney, D. Popovic, C. B. Watkins, M. J. Lindstrom, J. Harter, S. Sewall, A. Magliocco, J. H. Booske, M. Okoniewski, and S. C. Hagness, "A large-scale study of the ultrawideband microwave dielectric properties of normal breast tissue obtained from reduction surgeries," *Physics in Medicine and Biology*, vol. 52, pp. 2637–2656, May 2007.

[12] A. Mashal, B. Sitharaman, Xu Li, P. K. Avti, A. V. Sahakian, J. H. Booske, and S. C. Hagness, "Toward carbon-nanotube-based theranostic agents for microwave detection and treatment of breast cancer: Enhanced dielectric and heating response of tissue-mimicking materials," *IEEE Transactions on Biomedical Engineering*, vol. 57, pp. 1831–1834, Aug. 2010.

[13] G. Bellizzi, O. M. Bucci, and I. Catapano, "Microwave cancer imaging exploiting magnetic nanoparticles as contrast agent," *IEEE Transactions on Biomedical Engineering*, vol. 58, pp. 2528–2536, Sept. 2011.

[14] T. J. Colgan, S. C. Hagness, and B. D. Van Veen, "A 3-D level set method for microwave breast imaging," *IEEE Transactions on Biomedical Engineering*, vol. 62, pp. 2526–2534, Oct. 2015.

[15] P. M. v. d. Berg and R. E. Kleinman, "A total variation enhanced modified gradient algorithm for profile reconstruction," *Inverse Problems*, vol. 11, pp. L5–L10, June 1995.

[16] P. Mojabi and J. LoVetri, “Overview and classification of some regularization techniques for the Gauss-Newton inversion method applied to inverse scattering problems,” *IEEE Transactions on Antennas and Propagation*, vol. 57, pp. 2658–2665, Sept. 2009.

[17] P. Mojabi and J. LoVetri, “Enhancement of the Krylov subspace regularization for microwave biomedical imaging,” *IEEE Transactions on Medical Imaging*, vol. 28, pp. 2015–2019, Dec. 2009.

[18] N. Irishina, D. Álvarez, O. Dorn, and M. Moscoso, “Structural level set inversion for microwave breast screening,” *Inverse Problems*, vol. 26, p. 035015, Mar. 2010.

[19] W. Zhou, Y. Jiang, L. Chen, L. Ling, M. Liang, H. Pan, S. Wang, Q. Ding, X. Liu, and S. Wang, “Image and pathological changes after microwave ablation of breast cancer: A pilot study,” *European Journal of Radiology*, vol. 83, pp. 1771–1777, Oct. 2014.

[20] W. Zhou, X. Zha, X. Liu, Q. Ding, L. Chen, Y. Ni, Y. Zhang, Y. Xu, L. Chen, Y. Zhao, and S. Wang, “US-guided percutaneous microwave coagulation of small breast cancers: A clinical study,” *Radiology*, vol. 263, pp. 364–373, May 2012.

[21] G.-J. Qian, N. Wang, Q. Shen, Y. H. Sheng, J.-Q. Zhao, M. Kuang, G.-J. Liu, and M.-C. Wu, “Efficacy of microwave versus radiofrequency ablation for treatment of small hepatocellular carcinoma: experimental and clinical studies,” *European Radiology*, vol. 22, pp. 1983–1990, Sept. 2012.

[22] R. C. G. Martin, C. R. Scoggins, and K. M. McMasters, “Safety and Efficacy of Microwave Ablation of Hepatic Tumors: A Prospective Review of a 5-Year Experience,” *Annals of Surgical Oncology*, vol. 17, pp. 171–178, Jan. 2010.

[23] J. Yu, P. Liang, X.-l. Yu, Z.-g. Cheng, Z.-y. Han, X. Zhang, J. Dong, M.-j. Mu, X. Li, and X.-h. Wang, “US-guided percutaneous microwave ablation versus open radical nephrectomy for small Renal cell carcinoma: Intermediate-term results,” *Radiology*, vol. 270, pp. 880–887, Mar. 2014.

[24] A. Basile, G. Failla, A. Reforgiato, G. Scavone, E. Mundo, M. Messina, G. Caltabiano, F. Arena, V. Ricceri, A. Scavone, and S. Masala, “The use of microwaves ablation in the treatment of epiphyseal osteoid osteomas,” *CardioVascular and Interventional Radiology*, vol. 37, pp. 737–742, June 2014.

[25] D. E. Dupuy, “Microwave ablation compared with radiofrequency ablation in lung tissue–Is microwave not just for popcorn anymore?,” *Radiology*, vol. 251, pp. 617–618, June 2009.

[26] C. J. Simon, D. E. Dupuy, and W. W. Mayo-Smith, “Microwave ablation: Principles and applications,” *RadioGraphics*, vol. 25, pp. S69–S83, Oct. 2005.

[27] C. Correa-Gallego, A. M. Karkar, S. Monette, P. C. Ezell, W. R. Jarnagin, and T. P. Kingham, “Intraoperative ultrasound and tissue elastography measurements do not predict the size of hepatic microwave ablations,” *Academic Radiology*, vol. 21, pp. 72–78, Jan. 2014.

[28] L. G. Merckel, L. W. Bartels, M. O. Köhler, H. J. G. D. van den Bongard, R. Deckers, W. P. T. M. Mali, C. A. Binkert, C. T. Moonen, K. G. A. Gilhuijs, and M. A. A. J. van den Bosch, “MR-guided high-intensity focused ultrasound ablation of breast cancer with a dedicated breast platform,” *CardioVascular and Interventional Radiology*, vol. 36, pp. 292–301, Apr. 2013.

[29] R. Kloeckner, D. P. d. Santos, J. Schneider, L. Kara, C. Dueber, and M. B. Pitton, “Radiation exposure in CT-guided interventions,” *European Journal of Radiology*, vol. 82, pp. 2253–2257, Dec. 2013.

[30] V. Lopresto, R. Pinto, G. A. Lovisolo, and M. Cavagnaro, “Changes in the dielectric properties of *ex vivo* bovine liver during microwave thermal ablation at 2.45 GHz,” *Physics in Medicine and Biology*, vol. 57, pp. 2309–2327, Apr. 2012.

[31] Z. Ji and C. L. Brace, “Expanded modeling of temperature-dependent dielectric properties for microwave thermal ablation,” *Physics in Medicine and Biology*, vol. 56, pp. 5249–5264, Aug. 2011.

[32] A. Rosen, M. Stuchly, and A. Vander Vorst, “Applications of RF/microwaves in medicine,” *IEEE Transactions on Microwave Theory and Techniques*, vol. 50, pp. 963–974, Mar. 2002.

[33] R. J. Halter, T. Zhou, P. M. Meaney, A. Hartov, R. J. Barth, K. M. Rosenkranz, W. A. Wells, C. A. Kogel, A. Borsic, E. J. Rizzo, and K. D. Paulsen, “The correlation of in vivo and ex vivo tissue dielectric properties to validate electromagnetic breast imaging:

Initial clinical experience," *Physiological Measurement*, vol. 30, pp. S121–S136, June 2009.

[34] W. T. Joines, "The measured electrical properties of normal and malignant human tissues from 50 to 900 MHz," *Medical Physics*, vol. 21, no. 4, p. 547, 1999.

[35] L. Garnero, A. Franchois, J.-P. Hugonin, C. Pichot, and N. Joachimowicz, "Microwave imaging-complex permittivity reconstruction-by simulated annealing," *IEEE Transactions on Microwave Theory and Techniques*, vol. 39, pp. 1801–1807, Nov. 1991.

[36] Q. Fang, P. Meaney, S. Geimer, A. Streltsov, and K. Paulsen, "Microwave image reconstruction from 3-D fields coupled to 2-D parameter estimation," *IEEE Transactions on Medical Imaging*, vol. 23, pp. 475–484, Apr. 2004.

[37] Z. Zhang and Q. Liu, "Three-dimensional nonlinear image reconstruction for microwave biomedical imaging," *IEEE Transactions on Biomedical Engineering*, vol. 51, pp. 544–548, Mar. 2004.

[38] M. Haynes, S. Clarkson, and M. Moghaddam, "Electromagnetic inverse scattering algorithm and experiment using absolute source characterization," *IEEE Transactions on Antennas and Propagation*, vol. 60, pp. 1854–1867, Apr. 2012.

[39] W. C. Chew, *Waves and fields in inhomogeneous media.* Piscataway, NY: IEEE Press, 1995.

[40] J. Nocedal and S. J. Wright, *Numerical Optimization.* New York: Springer, 2006. OCLC: 209918411.

[41] P. M. v. d. Berg and R. E. Kleinman, "A contrast source inversion method," *Inverse Problems*, vol. 13, pp. 1607–1620, Dec. 1997.

[42] R. F. Remis and P. M. v. d. Berg, "On the equivalence of the Newton-Kantorovich and distorted Born methods," *Inverse Problems*, vol. 16, pp. L1–L4, Feb. 2000.

[43] C. Gilmore, P. Mojabi, and J. LoVetri, "Comparison of an enhanced distorted Born iterative method and the multiplicative-regularized contrast source inversion method," *IEEE Transactions on Antennas and Propagation*, vol. 57, pp. 2341–2351, Aug. 2009.

[44] F. Gao, B. D. Van Veen, and S. C. Hagness, "Microwave imaging of breast tumors with contrast agents: Theoretical study of dielectric contrast enhancement requirements," in *IEEE Interational Symposium on Antennas and Propagation*, pp. 2030–2031, IEEE, July 2013.

[45] J. Fessler, N. Clinthorne, and W. Rogers, "Regularized emission image reconstruction using imperfect side information," *IEEE Transactions on Nuclear Science*, vol. 39, pp. 1464–1471, Oct. 1992.

[46] G. Gindi, M. Lee, A. Rangarajan, and I. Zubal, "Bayesian reconstruction of functional images using anatomical information as priors," *IEEE Transactions on Medical Imaging*, vol. 12, pp. 670–680, Dec. 1993.

[47] M. Glidewell and K. Ng, "Anatomically constrained electrical impedance tomography for anisotropic bodies via a two-step approach," *IEEE Transactions on Medical Imaging*, vol. 14, pp. 498–503, Sept. 1995.

[48] B. Lipinski, H. Herzog, E. Rota Kops, W. Oberschelp, and H. Muller-Gartner, "Expectation maximization reconstruction of positron emission tomography images using anatomical magnetic resonance information," *IEEE Transactions on Medical Imaging*, vol. 16, pp. 129–136, Apr. 1997.

[49] A. M. Alessio and P. E. Kinahan, "Improved quantitation for PET/CT image reconstruction with system modeling and anatomical priors," *Medical Physics*, vol. 33, no. 11, p. 4095, 2006.

[50] A. Golnabi, S. Geimer, P. Meaney, and K. Paulsen, "Comparison of no-prior and soft-prior regularization in biomedical microwave imaging," *Journal of Medical Physics*, vol. 36, no. 3, p. 159, 2011.

[51] A. H. Golnabi, P. M. Meaney, and K. D. Paulsen, "Tomographic microwave imaging with incorporated prior spatial information," *IEEE Transactions on Microwave Theory and Techniques*, vol. 61, pp. 2129–2136, May 2013.

[52] P. M. Meaney, A. H. Golnabi, N. R. Epstein, S. D. Geimer, M. W. Fanning, J. B. Weaver, and K. D. Paulsen, "Integration of microwave tomography with magnetic resonance for improved breast imaging," *Medical Physics*, vol. 40, no. 10, p. 103101, 2013.

[53] C. L. Brace, “Microwave Tissue Ablation: Biophysics, Technology, and Applications,” *Critical Reviews*^{TM} *in Biomedical Engineering*, vol. 38, no. 1, pp. 65–78, 2010.

[54] Fornage, “Image-guided percutaneous ablation of small breast cancer: Which technique is leading the pack?,” *Technology in Cancer Research and Treatment*, 2013.

[55] D. Kreb, B. Looij, M. Ernst, M. Rutten, G. Jager, J. van der Linden, J. Pruijt, and K. Bosscha, “Ultrasound-guided radiofrequency ablation of early breast cancer in a resection specimen: Lessons for further research,” *The Breast*, vol. 22, pp. 543–547, Aug. 2013.

[56] B. Hildebrandt, “The cellular and molecular basis of hyperthermia,” *Critical Reviews in Oncology/Hematology*, vol. 43, pp. 33–56, July 2002.

[57] M. Lazebnik, M. C. Converse, J. H. Booske, and S. C. Hagness, “Ultrawideband temperature-dependent dielectric properties of animal liver tissue in the microwave frequency range,” *Physics in Medicine and Biology*, vol. 51, pp. 1941–1955, Apr. 2006.

[58] H. Schwan and K. Foster, “RF-field interactions with biological systems: Electrical properties and biophysical mechanisms,” *Proceedings of the IEEE*, vol. 68, no. 1, pp. 104–113, 1980.

[59] H. Luyen, S. C. Hagness, and N. Behdad, “A balun-free helical antenna for minimally invasive microwave ablation,” *IEEE Transactions on Antennas and Propagation*, vol. 63, pp. 959–965, Mar. 2015.

[60] M. Haynes, J. Stang, and M. Moghaddam, “Real-time microwave imaging of differential temperature for thermal therapy monitoring,” *IEEE Transactions on Biomedical Engineering*, vol. 61, pp. 1787–1797, June 2014.

[61] O. Fiser, M. Helbig, J. Sachs, S. Ley, I. Merunka, and J. Vrba, “Microwave Non-Invasive Temperature Monitoring Using UWB Radar for Cancer Treatment by Hyperthermia,” *Progress In Electromagnetics Research*, vol. 162, pp. 1–14, 2018.

[62] G. Chen, J. Stang, M. Haynes, E. Leuthardt, and M. Moghaddam, “Real-Time Three-Dimensional Microwave Monitoring of Interstitial Thermal Therapy,” *IEEE Transactions on Biomedical Engineering*, vol. 65, pp. 528–538, Mar. 2018.

[63] L. M. Neira, B. D. Van Veen, and S. C. Hagness, “High-Resolution Microwave Breast Imaging Using a 3-D Inverse Scattering Algorithm With a Variable-Strength Spatial Prior Constraint,” *IEEE Transactions on Antennas and Propagation*, vol. 65, pp. 6002–6014, Nov. 2017.

[64] A. H. Golnabi, P. M. Meaney, and K. D. Paulsen, “3d microwave tomography of the breast using prior anatomical information,” *Medical Physics*, vol. 43, pp. 1933–1944, Apr. 2016.

[65] L. M. Neira, B. D. Van Veen, and S. C. Hagness, “An inverse scattering algorithm with spatial prior constraints for high-resolution microwave breast imaging,” in *IEEE Interational Symposium on Antennas and Propagation*, pp. 1113–1114, 2014.

[66] E. Zastrow, S. Davis, M. Lazebnik, F. Kelcz, B. Van Veen, and S. Hagness, “Development of anatomically realistic numerical breast phantoms with accurate dielectric properties for modeling microwave interactions with the human breast,” *IEEE Transactions on Biomedical Engineering*, vol. 55, pp. 2792–2800, Dec. 2008.

[67] University of Wisconsin Cross-Disciplinary Electromagnetics Laboratory (UWCEM), “Numerical breast phantom repository.” http://uwcem.ece.wisc.edu.

[68] S. Gabriel, R. W. Lau, and C. Gabriel, “The dielectric properties of biological tissues: III. Parametric models for the dielectric spectrum of tissues,” *Physics in Medicine and Biology*, vol. 41, pp. 2271–2293, Nov. 1996.

[69] A. Taflove and S. C. Hagness, *Computational electrodynamics: the finite-difference time-domain method*. Artech House antennas and propagation library, Boston: Artech House, 3rd ed ed., 2005.

[70] M. Ostadrahimi, A. Zakaria, J. LoVetri, and L. Shafai, “A Near-Field Dual Polarized (TE–TM) Microwave Imaging System,” *IEEE Transactions on Microwave Theory and Techniques*, vol. 61, pp. 1376–1384, Mar. 2013.

[71] M. J. Burfeindt, N. Behdad, B. D. Van Veen, and S. C. Hagness, “Quantitative Microwave Imaging of Realistic Numerical Breast Phantoms Using an Enclosed Array of Multiband, Miniaturized Patch Antennas,” *IEEE Antennas and Wireless Propagation Letters*, vol. 11, pp. 1626–1629, 2012.

[72] F. Gao, B. D. Van Veen, and S. C. Hagness, "Sensitivity of the distorted born iterative method to the initial guess in microwave breast imaging," *IEEE Transactions on Antennas and Propagation*, vol. 63, pp. 3540–3547, Aug. 2015.

[73] N. C. I. , "SEER Stat Fact Sheets: Breast Cancer," 2017.

[74] C. E. Hill-Kayser, C. Vachani, M. K. Hampshire, G. A. Di Lullo, and J. M. Metz, "Cosmetic Outcomes and Complications Reported by Patients Having Undergone Breast-Conserving Treatment," *International Journal of Radiation Oncology*Biology*Physics*, vol. 83, pp. 839–844, July 2012.

[75] T. L. Huston and R. M. Simmons, "Ablative therapies for the treatment of malignant diseases of the breast," *The American Journal of Surgery*, vol. 189, pp. 694–701, June 2005.

[76] B. D. Fornage and K. K. Hunt, "Image-guided Percutaneous Ablation of Small Breast Cancer: Which Technique is Leading the Pack?," *Technology in Cancer Research & Treatment*, vol. 14, pp. 209–211, Apr. 2015.

[77] P. Cortazar, L. Zhang, M. Untch, K. Mehta, J. P. Costantino, N. Wolmark, H. Bonnefoi, D. Cameron, L. Gianni, P. Valagussa, S. M. Swain, T. Prowell, S. Loibl, D. L. Wickerham, J. Bogaerts, J. Baselga, C. Perou, G. Blumenthal, J. Blohmer, E. P. Mamounas, J. Bergh, V. Semiglazov, R. Justice, H. Eidtmann, S. Paik, M. Piccart, R. Sridhara, P. A. Fasching, L. Slaets, S. Tang, B. Gerber, C. E. Geyer, R. Pazdur, N. Ditsch, P. Rastogi, W. Eiermann, and G. von Minckwitz, "Pathological complete response and long-term clinical benefit in breast cancer: the CTNeoBC pooled analysis," *The Lancet*, vol. 384, pp. 164–172, July 2014.

[78] S. Li, M. Kennedy, S. Payne, K. Kennedy, V. L. Seewaldt, S. V. Pizzo, and R. E. Bachelder, "Model of Tumor Dormancy/Recurrence after Short-Term Chemotherapy," *PLoS ONE*, vol. 9, p. e98021, May 2014.

[79] P. Liang, B. Dong, X. Yu, D. Yu, Y. Wang, L. Feng, and Q. Xiao, "Prognostic Factors for Survival in Patients with Hepatocellular Carcinoma after Percutaneous Microwave Ablation," *Radiology*, vol. 235, pp. 299–307, Apr. 2005.

[80] J. Yu, B.-H. Chen, J. Zhang, Z.-Y. Han, H. Wu, Y. Huang, M.-J. Mu, and P. Liang, "Ultrasound guided percutaneous microwave ablation of benign breast lesions," *Oncotarget*, vol. 8, pp. 79376–79386, Oct. 2017.

[81] D. Yang, J. Bertram, M. Converse, A. O'Rourke, J. Webster, S. Hagness, J. Will, and D. Mahvi, "A Floating Sleeve Antenna Yields Localized Hepatic Microwave Ablation," *IEEE Transactions on Biomedical Engineering*, vol. 53, pp. 533–537, Mar. 2006.

[82] R. O. Mays, *Microwaves in Heterogeneous Tissue: Development and Evaluation of Arrays and Antennas for Breast Imaging, Tumor Treatment, and Treatment Monitoring.* PhD thesis, Department of Electrical and Computer Engineering, University of Wisconsin-Madison, Madison, Wisconsin, 2016.

[83] D. Hagl, D. Popovic, S. Hagness, J. Booske, and M. Okoniewski, "Sensing volume of open-ended coaxial probes for dielectric characterization of breast tissue at microwave frequencies," *IEEE Transactions on Microwave Theory and Techniques*, vol. 51, pp. 1194–1206, Apr. 2003.

[84] L. M. Neira, J. Sawicki, B. D. Van Veen, and S. C. Hagness, "Characterization and Analysis of Wideband Temperature-Dependent Dielectric Properties of Liver Tissue for Next-Generation Minimally Invasive Microwave Tumor Ablation Technology," in *2018 IEEE/MTT-S International Microwave Symposium - IMS*, (Philadelphia, PA, USA), pp. 911–914, IEEE, June 2018.

[85] J. F. Sawicki, J. D. Shea, N. Behdad, and S. C. Hagness, "The impact of frequency on the performance of microwave ablation," *International Journal of Hyperthermia*, vol. 33, pp. 61–68, Jan. 2017.

[86] R. Scapaticci, G. G. Bellizzi, M. Cavagnaro, V. Lopresto, and L. Crocco, "Exploiting Microwave Imaging Methods for Real-Time Monitoring of Thermal Ablation," *International Journal of Antennas and Propagation*, vol. 2017, pp. 1–13, 2017.

[87] S. Kidera, L. M. Neira, B. D. Van Veen, and S. C. Hagness, "TDOA-based microwave imaging algorithm for real-time monitoring of microwave ablation," in *2017 11th European Conference on Antennas and Propagation (EUCAP)*, (Paris, France), pp. 3717–3721, IEEE, Mar. 2017.

[88] V. Lopresto, R. Pinto, and M. Cavagnaro, “Experimental characterisation of the thermal lesion induced by microwave ablation,” *International Journal of Hyperthermia*, vol. 30, pp. 110–118, Mar. 2014.

[89] Hung Luyen, Fuqiang Gao, S. C. Hagness, and N. Behdad, “Microwave Ablation at 10.0 GHz Achieves Comparable Ablation Zones to 1.9 GHz in Ex Vivo Bovine Liver,” *IEEE Transactions on Biomedical Engineering*, vol. 61, pp. 1702–1710, June 2014.

[90] A. P. O’Rourke, M. Lazebnik, J. M. Bertram, M. C. Converse, S. C. Hagness, J. G. Webster, and D. M. Mahvi, “Dielectric properties of human normal, malignant and cirrhotic liver tissue: *in vivo* and *ex vivo* measurements from 0.5 to 20 GHz using a precision open-ended coaxial probe,” *Physics in Medicine and Biology*, vol. 52, pp. 4707–4719, Aug. 2007.

[91] C. L. Brace, “Radiofrequency and microwave ablation of the liver, lung, kidney, and bone: What are the differences?,” *Current Problems in Diagnostic Radiology*, vol. 38, pp. 135–143, May 2009.

[92] B. Kaltenbach, A. Roman, K. Eichler, N.-E. A. Nour-Eldin, T. J. Vogl, and S. Zangos, “Real-time qualitative MR monitoring of microwave ablation in *ex vivo* livers,” *International Journal of Hyperthermia*, vol. 32, pp. 757–764, Oct. 2016.

[93] G. G. Bellizzi, L. Crocco, M. Cavagnaro, L. Farina, V. Lopresto, and R. Scapaticci, “A full-wave numerical assessment of microwave tomography for monitoring cancer ablation,” in *2017 11th European Conference on Antennas and Propagation (EUCAP)*, (Paris, France), pp. 3722–3725, IEEE, Mar. 2017.

[94] S. Kidera, L. M. Neira, B. D. Van Veen, and S. C. Hagness, “TDOA-based microwave imaging algorithm for real-time microwave ablation monitoring,” *International Journal of Microwave and Wireless Technologies*, vol. 10, pp. 169–178, Mar. 2018.

[95] J. F. Sawicki, H. Luyen, Y. Mohtashami, J. D. Shea, N. Behdad, and S. C. Hagness, “The Performance of Higher-Frequency Microwave Ablation in the Presence of Perfusion,” *IEEE Transactions on Biomedical Engineering*, pp. 1–1, 2018.